TECHNISCHE UNIVERSITÄT MÜNCHEN
Lehrstuhl für Angewandte Mechanik

Permanent Magnet Reluctance Actuators for Vibration Testing

Daniel Wiedemann

Vollständiger Abdruck der von der Fakultät für Maschinenwesen
der Technischen Universität München zur Erlangung des akademischen Grades eines

Doktor-Ingenieurs

genehmigten Dissertation.

Abstract

The analysis of vehicles and automotive components for disturbing noise requires actuators with high force density, robustness and energy efficiency. This thesis covers the mechatronic design and simulation of magnetic reluctance actuators for vibration excitation. A comparison with hydraulic and electrodynamic actuation concepts shows the application potential of reluctance force actuators in automotive vibration test rigs. For the magnetic design, reluctance circuits and the finite element analysis are used. The developed topology is characterized by a fully laminated armature and a core with surface mounted permanent magnets. The resulting negative magnetic stiffness is completely compensated by mechanical springs which enable a robust and stable operation. For dynamic simulations of the electromagnetic energy conversion a co-energy based model is developed. It features low computational cost and enables an accurate description of the nonlinear actuator characteristics. The presented methods are verified by experiments with two prototype actuators.

Zusammenfassung

Die Störgeräuschanalyse von Fahrzeugen und Fahrzeugkomponenten erfordert Aktoren mit einer hohen Kraftdichte, Robustheit und Energieeffizienz. Diese Arbeit beschreibt den mechatronischen Entwurf und die Simulation von magnetischen Reluktanzaktoren für die Schwingungsanregung. Der Vergleich mit hydraulischen und elektrodynamischen Antriebskonzepten zeigt das Anwendungspotential von Reluktanzaktoren in Vibrationsprüfständen bei der Fahrzeugentwicklung. Für den Magnetkreisentwurf werden Netzwerkmodelle und die Finite-Elemente-Methode verwendet. Die entwickelte Topologie zeichnet sich durch einen vollständig geblechten Anker und einen mit Permanentmagneten bestückten Kern aus. Die negative magnetische Steifigkeit wird durch mechanische Federn voll kompensiert, so dass ein robuster und stabiler Betrieb möglich wird. Für dynamische Simulationen der elektromagnetischen Energiewandlung wird ein Modell unter Verwendung der Co-Energie entwickelt, welches einen geringen Rechenaufwand erfordert und die genaue Beschreibung der nichtlinearen Aktorcharakteristik ermöglicht. Die vorgeschlagenen Methoden werden durch Experimente mit zwei Prototypen verifiziert.

Acknowledgments

This thesis summarizes a large part of my research carried out at the Institute of Applied Mechanics, Technische Universität München. Without the help of numerous people who supported me over the the course of the previous years the completion of this work would not have been possible.

First and foremost, I would like to express my deep gratitude to my advisor Professor Heinz Ulbrich for providing an excellent research environment, stimulating discussions and helpful advice during my time as his PhD student. He gave me the freedom to pursue my own ideas and support when it was needed.

I would also like to warmly thank the second advisor Professor Horst Baier and chairman Professor Daniel Rixen for serving on my dissertation committee and for their interest in my work. For managing the project resources and his support in all administrative manners I owe thanks to Dr. Thomas Thümmel.

I very much enjoyed working with great colleagues at the institute. Here, I am particularly grateful to Dr. Marcus Herrmann, not only for triggering my interest in magnetic actuators, but also for encouraging me to take a research position. He introduced me into the field of electromagnetic devices, being a competent advisor and partner for scientific discussions.

Special thanks I wish to offer to Dr. Ulrich Koch who was responsible for the shaker plant and the control system design. The collaboration with him was always very inspiring and productive. Besides for his tireless efforts in the common project, I would like to thank him for sharing good ideas and providing industrial background knowledge to our research.

Further, I would like to sincerely thank Dr. Thomas Villgrattner, Valerio Favot, Dr. Markus Schneider and Dr. Thorsten Schindler for their continuous assistance and the many fruitful discussions. I am particularly indebted to Markus Schwienbacher for his valuable advice and helpful suggestions regarding the mechatronic aspects of this thesis. The hardware development would not have been possible without the excellent work of the institute's mechanical and electrical workshops. For the development of the power electronics and for numerous discussions about sensors and actuators I wish to express my sincere thanks to Georg Mayr. His enthusiasm and broad engineering experience contributed substantially to the experimental research. Working with him was always deeply pleasant and rewarding. Furthermore, I warmly thank Simon Gerer, Philip Schneider and Tobias Schmid for manufacturing the mechanical components and their assistance during the assembly of numerous prototypes.

I would like to thank my proofreaders Dr. Marcus Herrmann, Dr. Thomas Villgrattner, Dr. Ulrich Koch and Valerio Favot for their interest and helpful comments.

Finally, I would like to express my immense gratitude to my family who has always encouraged and supported me in all my endeavours.

Munich, April 2013   Daniel Wiedemann

Contents

Nomenclature

Abbreviations

ADC   analog to digital converter

ASCII   american standard code for information interchange

CAD   computer aided design

DC   direct current

DOF   degree of freedom

EMF   electromotive force

FE   finite element

FEM   finite element method

KCL   Kirchhoff's current law

KVL   Kirchhoff's voltage law

LTI   linear time invariant

MEC   magnetic equivalent circuit

MIMO   multiple-input multiple-output

MMF   magnetomotive force

NVH   noise, vibration, harshness

PWM   pulse width modulation

ROM   reduced order model

TWR   time waveform replication

Symbols

δ_d logarithmic decrement

δ_s skin depth

γ equivalent phase lag

$\hat{x}(t)$ oscillation amplitude

μ	magnetic permeability
μ_0	vacuum permeability
μ_r	relative permeability
μ_{PM}	permanent magnet magnetic permeability
ω_0	angular frequency
Φ	magnetic flux
Ψ	flux linkage
Ψ_0	constant flux linkage
ρ_0	material density
ρ_s	space-charge density
σ	electrical conductivity
σ	leakage factor
τ	coil time constant
Θ	magnetomotive force
Θ_{c1}	magnetomotive force of coil 1
Θ_{c2}	magnetomotive force of coil 2
Θ_{PM}	permanent magnet magnetomotive force
$\boldsymbol{\Phi}$	flux vector
$\boldsymbol{\Theta}$	magnetomotive force vector
$\boldsymbol{B}$	magnetic flux density
$\boldsymbol{E}$	electric field strength
$\boldsymbol{H}$	magnetic field strength
$\boldsymbol{J}$	current density
$\boldsymbol{n}$	normal vector
$\boldsymbol{R}$	reluctance matrix
$\boldsymbol{v}$	charge carrier velocity
ζ	damping ratio
A	area

A_0	reluctance surface
A_{co}	copper area
A_{PM}	permanent magnet cross-sectional area
A_w	winding area
B_r	remanence
B_{avg}	peak value of mean magnetic induction
d	damping constant
d_{co}	copper diameter
f	frequency
f_c	cutoff-frequency
F_{ed}	electrodynamic force
f_{mv}	magnetic force per unit volume
F_m	magnetic force
F_{rel}	reluctance force
$F_{s,max}$	maximum static force
f_{sc}	semi-cutoff frequency
h	hysteresis loss exponent
H_{cB}	coercivity
i	current
I_0	constant current
K_h	hysteresis loss constant
k_{co}	copper filling factor
k_{Fi}	force-current factor
L	inductance
l	length
L_0	self inductance
l_m	average winding length
l_{PM}	permanent magnet length

m	armature mass
n_s	number of springs
P_e	eddy current loss
P_h	hysteresis loss
P_w	winding loss
Q	charge
R	resistance
R_c	coil resistance
r_c	core radius
R_i	internal resistance
R_m	magnetic reluctance
R_{jk}	reluctance of airgap jk
R_{PM}	reluctance of permanent magnet
R_{th}	temperature-dependent winding resistance
T	Maxwell stress tensor of the magnetic field
t	lamination thickness
t	time
T_d	oscillation period
u	voltage
u_0	supply voltage
u_i	induced voltage
V	volume
w	winding number
W_{el}	electric energy
W_m	magnetic energy
W_m^{co}	magnetic co-energy
W_{therm}	thermal energy
x	armature position

x_{jk}	length of airgap jk
K	stiffness matrix
A	magnetic vector potential
M	magnetization

1. Introduction

Magnetic actuators are widespread drives in industrial automation and used in many applications such as relays, solenoid valves and locking devices. They serve as indispensable link between the information processing and the technical process.

Electromagnetic reluctance actuators are electromechanical energy converters which use the reluctance principle for the force generation. Characteristic properties are a limited stroke and an armature motion with one degree of freedom. Generally, reluctance forces allow only for the generation of a unidirectional motion due to their attractive nature. The restoring force is either provided by external forces or a second actuator. Main advantages of reluctance actuators are the comparatively simple design and system integration. In addition to a field coil, polarized actuators feature permanent magnets which increase the efficiency and energy density due to their inherent magnetization.

During the past decades, the development of magnetic actuators has witnessed significant advances. Improvements in the field of magnetic materials enabled a continuous performance enhancement with regard to the obtainable forces, strokes and energy densities. Further functionality enhancements were driven by the integration of mechanics, electromagnetics, power- and control electronics to mechatronic actuation systems. The interdisciplinary approach enables the realization of intelligent electromagnetic actuators and a precise control of the operating behavior. Hence, particularly the feedback-controlled trajectory tracking is technically feasible. As a consequence new application fields, such as the precise excitation of vibration, can be established.

Growing customer demands on quality and comfort have led to extensive vibration testing in the modern product development process. The perpetual strive for quality improvement in combination with lower costs and time-to-market reduction requires detailed analyses of products in all stages of the development process. The employment of reluctance actuators as direct drives in vibration test rigs is an interesting alternative to existing hydraulic or electrodynamic systems. However, the application poses high demands on the actuation systems in terms of robustness, performance, energy density and tracking quality.

In order to realize the specific benefits of reluctance actuators for vibration excitation, a systematic design approach is required. For this purpose the demands on reluctance actuators in vibration testing have to be determined. The description of the complex nonlinear energy conversion process requires different models for the design, simulation and control. A major design challenge for precise vibration excitation is the increase of the obtainable bandwidth through appropriate design measures for eddy current reduction. Finally, a stable and robust behavior is fundamental for the realization of multi-actuator vibration test rigs.

1.1. Literature Review

This section is organized in two parts. First a general overview of the state of the art in magnetic actuator design is given. Second, research directly related to this thesis is summarized. The application of magnetic reluctance actuators and an overview of the current status of vibration testing are presented in Chapter 2. More detailed references to specific aspects of material selection, magnetic circuit design and simulation methods are given in the chapters covering these subjects.

Magnetic Actuators

The available literature on magnetic actuators is extensive and steadily growing. Due to the large number of publications in this field, only research relevant for the key aspects of this thesis is briefly summarized in the following. First of all, introductory standard works are pointed out. Furthermore, an excerpt of international research publications on the development of magnetic actuators is presented.

The German standard work on electromagnetic actuators *Elektromagnete - Grundlagen, Berechnung, Entwurf und Anwendung* is authored by KALLENBACH *et al.* [47]. It covers all aspects of the design, control and dynamics of magnetic actuators. In addition to the basics of simulation and modeling, the practical engineering process is illustrated by application studies. The English counterpart is the book *Magnetic Actuators and Sensors* of BRAUER [9]. The author focuses more on computer-aided engineering methods for the design and application of actuators. Numerous practical examples illustrate the theoretical foundations of actuator development. STÖLTING *et al.* give an overview of the aspects of small electromagnetic drives in *Handbuch Elektrische Kleinantriebe* [104]. However, one section focuses also on the design of drives with limited motion. A broad introduction into the fundamentals of magnetics, analytical and numerical field calculations is given by CASSING *et al.* [13]. In addition, mechatronic applications of sensors and actuators are treated.

Methods for modeling and simulation of electromagnetic drives are described by JONEIT [43]. The work of STRÖHLA focuses on the same topics [106]. He develops magnetic equivalent circuits considering hysteresis, saturation, eddy currents and leakage flux. The challenging topic of actuator design under consideration of hysteresis is also treated in the thesis of ROSENBAUM [93]. He carries out extensive investigations on the influence of hysteresis on electromagnetic drives and implements suitable models. The identification of parameters and simulation examples supplement the text. The modeling and simulation of electromagnetic actuators is also treated in the thesis of GOLLEE [30]. In addition to the discussion of fundamentals, his contribution deals with the modeling of material properties and magnetic circuits, thereby focusing on the characterization of hysteresis and circuit models. The work of RADLER describes the measurement of magnetic properties [87]. For this purpose a universal test rig is designed. The results allow for a better validation of simulation models.

ROSCHKE aims at the development of feedback-controlled actuators for contactors [92]. However, his thesis also gives a broad overview of the fundamentals of solenoids. Furthermore, numerous approaches for modeling and simulation are discussed. Particularly the comparison of different methods is valuable for the de-

velopment of other magnetic devices. The application of finite element methods for the design of electromagnetic linear actuators is described by Schultz [99]. Both stationary and transient properties of reluctance actuators are determined employing numerical field calculations. In addition, he derives characteristic properties of different actuator principles and points out potential improvements which are made visible by the proposed methods.

The application of design and simulation models for the performance optimization of electromagnetic valve systems is described by Clark in [17]. The contribution shows that the force characteristics of variable air-gap reluctance actuators can be tailored to meet specific operational demands. For this purpose different topologies are investigated. The combination of a laminated stator with a slotted armature is proposed. The improvement of the dynamic parameters of magnetic valves by optimization is carried out in the work of Rosenbaum [94]. The contribution differentiates the influence of topology, load and driving method on the dynamics, thereby focusing on optimized resonant magnetic drives. Investigations on eddy currents and the potential for release delay reduction are presented. Hartwig develops translational magnetic actuators for active vibration control of combustion engines [32]. For this purpose different moving magnet actuation concepts are compared and evaluated. The design methodology for mechatronic systems according to VDI guideline 2206 is extended to micromechatronic systems by Kallenbach, M. [46]. He focuses on mini and micro actuators with a strongly nonlinear magnetic circuit. In addition to optimization methods, resonant magnetic actuation systems are treated. Particularly the configuration of resonant bidirectional and polarized systems is discussed.

The application of permanent magnets in magnetic actuators for the improvement of thermal, dynamic and other relevant properties is described in numerous publications. In the work of Riethmüller different topologies of polarized electromagnetic actuators are described [89]. The thesis delivers calculation methods for permanent magnet circuits and compares polarized and neutral magnetic actuators. A major contribution is the systematic analysis of the influence of the permanent magnet position in the magnetic circuit on the actuator performance. The magnet position in a direct comparison of serial and parallel configurations is also the topic of Zhu [125]. Depending on the specific application context, a serial configuration of coil and permanent magnet is evaluated best. An overview of the computer-aided design process of electromagnetic systems with permanent magnet materials is presented by Kallenbach in [45]. The publication also compromises application examples of such actuators.

Further contributions focus on the design of permanent magnet actuators for specific applications. Advantages of polarized actuators, such as loss reduction by current-less force generation, are used by Rens in [88] for the development of valves in combustion engines. Langley designs a short-stroke actuator for aerospace vibration control applications [65]. The high force-to-mass ratio is obtained by embedding permanent magnet materials. A quick-latching actuator is developed by Kim [52]. He uses a configuration of an electromagnetic stator with two coils and an armature equipped with permanent magnets. Complementary springs generate restoring forces and support the stroke process.

The combination of magnetic forces and spring forces is a promising concept for many applications. Fundamental contributions to this approach originate from

LEQUESNE. In [68] different configurations of permanent magnet motors for short strokes are analyzed. The same author observes a clearly higher performance of polarized reluctance actuators with restoring springs for high-frequency oscillating applications in [67]. The approach is particularly useful for long-stroke actuators.

The comparison and classification of different actuator concepts is the topic of numerous further publications. BOLDEA gives an overview of linear electric actuators and generators [6]. The contribution compares moving coil permanent magnet actuators and linear reluctance actuators. Furthermore, different actuator configurations are discussed. A similar objective has HOWE [36,37]: he discusses different actuator topologies with respect to loss and application potential. The application of electrodynamic and electromagnetic actuators in compressor drives is investigated by BÖDRICH [5]. For the specific application, electrodynamic actuators of moving magnet type as direct drives for oscillatory motion show advantages when compared to polarized actuators based on surface boundary forces. The investigation of linear motor topologies for reciprocating vapor compressors is also the topic of WANG [115]. A configuration with a quasi-Halbach magnetized armature and a slotted stator is evaluated best. A comparative study of single-phase permanent magnet oscillating actuators is carried out by CHEN [14]. He assesses the electromagnetic performance and evaluates the properties of different configurations.

Finally, CLAEYSSEN focusses on a direct comparison between controllable moving coil and moving iron actuators [16]. According to the results of the contribution, moving iron actuators offer a higher force to power and a higher force to mass ratio. In addition they are more robust and therefore an interesting alternative for applications such as anti-vibration control.

Related Work

This thesis is part of continuous research activities in the field of electromagnetic actuators under the supervision of ULBRICH in Braunschweig, Essen and Munich. The contributions presented here are based on reluctance drives, which were originally designed for active vibration damping in conventional machinery. The rising field of mechatronics promised new prospects of machine optimization by a combination of mechanics, actuators and intelligent control [110].

Over the years, applications in various mechanical engineering fields were investigated. An interesting example from rotor dynamics is the work of GINZINGER who uses the developed reluctance actuators in an active auxiliary bearing for the control of a rubbing rotor [29].

Furthermore, the controlled excitation of systems has been developed as an additional application scenario. The design objectives originally formulated by ULBRICH were as follows:

- armature stroke $\geq 0.5\,\text{mm}$

- actuation force $\geq 2\,\text{kN}$

- actuation frequency $\geq 200\,\text{Hz}$

- linear transfer behavior between actuation force and armature stroke

- minimized package space.

Based on these demands WANG developed three different actuator topologies [116]. Key issues are the comparison of coil-generated and permanent magnet bias flux. In addition, different magnet positions are investigated. Particularly the mounting positions in the armature are evaluated as technologically challenging due to potential shock loads on the brittle magnetic material. While the configuration with a permanent magnet bias is evaluated best with respect to the actuator performance, the resulting negative magnetic stiffness causes an inherent instability. Furthermore, the application of different magnetic materials is investigated. The use of special soft magnetic alloys increases the obtainable force dynamics considerably. An evaluation of static and dynamic actuator properties completes the work.

OBERBECK continues the research and analyses the developed magnetic systems using magnetic equivalent circuits [78]. Based on his findings, he proposes a topology with a magnet position between two control coils. The fundamental advantage is a low influence of the coil flux on the permanent magnet material, therefore minimizing the risk of demagnetization. The system uses two armature discs in contrast to the central single armature disc of the previous variants. In addition, first feedback control concepts are investigated. The inherent force nonlinearity is compensated by a static feedback linearization, such that a proportional current-force transfer function is obtained.

The thesis of HERRMANN focuses on the systematic design and control of electromagnetic actuators [33]. He adopts the basic topology presented in [78] and proposes a design method based on magnetic equivalent circuits with different modeling depth. Moreover, he analyzes the developed system numerically by means of finite element field calculations. A major contribution is the linear modeling of the electromagnetic energy conversion by linear time invariant (LTI) systems in the frequency domain. Based on these results, different feedback control methods aiming at trajectory tracking are investigated and evaluated. The research efforts lead to the development of a high-performance actuator which is mainly restricted by the inherent instability due to the magnetic bias and by eddy currents in the solid core at high frequency operation. The developed actuator is used for the controlled excitation of vibrations. Quality control and the analysis of products for disturbing noises are suggested as potential application fields.

Parallel to this thesis, the industrial application of vibration test rigs for cars and components is further continued by KOCH [53–56, 58]. He develops test rigs based on reluctance actuators designed in [33] and later in the course of this work. For this purpose different control concepts, which incorporate the inherent coupling of several actuators by the test object, are applied and compared. High tracking quality is ensured by implementation of multivariable time waveform replication (TWR) algorithms. Furthermore, the application of magnetic reluctance actuators in vibration test rigs is evaluated from a practical perspective. A comparison to hydraulic test rigs shows that test rigs based on magnetic reluctance actuators yield equivalent tracking results and are thus an interesting alternative to existing concepts [57].

1.2. Contributions and Outline of the Thesis

The main objective of this thesis is the mechatronic design of magnetic reluctance actuators for vibration testing. The combination of the individual fields of magnetic, electric and mechanical design with suitable information processing enables the development of high-performance actuators for the controlled excitation of vibration. For this purpose, a systematic design process based on analytical and numerical magnetic circuit models is proposed. An energy-based modeling approach allows for the accurate prediction of the inherently nonlinear actuator characteristics in dynamic simulations. The realization of two different prototypes serves for the validation of the proposed design methods.

The contribution is organized in eight chapters. Initially, Chapter 2 gives an overview of the current state of the art in vibration testing and introduces into the field of disturbing noise analysis. Subsequently different actuator concepts for vibration excitation are discussed and compared. The key aspect is the assessment of the application potential of magnetic reluctance actuators in contrast to existing hydraulic and electrodynamic concepts. An overview of the design and operating mode of automotive test rigs finally motivates the development of magnetic reluctance actuators for vibration testing.

Chapter 3 introduces relevant fundamentals of magnetic actuators, primarily the generation of magnetic forces and power losses in magnetic circuits. The reduction of eddy currents due to rapid field variations is essential for enhancing the dynamic performance of reluctance actuators. In addition, modeling methods for the design and simulation are discussed and compared. Apart from well-known analytical and numerical approaches, energy-based methods which are suitable for the accurate prediction of nonlinear force characteristics in dynamic simulations are evaluated.

The magnetic design is the purpose of Chapter 4. Based on the definition of design objectives and requirements on actuators for vibration testing, a suitable topology is proposed. The chapter discusses selection criteria for magnetic materials and strategies for the reduction of eddy currents. A design method for the magnetic circuit based on equivalent networks is developed. A detailed numerical field analysis concludes the magnetic design.

Chapter 5 deals with the energy-based modeling of magnetic systems. A universal model for the dynamic simulation of reluctance actuators is developed on the basis of a numerical computation of co-energy values. A short overview of the energy-based modeling approach for nonlinear systems is complemented by the discussion of approximation methods and the derivation of relevant system parameters. The resulting dynamic multidomain simulation model allows for an efficient prediction of the nonlinear system characteristics.

Chapter 6 discusses mechatronic design aspects which complement the magnetic design of Chapter 4. The design and realization of two prototype actuators is described in detail. Laminated core and armature parts enhance the magnetic performance but strongly influence the mechanical design. A suitable information processing system is presented, which is a prerequisite for controlling vibration excitation. Additionally, experiences gained at each design step are presented, which allow for a better evaluation of the benefits and challenges of magnetic reluctance systems in practical applications.

An overview of experimental results and the validation of the proposed design methods is given in Chapter 7. Furthermore, the setup of a suitable test rig for the precise measurement of high reluctance forces is described. Both prototype actuators are tested in static and dynamic experiments as a preliminary stage of the application in industrial test rigs.

Finally Chapter 8 summarizes the results and gives recommendations for future research.

2. Vibration Testing

The significance of vibration testing in the modern product development process grows due to increasing quality standards and warranty costs. An important field of application in the automotive industry is the analysis of cars and their components for annoying noises. For this purpose special vibration test rigs are required. Hydraulic and electrodynamic actuators, which are also called shakers in this context, are widespread as drives in industrial applications.

This chapter illustrates the application potential of electromagnetic reluctance actuators for vibration testing and provides the motivation for the development of reluctance shakers in Chapter 4. First of all, an overview of industrial vibration testing and the analysis of products for disturbing noise is given. The comparison with established hydraulic and electrodynamic drive concepts allows for an evaluation of the reluctance principle with respect to vibration testing. Therefor, the functional principle, the properties and typical applications in automotive vibration testing are discussed. Essential criteria are the achievable force density, force characteristic and stroke. Furthermore, the implications on the design of test rigs are described.

An introduction to vibration test rigs is intended to serve as basis for the derivation of design objectives for magnetic reluctance shakers. Both test rigs for components and for vehicles are considered. Different designs allow for the adaption to the requirements of the respective analysis situation.

2.1. Noise, Vibration and Harshness Analysis

The acoustic performance of products significantly influences the quality perception of consumers. Growing customer demands have led to extensive noise, vibration and harshness (NVH) analysis with the aim of improving the overall sound quality. Acoustic noise is the unwanted sound that causes audible disturbances. Vibration is a mechanical oscillation which leads to noises and disturbance. The term harshness is used to quantify the discomfort and severity associated with both noise and vibration [114].

In automotive engineering, disturbing noises are sounds inside the passenger compartment which are not caused by the operation of the vehicle or the vehicle components. The terms for disturbing noises are often of colloquial and onomatopoeic nature. Noises generated by the contact of adjacent parts can be grouped into impact noises (rattle, buzz), stick-slip noises (creak, click, squeak) and others [123]. Typical sources for impact noises in the car are the glove compartment and sun roof. Stick-slip noises are generated e.g. by door seals, if a distortion causes a relative movement between door and frame.

In contrast, operational noises arise from the normal operation of the car and can even mask disturbing noises in some cases. However, the ongoing reduction

of the masking noises of engine, powertrain and airflow raises the demands on a low-noise passenger compartment. The emergence of silent hybrid and full electric cars will accelerate this trend considerably. Finally, the analysis and elimination of disturbing sound plays an important role, particularly in terms of competitiveness, since customers typically equate sound and product quality [28]. Due to the growing customer demands and increasing competition, the NVH analysis has a high priority and is often carried out in an early phase in the product development cycle in order to avoid follow-up costs.

The NVH engineering process is typically composed of three phases [48, 53]:

1. virtual analysis

2. component testing

3. vehicle testing.

For virtual analyses computer aided design (CAD) systems are used which enable the identification of critical components and assemblies for static contacts. The NVH potential is estimated on the basis of the component distance, assembly properties and surface hardness [75]. However, the method neglects the excitation and the component dynamics so that the results are only of limited use for noise validation. In order to enhance the disturbing noise prediction, research focuses on finite element (FE) analyses and analytic models which allow for a detailed calculation of the noise emission. However, these methods alone are currently not sufficient for an adequate NVH validation.

Therefore, the experimental examination of components and vehicles makes up a large part of the overall NVH analysis activities. Specialists analyze single components, larger modules and finally the entire vehicle during test drives for disturbing noises. Special rough road tracks are used for the test drives. Typical road surfaces include cobblestone pavements, Belgian block, wash board surfaces or artificial sinusoidal profiles.

For time to market and cost reasons, the testing activities are increasingly shifted towards laboratory experiments. Here, road drives are reproduced on vibration test rigs. For this purpose acceleration profiles, representing the excitation of the car by the road surface, are recorded during real test drives. These serve as basis for the calculation of so-called drive files which are the command signal in the test rig, where the road-like excitation is then provided by actuators. Feedback control systems ensure a high tracking quality, so that the actual acceleration of the car or its components in the test rig is identical to the road drive, cf. Section 2.3. The advantages of road simulations on excitation test rigs in comparison with real test drives are as follows (extended from [53]):

- Climatic chambers allow for defined environmental conditions during the test.

- Unwanted masking noises are reduced. No influence of tire, powertrain and airflow noises.

- A single operator is sufficient for the analysis. For road drives at least two persons are required: a driver and the analysis specialist.

- Analyses outside of the passenger compartment are possible.

- The experiments are reproducible.

- A defined artificial aging can be carried out: in contrast to real road drives the car can be subjected to stronger excitations, harsher environments and the test rig can be operated day and night without interruptions.

- The experimental effort is significantly decreased: transfer drives to testing facilities and the disguise of prototypes are not necessary. Furthermore there is no risk of damaging or soiling the vehicles as it is the case during road drives.

Currently, most NVH activities are concentrated on the car development phase. An additional future application of vibration test rigs will be their integration as end-of-line test during the production of new vehicles. For this purpose, small, reliable and cost-effective actuation systems will be required.

2.2. Actuators

The key elements in the vibration test rigs are the driving actuators. They convert the control signal into the desired mechanical motion and are thus the connecting links between the information processing part and the mechanical part of the mechatronic system. Due to their relevance and the variety of the underlying physical principles, a vast number of actuator types have been realized in the history of technological development. Besides classical magnetic, hydraulic and pneumatic actuators, new operating principles have been investigated in recent works. These include piezoelectric, magnetostrictive and electrostrictive actuators, electrochemical actuators, the use of fluids in electro- and magnetorheological actuators and the investigation of shape-memory materials [38, 40, 42]. Overall, the number of development approaches correlates with the wide field of feasible physical principles and their application.

According to [40], the different operating principles can be grouped into energy controllers and energy converters. Energy controllers depend on an additional power supply which provides the output energy by means of auxiliary media such as hydraulic fluids or pressurized air. The output quantity is energy which is controlled via a low power input variable. Examples for energy controllers include hydraulic and pneumatic actuators. In contrast, input and output of energy converters are both power quantities transporting actuation energy. Electric, piezoelectric and magnetic actuators belong to this group. So far, automotive vibration testing has mainly been using mechanical, hydraulic and electrodynamic shaker systems.

Mechanical shakers are constructed in form of shaking rollers, rotating unbalanced masses or crank mechanisms, which convert rotation into an oscillating translatory motion. In test rigs based on shaking rollers, the vehicle being tested sits on rotating rollers with a defined surface profile. While shaking roller test rigs are relatively easy to realize and resemble the widespread roller dynamometers, they feature a low testing flexibility due to the fixed profiles on the rollers, which require a roller change for the adaption of the excitation. Mechanical shaker systems are not further investigated in this thesis.

Table 2.1.: Typical properties of different actuator principles for vibration testing.

		hydraulic	electrodynamic	reluctance
actuator				
force characteristics		linear	linear	nonlinear
stroke	mm	> 100	< 100	< 10
frequency range	Hz	< 200	> 1000	< 200
force density	N/mm³	high	low	high
noise emission	dB(A)	high	medium	low
actuator size	mm³	small	large	small
robustness		high	medium	high
auxiliary medium		fluid	current	current
test rig				
installation space	m³	large	medium	small
efficiency		low	low	high
maintenance effort		high	low	low
mobility		no	yes	yes

This section compares hydraulic, electrodynamic and electromagnetic reluctance actuators with regard to the application in NVH test rigs [96]. While hydraulic and electrodynamic shaker systems are established and widely used, the application of reluctance shakers is new and complements the existing drive mechanisms [120].

An overview of typical properties is given in Table 2.1, which is adapted from preliminary investigations of Ulbrich [110] and Herrmann [33].

2.2.1. Hydraulic Actuators

Operation Principle

Hydraulic actuators use the energy of a pressurized hydraulic fluid which is typically oil. The pressure of up to several hundred Bars is provided by pressure reservoirs and powerful hydropumps. A basic hydraulic actuator consists of a cylinder with a piston connected to piston rods on both sides as shown in Figure 2.1. The cylinder volume is subdivided into two pressure chambers which are charged with different pressures p_1 and p_2. The fluid flows in and out via valves which allow for the control of the flow rate. Both opposite piston surfaces A_{piston} are subject to pressure, therefore the resulting force depends on the pressure difference Δp between the two chambers [122]:

$$F_{hydr} = \Delta p \cdot A_{piston}. \tag{2.1}$$

The direction of motion is bidirectional and depends on the pressure ratio. The force is proportional to the piston surface and particularly to the pressure difference, which is actively adjusted during operation.

An important aspect is the transmission of force and stroke. The hydraulic operation principle allows for the generation of both high forces and large strokes.
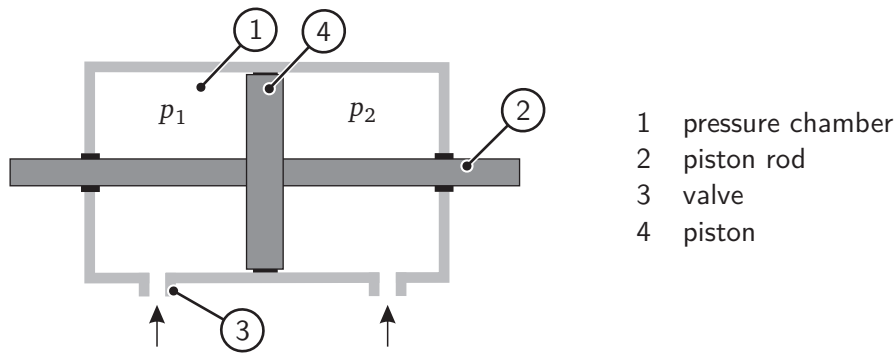
Figure 2.1.: Schematic view of a hydraulic actuator.

1	pressure chamber
2	piston rod
3	valve
4	piston

Properties

The force characteristic of hydraulic actuators is linear with respect to the manipulated variable pressure over the entire stroke range. This facilitates the control considerably; even basic control designs already achieve a satisfying tracking quality. Furthermore, the stroke is not limited by the physical principle. The utilization of the auxiliary medium allows for a significant increase in energy density. As a consequence, the dimensions of the hydraulic cylinder itself are comparably small.

The overall dynamics are primarily limited by the valves and the cylinder. In addition, large inertial forces result from the high mass of the moving fluid. Depending on the load and acceleration profile, in industrial applications frequencies up to a few hundred Hertz are realized. However, in typical NVH test rigs the top frequency limit is considerably lower.

Hydraulic shaker systems typically produce a distinct background noise. Fundamental parameters for the noise emission of a hydraulic actuator are the motor and pump of the pressurizing unit. For this reason both are usually located in separate soundproof compartments. In addition, piston friction and pipe oscillations contribute to the overall sound level [53].

Due to the simple design, hydraulic actuators are very robust. The temperature rise during operation results mainly from the fluid friction in the cylinder. The heat can be either dissipated via the fluid itself or heat exchangers. In general, the shaker efficiency is mainly determined by the hydraulic valves which are used for the power transmission. Typical efficiency factors are up to $\eta = 60\,\%$ [85].

The auxiliary medium ensures a small size of the cylinder itself compared to other actuator types. For operation, however, the hydraulic actuator itself must be complemented by hydropumps, pressure reservoirs, valves and pipes. This has several consequences. The required hydraulic fluid implicates a permanent risk of leakage. The maintenance effort is high owing to the complexity of the plant. This includes the fluid exchange in defined intervals and also the necessary cleaning. The required installation space of the complete test rig is large due to the numerous auxiliary components. Moreover, for the installation in industrial facilities a leakage basin is required which adds to the already high space requirements. Hence, the test rig is in most cases permanently installed and stationary.

Figure 2.2.: CREST road simulator with hydropulser, climatic chamber and floodlight system for the imitation of sunlight [53].

Application

Hydraulic actuators combine high forces and large strokes. Therefore they are primarily deployed in application scenarios where both properties are essential. In the field of vibration testing this includes the earthquake simulation [71, 101], system identification of civil engineering structures [12] and particularly the excitation of heavy vehicles such as trucks [76] or agricultural machines [2, 77].

Component testing usually requires much lower forces. Due to the acquisition cost and the required installation space, hydraulic actuators are used for vehicle tests in most applications. Here characteristic forces of up to 50 kN and maximum strokes of 100 mm are achieved. The obtainable frequencies reach up to 100 Hz.

Car test rigs based on hydraulic actuators are also known as hydropulsers. Figure 2.2 shows a typical shaker plant. The car sits directly on four props which are connected to the hydraulic cylinders. The CREST plant (*Combined Road and Environmental Simulation Test*) excites the car via the wheels and the suspension like the road would do. In order to ensure a realistic excitation, large strokes and high forces are necessary. The test rig allows for both the analysis of the behavior in new condition and the defined aging of the car. Besides the vibration excitation, the adjustment of various climatic conditions is possible. For this purpose, the temperature and humidity influence is simulated by means of a climatic chamber which encloses the testing space. A powerful floodlight system imitates sunlight exposure.

2.2.2. Electrodynamic Actuators

Operation Principle

Electrodynamic actuators are based on the electrodynamic force principle, from which the name is derived. The functional principle uses the LORENTZ force on a moving charge in the magnetic field. The generation of an electrodynamic force occurs if a

current carrying conductor is located in a quasi-stationary magnetic field [104]. The resulting force for a conductor with an effective length l in a magnetic field with flux-density B for a given current i is given by

$$F_{ed} = Bli = k_f i. \tag{2.2}$$

Here k_f denotes the force constant which determines the achievable force per current. The calculation assumes the orthogonality of current direction and magnetic field. The electrodynamic force is proportional to the applied current, and an inversion of the force direction is achieved by current inversion. A detailed derivation from the electromechanic stress tensor is given in Section 3.1.

For technical applications the physical principle is exploited in voice coil actuators, see Figure 2.3 for a schematic view. A moving coil is positioned in the working airgap which forms the output side of the shaker. The required magnetic field is generated by a permanent magnetic excitation. For larger shakers, field generating coils are used instead of permanent magnets for cost reasons. In that case, both the field coil in the stator and the voice coil in the armature contribute to the electric power loss. The field is guided by the iron yoke and crosses the airgap perpendicularly to the concentric mounted voice coil [64]. Radial stiff and axial compliant flexures support the voice coil mechanically. Thus the electrodynamic force leads to a displacement in axial direction, while an eventual tilting in other directions is avoided [62]. The flange for the test loads is directly connected to the moving coil.

Properties

The force characteristic of an electrodynamic actuator is proportional to the actively adjusted voice coil current, see (2.2). Therefore, basic control concepts can be applied to ensure the tracking quality in test rigs. In less demanding applications the controller can be omitted and replaced by a simple voltage command. The coil current is the limiting factor for the force generation in large parts of the operating range since the maximum coil current cannot be arbitrarily increased due to the resulting heating. The stroke is not limited by the physical principle and typically ranges from
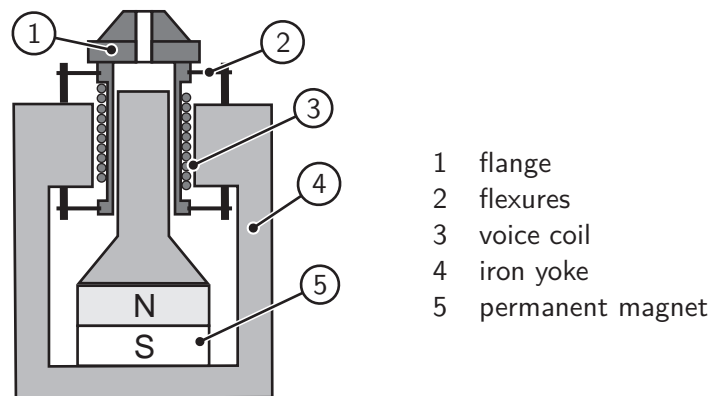

1   flange
2   flexures
3   voice coil
4   iron yoke
5   permanent magnet

Figure 2.3.: Schematic view of an electrodynamic actuator.

a few millimeters up to 100 mm in long stroke versions. Due to the good scalability, electrodynamic shakers are available in numerous size and power classes.

The most prominent feature of electrodynamic shakers is the large frequency range in which oscillations can be generated. Depending on the actuator size, different frequency ranges are given in the literature [59, 85]. Typical frequency limits range from approximately 30 kHz for small shakers to a maximum frequency of 5 kHz for larger shakers. Since the armature is designed iron-less and consists basically only of the voice coil, the moving part is light-weight and enables high dynamic motions.

The actuator itself operates virtually noiseless. However, depending on its design the required cooling system can produce a disturbing background noise. The comparatively low force constant k_f demands for considerably high coil currents in applications which require high accelerations or the actuation of heavy loads. Depending on the shaker size and power class, either air cooling or water cooling systems are used. The temperature rise limits the feasible current and the force during permanent operation. The main problem during the operation is the heat discharge. If the masking noise of active cooling systems is not acceptable for the respective application, passive cooling must be used. In that case restrictions apply to the maximum duty cycle of the shaker.

In order to ensure the energy supply, a current lead to the moving voice coil is required. This is a major design drawback with respect to the robustness of the actuator, because the electrical connection must withstand the vibration.

The main parameters which determine the overall size of an electrodynamic actuator result from the equation for the LORENTZ force. Besides the variable current and the given magnetic field density, the LORENTZ force depends mainly on the active length of the coil. A larger coil diameter and higher winding number increase the active wire length and consequently the resulting force. The physical dimensions of the coil body largely determine the overall actuator size. Since only electrical power is converted, no additional auxiliary medium is required. Consequently, regular time consuming maintenance can be avoided and the operational readiness of the system is high.

The required high coil currents produce a significant winding loss. In addition, the losses in the cooling system and the power amplifier deteriorate the overall efficiency of the test rig [63]. Generally electrodynamic shaker systems are mobile. However, it should be noted that the shaker and the power amplifier used for typical car test rigs require a considerable amount of installation space.

Application

Electrodynamic shakers are widespread in the field of vibration excitation. The existing performance classes range from very small shakers for high frequency applications, as for example in modal analyses, to large shakers with a force vector of several kN for car test rigs.

Important applications in the field of automotive engineering are the artificial aging and NVH testing of components [27, 81, 82]. The required force in these applications is comparatively low due to the moderate weight of typical components, which have to be actuated as loads. However, depending on the particular application, the thermal load makes a cooling system for the shaker necessary. If the shaker and test object are not spatially separated by constructive measures, the cooling system adds to the

Figure 2.4.: Vibration test rig with electrodynamic actuators [53].

background noise in the testing area. Particularly for noise-sensitive NVH testing applications, the operating noise masks the test object noise and therefore affects the detection of the real disturbing noise in examination. The problem can be remedied by a passive noise insulation although this measure involves considerable effort. Alternatively the test must be interrupted for cooling periods. However, this disturbs the test sequence and increases the overall testing time considerably.

Large electrodynamic shakers are also used in car test rigs [10, 44], where the vehicle is usually excited via the jacking points. Other test rig concepts use the excitation via wheels or directly via the wheel hubs. Figure 2.4 shows a test rig based on electrodynamic actuators. In the picture only two of the overall four actuators are visible. The car sits on the wheels; this way the assembly avoids the static loading of the shaker system. The shakers are positioned adjacent to the vehicle. The connection to the test object is achieved via a simple lever construction, which enables a force transformation. The shaker itself is mounted in a top-down configuration, thereby realizing the required height compensation to the jacking point level. The holding frame is designed as a massive steel construction considering the high actuation forces and the weight of the actuators. Despite the considerable actuator size, the overall setup is significantly smaller compared to the hydraulic test rig described above. Therefore, mobile test rigs can be generally realized. However, for the operation large power amplifiers are necessary. These often require more installation space than the actual shakers and must be considered in the conceptual design of test rigs.

2.2.3. Magnetic Reluctance Actuators

Operation Principle

In contrast to electrodynamic actuators, which use the LORENTZ force on current-carrying conductors, electromagnetic reluctance actuators are based on reluctance forces (Maxwell forces). These occur at the boundary surfaces of materials with different magnetic permeability, which are subject to a magnetic field. Classic applications of reluctance forces include small clamping magnets in the household or the widespread solenoids in industrial automation. If the magnetic voltage drop in the iron parts of the actuator is neglected, the reluctance force is given by

$$F_{rel} = \frac{B^2 A_{Fe}}{2\mu_0} \tag{2.3}$$

where A_{Fe} denotes the iron surface penetrated perpendicularly by the magnetic flux density B. The force is always attractive, since the system aims at the minimization of the working airgap (energy minimum). A further discussion of the force generation with regard to the design of magnetic actuators is given in Section 3.1. In the following, the characteristics of electromagnetic reluctance actuators for vibration excitation are reviewed.

Properties

The reluctance force is nonlinear with respect to the air gap length and the applied coil current due to nonlinear material characteristics. Consequently, in most cases simple control methods (e.g. proportional-integral-derivative controllers, PID) are not sufficient to ensure a good tracking quality of given reference profiles. Since only attractive forces can be generated, the armature restoring force must be provided by springs or alternatively by adding a second magnetic actuator with opposite direction. The force generation depends on the inverse square of the airgap length; therefore the achievable stroke in practical applications is restricted, which is a major disadvantage of reluctance actuators. However, for the specific case of NVH testing the stroke limit is not relevant as shown in Section 4.2. The obtainable force can be enhanced by increasing the armature surface or the magnetic field density. Actuators with high force densities and small strokes are realizable, which facilitates the design of very compact shakers. This advantage becomes particularly apparent in comparison to electrodynamic shakers.

The dynamics of reluctance actuators depend mainly on the inductivity of the magnetic circuit and the applied driving method. A high dynamic force generation depends on a fast variation of the magnetic field. Eddy currents in the flux-guiding iron parts influence the actuator dynamics considerably. Therefore, suitable countermeasures such as the use of laminations or slotted parts are essential for the design of high performance shakers. The moving armature consists in large parts of flux-guiding iron as well. Although the achievable bandwidth (typ. 150 Hz) is lowered by the associated weight, the impact is less significant when actuating heavy objects such as cars. The overall dynamics and the maximum actuating frequencies are clearly lower

in comparison to electrodynamic actuators. However, the achievable frequency range of reluctance shakers is well suited for automotive NVH testing.

A suitable thermal design of the coil systems avoids the need for an active cooling system, while the overall actuator dimension can be still kept small due to the high force density. For the operation small coil currents (up to 8 A) are necessary. The reluctance shakers developed in this thesis feature a power consumption of 640 W for a quasi-static peak force of 8 kN. The exclusive passive cooling enables the application in noise-sensitive NVH testing scenarios without further effort for noise insulation. However, a sealing of the casing against dirt and moisture can cause a problematic temperature rise, since the air circulation is suppressed.

As in the case of rotating reluctance motors (switched reluctance machines, SRM), a simple and robust design is realizable. In particular, the moving armature consists of iron only and carries no windings. Since the field-producing coils are located in the stationary core, the power connection is stationary.

The high force density and the low power consumption allow for the design of very compact vibration test rigs. Installation space for hydropumps and leakage prevention measures as in the case of hydraulic test rigs are not required. The compact reluctance actuators also fit into existing test structures. In contrast to electrodynamic shakers, no large fixation frames are necessary due to the low weight (65 kg). This facilitates the design of multiaxis vibration test rigs considerably. An integration of power and control electronics makes the realization of mobile shakers possible. Due to the low wear, maintenance cycles are long and mainly determined by the fatigue strength of the armature springs.

2.3. Vibration Test Rigs

The test rigs, which are described in this section, evolved from a close cooperation between academic research, test rig manufacturers and end users. Preliminary design considerations resulted in first component test rigs with reluctance force actuators in an academic laboratory environment [33]. The collaboration with development departments of a car manufacturer[1] enabled the incorporation of practical testing demands and the application of developed shaker prototypes in an industrial environment. The mechanical construction, the design of the control hardware and software and the assembly of the different test rigs have been carried out by professional test rig manufacturers [2]. As a result of this fruitful cooperation, different component and car test rigs were realized for industrial purposes.

2.3.1. Components

The analysis of components is carried out on component test rigs, where the focus lies on rattling sounds. Typical automotive test objects include glove compartments and instrument panels. In addition, larger modules such as complete doors and seats are analyzed. The test procedure is usually structured in three steps [53]:

---

1 BMW AG
2 AKE-technologies GmbH, MAHA-AIP GmbH & Co. KG, KE Knestel Elektronik GmbH

1. NVH analysis of the component in original condition (one-dimensional excitation direction, usually vertical)

2. artificial aging by defined vibration excitation (three-dimensional, usually sequential)

3. further NVH analysis of the component in the artificially aged condition (one-dimensional excitation direction, usually vertical).

Additionally, environmental influences on the noise and aging characteristic of a component can be investigated using climatic chambers.

Figure 2.5 shows different component test rigs based on magnetic reluctance actuators. The basic setup is similar for each test rig. The shaker is flanged to a steel base plate and drives the test rig frame via a coupling rod. The frame itself must be both rigid in order to avoid additional unwanted oscillations and light-weight since its own weight adds to the accelerated mass. The frame sits on air bellows which inhibit unwanted tilting movements and carry the static weight. In neutral position the shaker experiences no load. Therefore, a temperature rise due to stationary coil currents is avoided. Aluminum profiles enable the fast mounting of different specimen. Due to the small size, the actuator can be directly positioned below the test rig frame allowing for a low overall height.

Transport simulation is another important application (see Figure 2.5). The cargo shipment over rough roads can be reconstructed in a laboratory environment. The motivation is similar to the NVH testing scenarios: avoiding real test drives out of time and cost reasons. Trial shipments are not only time-consuming and expensive but also not entirely objective, since the actual road conditions might vary and the cargo is subject to different climatic conditions. With this method the packaging can be tested and freight damages be avoided. In addition, the approach allows for the development of new packagings and their optimization. Reluctance shakers are well suited for packaging tests, since their high forces enable the actuation of even heavy loads.
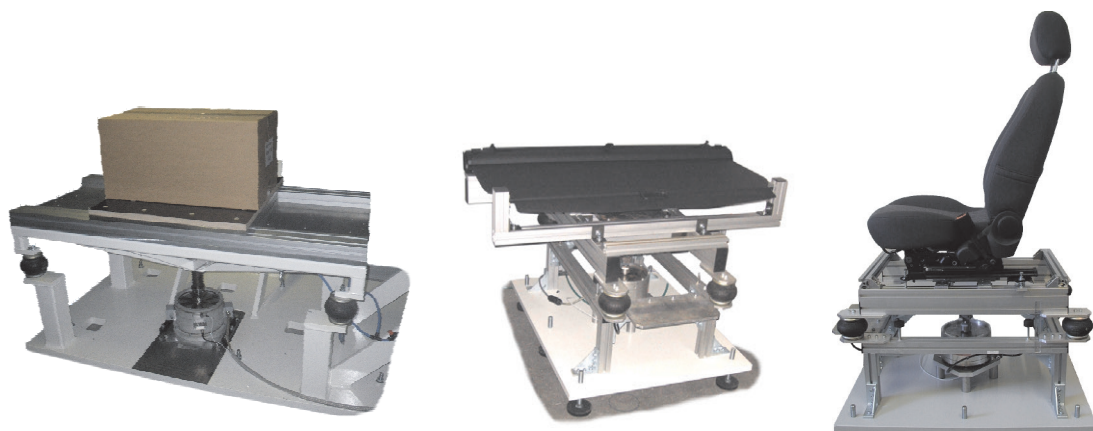

Figure 2.5.: Transport simulation and component test rigs with magnetic reluctance actuators.

2.3.2. Cars

The analysis of components for disturbing noise is fundamental for the development of cars with a high quality appearance. Nonetheless, component testing alone does not ensure the NVH quality of the overall product, since a typical vehicle consists of thousands of components and the assembly introduces numerous additional sources of disturbing noise. Therefore, car test rigs are used for testing the entire vehicle.

An important aspect with regard to the application of reluctance shakers is the type of excitation and force transmission in the test rig. Here, two major methods are used in practice as illustrated in Figure 2.6. When excited via the wheels and the chassis, the vehicle sits directly on the driving props. The car body is thereby loading the wheels and chassis in a normal way. Since the entire weight of the vehicle rests on the props, the driving actuators must provide high forces. In addition, large strokes are necessary, since the excitation path includes the suspension of the vehicle. For this configuration usually hydraulic actuators are used. The main advantage is the realistic excitation of the car via the wheels which resembles a real road drive.

Due to their physical principle, reluctance shakers cannot provide the required strokes for a sufficient wheel excitation. Consequently, the concept of direct body excitation (DBE) is preferred for the actuator integration in the test rig. The car is supported via wheels and chassis either by car lift platforms or the ground. The vehicle weight is fully sustained and does not rest on the actuation system. The actuators are statically unloaded, thus avoiding stationary currents and the associated heating. Furthermore, due to the direct excitation of the frame, the required forces and strokes are significantly lower compared to the excitation via wheels and chassis as shown in Section 4.2. The main disadvantage is the unrealistic excitation method which omits wheels and suspension in contrast to a real road drive. Nevertheless, the application of suitable control concepts ensures a realistic excitation of the vehicle interior [57].

As coupling points the jacking points are chosen. These are readily accessible during the tests and require no constructional changes to the vehicle. Up to four shakers can be used for the excitation in a push-pull mode. However, jacking points are designed for the transmission of static forces only. When loaded dynamically, the stiffness decreases considerably. Consequently the dynamics of the coupling points must be considered for the design of the shakers and the control of the test rig. The actuators are directly connected to the car via coupling rods which are latched via the bayonet catches in the jack housings.

Figure 2.7 illustrates two different car test rigs based on reluctance actuators. The left picture shows a large test rig with integrated climatic chamber that allows for the
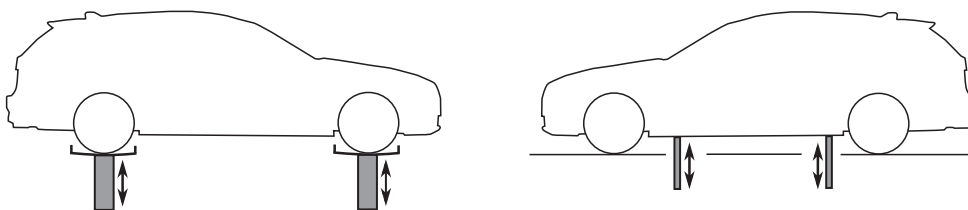

Figure 2.6.: Car excitation via wheels and suspension in comparison to direct body excitation (DBE) [53].

Figure 2.7.: Road simulation with electromagnetic reluctance actuators. Left: test rig
with integrated climatic chamber (actuators not visible) [53]. Right: test rig with lifting
platform.

analysis of temperature and humidity influences. The car sits on the ground while the
actuators and power electronics are located in the subfloor beneath. The coupling rods
protrude into the climatic chamber through slotted holes which allow the adaption to
different vehicle types. The required openings are sealed with inflatable air bellows
in order to protect the actuators against climatic conditions. The test rig uses a four-
shaker configuration, where one shaker drives each jacking point. The operating room
is located outside of the climatic chamber and allows for visual monitoring via an
additional window to the testing area.

The right picture in Figure 2.7 shows a smaller and more cost-effective alternative.
Here the car sits on a car lift. The omission of the climatic chamber enables a compact
design which facilitates the integration into existing test areas or production lines. The
test rig uses a two shaker configuration, the coupling rods are latched pneumatically
in the jacking points. The shaker units are movable and allow for the adaption to
different wheelbases and tracks. Strong holding magnets fixate the shakers in their
final position on the base plate of the test rig. An additional casing shields the actuator
and its sensors from dirt and water dripping of the vehicle underbody.

In order to ensure the tracking quality at different positions in the vehicle interior,
an advanced control system is required. The use of multiple shakers necessitates
a multiple-input multiple-output (MIMO) control design. The car body causes a
strong coupling between the individual actuators. Hence, decentral controllers are not
sufficient. KOCH [53] implements a MIMO control concept with a reduced observer
which allows for a significant reduction of the required sensor amount. A TWR
algorithm ensures the tracking quality of the controller.

2.4. Chapter Summary

This chapter has provided an introduction into the vibration testing during NVH
analyses of cars and components. In order to avoid test drives, road simulations using
special vibration test rigs are state of the art. In these testing stations, the excitation
is provided by powerful actuators. The simulation of real road drives in a laboratory

environment enables significant improvements of the noise examination. A comparison of hydraulic, electrodynamic and electromagnetic drives is given and illustrates the application potential of magnetic reluctance shakers. The reluctance force principle complements the existing actuation concepts and fulfills the demand for compact actuators for vibration excitation.

Key features for the application of actuators in vibration test rigs are the avoidance of active cooling systems and the risk of leakage. In addition, the required installation space and the maintenance effort should be low. Reluctance force actuators fit into that niche of requirements, exhibiting a high force density and robustness. The energy supply is electric current, which is easily available in industrial environments.

An overview of test rig concepts for the vibration excitation of components and vehicles finalizes the chapter, providing the basis for the specific design of magnetic reluctance shakers in the following. The main drawback of reluctance actuators for the application as shakers is the stroke limitation due to the physical concept. By choosing an appropriate excitation method, this limitation can be compensated. The direct body excitation (DBE) of vehicles via the frame instead of the wheels and suspension enables a sufficient excitation of test objects with comparatively small strokes. Thus the application of magnetic reluctance actuators provides an alternative to hydraulic or electrodynamic test rig solutions.

3. Magnetic Reluctance Actuators

The knowledge required for the design and development of magnetic reluctance actuators is extensive and comes from all fields of mechatronics. This chapter briefly reviews the fundamental principles of magnetic force generation with a special focus on reluctance forces. Moreover, fast actuation requires a rapid change of the force generating magnetic fields. In order to achieve high actuator dynamics the investigation of frequency-dependent phenomena is essential.

Power losses reduce the bandwidth and energy efficiency. For a better understanding, the main loss mechanisms in the windings and the iron parts due to eddy currents and hysteresis are illustrated. Here, solid and laminated cores are considered and the basis for the design of high dynamic magnetic cores in Chapter 4 is established.

Furthermore, methods to model static and dynamic actuator properties are discussed. For this purpose, reluctance circuits are compared to the finite element analysis and a reduced order model.

3.1. Magnetic Forces

Based on MAXWELL's equations, the magnetic force f_{mv} per unit volume can be expressed as the divergence of an electromechanic stress tensor T of the electromagnetic field [100]. If the magnetic permeability μ depends on the material density ρ_0 and only magnetic fields are considered, the tensor is written as [70]

$$f_{mv} = \nabla \cdot T \tag{3.1}$$

$$T = \mu H H^T - \frac{\mu}{2} I H H \left(1 - \frac{\rho_0}{\mu} \frac{\partial \mu}{\partial \rho_0} \right). \tag{3.2}$$

Here H denotes the magnetic field strength and I the unit tensor. Expanding and rearranging finally yields the total force density f_{mv}, which can be split up in four divergence and gradient terms [13, 47]:

$$f_{mv} = f_{mv1} + f_{mv2} + f_{mv3} + f_{mv4} =$$
$$= \frac{1}{2} \nabla \cdot \left(H^2 \rho_0 \frac{\partial \mu}{\partial \rho_0} \right) - H \nabla M + J \times B - \frac{1}{2} H^2 \nabla \mu. \tag{3.3}$$

The first term

$$f_{mv1} = \frac{1}{2} \nabla \cdot \left(H^2 \rho_0 \frac{\partial \mu}{\partial \rho_0} \right) \tag{3.4}$$

describes the force caused by the density-dependent permeability $\mu(\rho_0)$ of the material in a magnetic field.
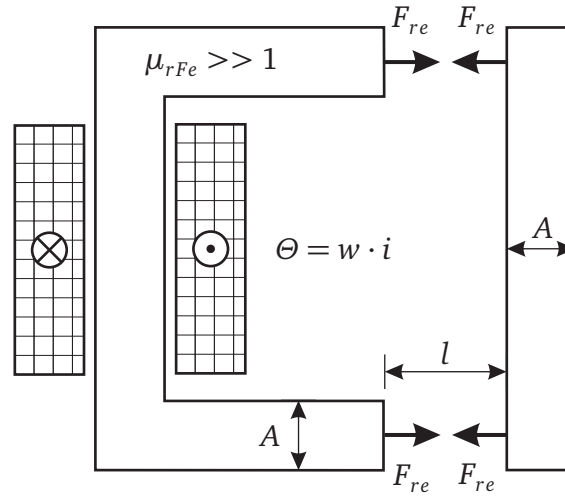
Figure 3.1.: Basic reluctance actuator.

This phenomenon is used in magnetostrictive actuators. The second term in (3.3) specifies source force density

$$f_{mv2} = -H\nabla M \tag{3.5}$$

of polarized magnets with magnetization M. This force contribution has to be incorporated if permanent magnets are used as magnetomotive force (MMF) sources in magnetic devices.

From an engineering perspective the third and fourth term are the most important with respect to technical applications.

$$f_{mv3} = J \times B \tag{3.6}$$

denotes the electrodynamic force on a current density J under the influence of a magnetic field B. Using the current-density

$$J = \rho_s v \tag{3.7}$$

with space-charge density ρ_s and charge-carrier velocity v and the overall charge per volume

$$Q = \int_V \rho \, dV, \tag{3.8}$$

the familiar expression for the LORENTZ (electrodynamic) force is written as

$$F_{ed} = Q(v \times B) = l(i \times B). \tag{3.9}$$

The term electrodynamic refers to the concept of a moving electric charge as basis for the force development. This force component is used in electrodynamic actuators by applying a current i to an elastically suspended coil, see Section 2.2.2. Common

applications include rotating motors and generators. Important applications in the linear case are linear drives and voice coil actuators. In the field of vibration excitation LORENTZ forces are widely used in electrodynamic shakers.

Key advantages of voice coil actuators are reversible forces and a linear behavior with respect to magnetic induction and to the driving current i in particular. Furthermore, they allow for large strokes since there is no direct dependency between the displacement of the coil and the created forces.

The core principle of the magnetic reluctance actuators considered in this thesis is specified by the fourth term

$$f_{mv4} = -\frac{1}{2} H^2 \nabla \mu \tag{3.10}$$

which describes the magnetic force due to a change in permeability $\nabla \mu$. For two materials with different permeability the resulting reluctance force is calculated as

$$f_{ma} = \frac{1}{2}(\mu_2 - \mu_1)(H_{t1}^2 + \frac{\mu_1}{\mu_2} H_{n1}^2) \cdot n. \tag{3.11}$$

Here f_{ma} is a surface force density with n being the normal vector to the surface. The force vector f_{ma} is directed from the material with higher permeability (μ_2) to the material with lower permeability (μ_1) to reduce energy in the system [61].

The most common case of technical applications is the boundary between iron ($\mu_2 = \mu_r \mu_0$) and air ($\mu_1 = \mu_0$), which can be written as

$$f_{ma} = \frac{\mu_r - 1}{2\mu_r \mu_0}(B_n^2 + \mu_r B_t^2) \cdot n \tag{3.12}$$

with B_n and B_t as the normal and tangential components of the magnetic field on the air side of the boundary. μ_0 denotes the vacuum permeability and μ_r the relative permeability of the material. In magnetic actuators the working airgaps are usually rather small so that the magnetic field passes perpendicularly through the relevant armature surfaces and the tangential component B_t can be neglected. In order to yield a high energy efficiency and small setup, materials with high permeability $\mu_r \gg 1$ are used for the magnetic circuit, which leads to the following simplification

$$f_{ma} = \frac{1}{2\mu_0} \cdot B^2. \tag{3.13}$$

Finally the reluctance force

$$F_{rel} = f_{ma} \cdot A = \frac{B^2 A}{2\mu_0} = \frac{\Phi^2}{2\mu_0 A} \tag{3.14}$$

is obtained from the force density f_{ma}. Here A denotes the pole surface area and Φ the magnetic flux.

In the case of a simple reluctance actuator as shown in Figure 3.1, a magnetomotive force MMF $\Theta = w \cdot i$ is produced in a winding of w turns by a current i. Together with

the airgap length l the reluctance force F_{rel} is then given by

$$F_{rel} = \frac{1}{2}\mu_0 A \frac{\Theta^2}{l^2}.$$ (3.15)

In contrast to electrodynamic forces, reluctance forces are attractive only and always reduce the effective airgap. Therefore, the force is nonreversible. Besides, the maximum stroke is limited due to the reciprocal dependency on l^2. Additionally, reluctance actuators exhibit an inherent nonlinearity with respect to MMF Θ and particularly to the airgap l, which makes modeling and control more difficult. However, high forces can be achieved by increasing the iron surface A. Typical applications include all kind of solenoids, as well as proportional, lifting and switching actuators (relays). Rotating electrical drives based on the reluctance principle are called switched reluctance machines.

3.2. Magnetic Induction

According to the axioms of classical electrodynamics a time-varying flux involves a curl of the electric field E. FARADAY's law of induction states that the electromotive force (EMF) is proportional to the rate of magnetic flux change [39]. The voltage induced in a single conductor loop is given by the flux variation

$$u_i = \oint_{l_s} E \, dl = -\frac{d\Phi}{dt}.$$ (3.16)

The voltage is induced regardless of the source of flux variation [61]. For technical systems with several relevant coil windings, the flux linkage

$$\Psi = w \cdot i$$ (3.17)

as a product of winding number w and coil current i is introduced. The equation for a simple coil with resistance R excited by voltage u is given by

$$u = R \cdot i + \frac{d\Psi}{dt}.$$ (3.18)

There are two feasible scenarios for voltage induction. First, a flux change might be caused by an additional coil (mutual inductance) or permanent magnet (external inductance). Second, a flux change can be provoked by the coil itself (self-inductance). In reluctance actuators the flux linkage is a nonlinear function of armature position x and coil current i [47], which yields

$$u = R \cdot i + \frac{d}{dt}(\Psi(x, i))$$ (3.19)

$$u = R \cdot i + \left(\underbrace{\frac{\mathrm{d}\,\Psi(x,i)}{\mathrm{d}\,x} \cdot \frac{\mathrm{d}\,x}{\mathrm{d}\,t}}_{u_{ix}} + \underbrace{\frac{\mathrm{d}\,\Psi(x,i)}{\mathrm{d}\,i} \cdot \frac{\mathrm{d}\,i}{\mathrm{d}\,t}}_{u_{ii}} \right). \tag{3.20}$$

The two terms express the major induction sources that contribute to voltage genera-tion. Flux change and induced voltage u_{ii} are the result of current variation in the coil. But also during the resulting armature motion a flux variation is caused inducing u_{ix}.

If the position-dependency is neglected $^{d\Psi}/_{dx} = 0$ and a linear relation between flux and current assumed $^{d\Psi}/_{di} = \mathrm{const.} = L_0$, (3.20) can be simplified to

$$u = R \cdot i + L_0 \frac{\mathrm{d}\,i}{\mathrm{d}\,t}. \tag{3.21}$$

Here L_0 denotes the self-inductance of the coil. Hence the solution for coil current i yields

$$i(t) = \frac{u}{R}\left(1 - e^{-\frac{t}{\tau}}\right) \tag{3.22}$$

with the coil time constant $\tau = {}^{L_0}/_R$. For the operating characteristics of high dynamic reluctance actuators the inductivity and associated time constant plays an essential role since it limits the current rise in the electric circuit and consequently the magnetic force development. The maximum source voltage, coil resistance and inductance are determined during the design process and have to be adjusted to the required actuator dynamic, see Section 4.7 and Section 4.8. The inductance depends on the geometrical shape, dimensions and permeability of the magnetic circuit [84]. It can be rewritten as

$$L_0 = \frac{w^2}{R_m}. \tag{3.23}$$

Here R_m denotes the reluctance of the magnetic circuit, see Section 3.4.1.

However, in the majority of cases the inductance determination is a challenging problem because of the nonlinear dependency on position and current. Modern reluctance actuators feature large airgaps and magnetic circuits which are partly driven into saturation in order to minimize the overall construction size. If nonlinear effects cannot be neglected, the magnetic analysis requires numeric approaches as shown in Chapter 5.

3.3. Power Losses

Power losses reduce the efficiency of actuators and lower the achievable bandwidth. This section describes different approaches to the calculation of winding, eddy current and hysteresis loss in laminated and solid cores.

3.3.1. Eddy Currents

According to FARADAY's law a time-varying magnetic field induces an electric voltage [39]. As a consequence, a circulating current flow occurs in electrically conducting material exposed to the varying field. The term eddy originates from the flow patterns which resemble eddies in turbulent liquids. According to LENZ's law the magnetic field of the induced eddy currents counteracts the original excitation field as both fields interfere. For rapid field changes a displacement of magnetic fields in surface direction occurs, such that there is a field cancellation in the center of the core. This can be also seen as a delay in penetration of magnetization into the core.

For high dynamic magnetic actuators two main consequences arise from eddy current influence. First, the skin effect causes a delayed magnetic force development due to the deferred field development and hence limits the available bandwidth. Apart from that, only a part of total flux carrying volume can be effectively utilized. Therefore, the effective area in (3.14) is reduced. Second, the resulting current flow produces heat which dissipates energy from the magnetic field (eddy current loss).

Due to the undesired consequences, measures for eddy current restraint must be taken when designing fast magnetic actuators, see Section 4.5. The two major solutions consist in either laminating the flux-carrying parts of the magnetic circuit (cutting the conductive path along the induced voltage drop) or using materials with higher electric resistivity. This leads to a faster flux penetration and full usage of iron [3].

Laminated Core

Since laminated steel restricts the flow pattern of eddy currents to the volume of one sheet, the associated loss is not completely eliminated but significantly reduced [9]. For skin depths (see Section 3.3.2) smaller than lamination thickness t, the power loss caused by eddy currents obeys to

$$P_e = \frac{\pi^2}{6} t^2 f^2 B^2 \sigma V. \tag{3.24}$$

Here P_e denotes the eddy current loss, f the operating frequency, σ the electrical conductivity and V the volume of the flux-guiding material. The order of the various terms in (3.24) is essential since it determines the influence on the total power loss. Lamination thickness, frequency and flux density contribute with the square whereas the loss is only proportional to the material's conductivity. Thus, the reduction of the lamination thickness is an effective measure for eddy current attenuation.

Solid Core

For solid cores (3.24) does not hold anymore. [91] provides a convenient approximation for cylindrical solid cores which are frequently used in rotation-symmetric actuators. The model is based on the assumption that hysteresis loops of the material can be approximated by equivalent ellipses. The semi-cutoff frequency

$$f_{sc} = \frac{2}{\pi r_c^2 \mu \sigma} \tag{3.25}$$

of a core with radius r_c separates the high frequency range from the low frequency range. Above f_{sc} the associated eddy current power loss is significant and modifies the DC characteristics. Thus it is possible to neglect hysteresis. For frequencies below f_{sc} eddy current influence can be neglected and hysteresis is dominant. An approximated eddy current loss model for the entire frequency range is given by

$$P_e \approx \frac{\pi f B_{avg}^2}{\mu} \cdot \frac{f}{2 f_{sc}} \cdot \frac{1}{\sqrt{1 + \frac{(1+\sin\gamma)f}{2 f_{sc}}}}. \tag{3.26}$$

Here B_{avg} denotes the peak value of mean magnetic induction and γ the equivalent phase lag between magnetic induction and field. For softer materials γ is smaller, so that an anhysteretic material would have $\gamma = 0$. The eddy current loss in solid cores is much higher than in laminated cores. In most cases materials with relatively high conductivity are used (iron: $\sigma \approx 10 \cdot 10^6\,\text{S/m}$), so that the resistance for eddy currents is low. Without further measures (cuts, special alloys with higher resistivity), the bandwidth of solid core actuators is limited.

3.3.2. Skin Depth

Eddy currents cause a field cancelation in the magnetic core during rapid field changes. As a consequence, the flux-carrying parts experience a flux concentration near to the surface while showing a lack of flux in the interior. As a result the outer parts of the core and armature exhibit a larger flux density while the inner volumes are essentially unused and do not contribute to the force generation [9]. This phenomenon is called skin effect. It occurs in all electric conductors and affects both windings and magnetic circuit. For the design of magnetic devices in this thesis, only the impact on the magnetic core is considered. However, for very high frequencies (above approx. 10 kHz) the skin effect in the coil must be taken into account as well.

An important criterion for the assessment of eddy current influence is the skin depth

$$\delta_s = \frac{1}{\sqrt{\pi f \mu \sigma}}. \tag{3.27}$$

Here δ_s denotes the depth at which the flux density has decayed to 36.8 % of its surface value. Therefore, it is a measure for the field penetration. The decay is exponential [84], the total depth of field penetration being approximately $4\dots8\delta_s$ [61]. The skin depth is inversely proportional to the square root of frequency. Thus δ_s is large for low frequencies. For higher frequencies though, a rapid decrease in field penetration depth occurs. The reciprocal dependency on the square root of magnetic permeability and electric conductivity means a further decrease in penetration depth, since a high permeability $\mu = \mu_r \mu_0$ is desired for typical soft-magnetic materials (iron: $\mu_r \approx 300\dots10000$). To facilitate flux penetration and full iron usage, soft-magnetic materials are often alloyed with other elements (nickel Ni, silicon Si) in order to reduce the electrical conductivity. During the design process the calculation of the skin depth can be used for the determination of the required lamination thickness, cf. Section 4.6.

For actuators with solid cores it provides a basic benchmark for the impact of eddy currents.

3.3.3. Hysteresis

In addition to eddy current loss, a time-varying excitation causes losses due to the hysteresis of ferromagnetic materials. During a magnetization cycle of the material, the flux follows a field variation on a hysteresis loop. The hysteresis is the reason why the relation between B and H field is not a single valued curve [9, 26]. The energy required for dislocation of the Bloch walls and orientation of the magnetic dipoles during a magnetization process is to some extent dissipated in the form of heat in the magnetic material [61]. Hence there is a net energy input into the magnetic material during each cycle of the hysteresis loop.

Laminated Core

The area enclosed by the hysteresis loop shown in Figure 3.2 for one particular cycle is equivalent to the energy density

$$w_m = \oint_t \boldsymbol{H} \, \mathrm{d}\boldsymbol{B}. \tag{3.28}$$

Since the area in Figure 3.2 represents the loss energy density per cycle, hysteresis loss at a given flux level is proportional to the magnetization change frequency and the total volume of the magnetic material. Calculation of power loss by integration over the considered volume V leads to the final expression

$$P_h = K_h f B^h V. \tag{3.29}$$

Here P_h denotes the hysteresis loss, K_h the material-specific hysteresis loss constant and h the loss exponent with $1.5 < h < 2.5$, typ. $h = 2.0$. Hence hysteresis losses are approximately proportional to the square of flux density in the magnetic circuit but increase only linear with magnetization frequency [9].
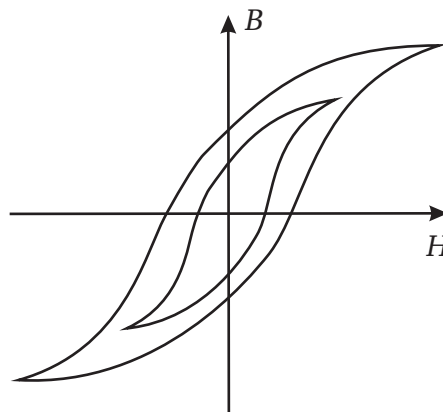

Figure 3.2.: *B-H* hysteresis loops for two different peak AC current values.

Solid Core

In [91] an approximation for the hysteresis losses in a solid cylindrical core is given as

$$P_h \approx \frac{\pi f \sin\gamma B_{avg}^2}{\mu} \cdot \sqrt{1 + \frac{f}{2(1 + \sin\gamma)f_{sc}}}. \tag{3.30}$$

Including several simplifications, the model is straightforward and requires only easily accessible material parameters. It is useful when designing a solid magnetic core or assessing the hysteresis influence on existing actuators. For higher frequencies the eddy current loss dominates and the hysteresis loss is usually neglected.

3.3.4. Coil Windings

Besides the losses in the core of reluctance actuators, there is an additional undesired source of loss in the windings that are used for the excitation of the machine. The associated power is called winding loss or copper loss, where the latter term refers to the material often used in coil design. Basically, winding loss results from Joule heating and is produced by the electrical currents in the winding of the actuator. The power loss P_w is obtained by modifying JOULE's first law

$$P_w = i^2 R, \tag{3.31}$$

where i denotes the current flowing in the winding and R the electrical resistance of the coil material. The power P_w is dissipated in form of heat in the winding. From a technical point of view the design needs to avoid heat and be thermally safe. However, in some cases an adequate cooling is required additionally. The electrical loss in the windings is proportional to the winding resistance and square of the winding current. Hence it is also called I^2R loss. Since the resistive loss scales with the square of current, it will dominate the total actuator loss for slow armature movements and high forces.

Basically two strategies can be applied to decrease winding losses. The first would be to use a lower winding current. However, this would have a significant impact on the available magnetic force which increases with the square of i. The second approach consists in using a lower winding resistance, achieved by a large cross-sectional area of the wire and the use of low-resistivity conductors. A detailed discussion of this issue with a focus on the practical application in actuator design is given in Section 4.8.

3.4. Modeling Methods

MAXWELL's equations are fundamental for the calculation of magnetic fields. However, their analytical solution is not feasible for the majority of technically relevant magnetic circuits. This section reviews magnetic networks, FE analyses and a reduced order approach with respect to the design of reluctance shakers.

3.4.1. Reluctance Circuits

The spatially distributed field in magnetic actuators can be described using magnetic equivalent circuits (MEC). This modeling method exploits the analogy of magnetic and electric field [47]. In order to map the physical magnetic circuit, a magnetic equivalent network is set up using lumped parameters, see Figure 3.3. The total volume subjected to the magnetic flux is separated into flux tubes, which are characterized by a perpendicular flux transit at the front and end surfaces. Each flux tube j is modeled at circuit level by a magnetic reluctance R_{mj} which causes the magnetic voltage drop V_{mj}. Similar to OHM's law, HOPKIN's law

$$R_{mj} = \frac{V_{mj}}{\Phi_j} \tag{3.32}$$

expresses the relation between magnetic resistance, magnetic potential and magnetic flow. In terms of geometrical and material parameters the equation above is rewritten as

$$R_{mj} = \frac{l_j}{\mu_j A_j}. \tag{3.33}$$

For a single flux tube j of length l_j, the magnetic permeability μ_j and the respective cross-sectional area A_j of the physical magnetic circuit are assumed to be constant. The MMF created by the coil is written as

$$\Theta = w \cdot i \tag{3.34}$$

where $w \cdot i$ is the total number of ampere turns exciting the magnetic circuit. The relation can be also interpreted as a magnetic voltage applied to the equivalent circuit. Both KIRCHHOFF's voltage law (KVL) and KIRCHHOFF's current law (KCL)
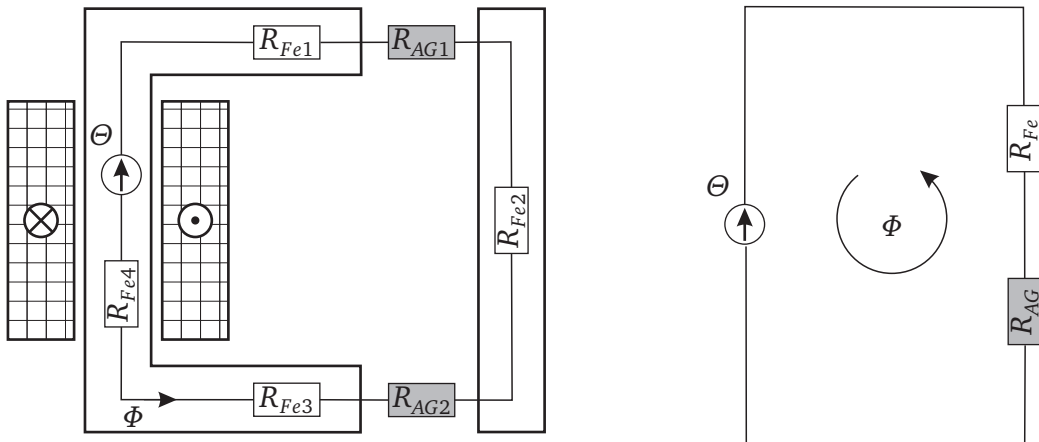
$$\sum_j V_{mj} = \Theta \tag{3.35}$$

Figure 3.3.: Basic magnetic actuator and equivalent magnetic circuit.

$$\sum_{k} \Phi_k = 0 \tag{3.36}$$

can be transferred to the magnetic case. An overview of the relation between electric and magnetic circuits with the most relevant parameters is given in Table 3.1.

An equivalent circuit for a permanent magnet consists of a magnetic voltage source modeling the MMF Θ_{PM} and the associated reluctance R_{PM}. Both are a function of the material and geometrical parameters of the permanent magnet.

$$\Theta_{PM} = H_{cB} \cdot l_{PM} \tag{3.37}$$

$$R_{PM} = \frac{H_{cB} \cdot l_{PM}}{B_r \cdot A_{PM}} = \frac{l_{PM}}{\mu_{PM} \cdot A_{PM}} \tag{3.38}$$

Here H_{cB} denotes the coercivity, B_r the remanence and μ_{PM} the magnetic permeability. The length is given by l_{PM} and the cross-sectional area by A_{PM}. The typical modeling procedure is characterized by the following steps:

1. Separation of the magnetic circuit into flux tubes with homogeneous field and constant cross-sectional area.

2. Determination of the equivalent circuit.

3. Application of the circuit laws KCL and KVL.

4. Determination of the resulting equation system.

5. Calculation of the fluxes.

6. Calculation of flux-dependent parameters such as inductivity and force.

The main drawback of MEC is the mandatory knowledge of the main flux paths which are not always known in detail [9]. Hence the modeling relies on engineering experience and intuition [26]. Most real world devices have complicated designs with multiple flux paths that have to be modeled with serial and parallel reluctances. The complex determination of fringing flux makes the calculation of fringing factors difficult [15, 24]. The same applies to the implementation of saturation by nonlinear *B-H* curves. Furthermore the consideration of core losses requires a workaround.

However, lumped parameter models with their low discretization result in a small set of equations which can be solved analytically. The implementation in a system simulator is straightforward with low computational cost. This allows for fast parameter studies. Therefore, magnetic networks are useful as a first step in the design process for the dimensioning of the magnetic circuit [34, 118].

Table 3.1.: Comparison between electric and magnetic circuit theory [9, 47, 92].

quantity	electric equivalent	unit	magnetic equivalent	unit
flow	current i	A	flux Φ	Vs
potential	voltage drop u	V	MMF V_m	A
potential/flow	resistance R	Ω	reluctance R	A/Vs
conductivity	conductivity σ	S/m	permeability μ	Vs/Am

3.4.2. Finite Element Analysis

To avoid the limitations of magnetic equivalent circuits, the finite element method (FEM) proves to be an important alternative. It is the most general and accurate method for the calculation of magnetic fields in technical devices [9]. The basic principle consists in the subdivision of the investigated problem region into small subdomains, called finite elements, which are connected via nodes to a grid. For the subproblems simple ansatz functions based on the vector potential are chosen. The global solution results from the superposition of all functions. Together with the boundary conditions of the problem an equation system is formulated and solved for the unknown magnetic potentials in each element. For spatially large problems and a high discretization, very large equation systems result, which are solved numerically.

BRAUER [9] delivers a reasonable short sketch of the FEM concept for the solution of linear magnetostatic problems. Point of departure is the assumption of energy conservation

$$W_{in} = W_{stored} \tag{3.39}$$

with W_{in} as input energy and W_{stored} as stored energy. That way the analyzed region exhibits no power loss. In reluctance actuators the energy is fed via the coils featuring the current density $\boldsymbol{J}$, and is stored in the magnetic field. Integration over the considered volume yields the energy balance

$$\frac{1}{2} \int \boldsymbol{J} \cdot \boldsymbol{A} \, \mathrm{d}v = \int \frac{B^2}{2\mu} \, \mathrm{d}v \tag{3.40}$$

with a constant μ. Now an energy functional is defined, in this case the difference between stored and input energy, which yields

$$F = W_{stored} - W_{in} = \int \frac{B^2}{2\mu} \, \mathrm{d}v - \frac{1}{2} \int \boldsymbol{J} \cdot \boldsymbol{A} \, \mathrm{d}v. \tag{3.41}$$

According to the energy conservation law, the functional must be zero. However, the condition is somewhat reduced and replaced by the minimization

$$\frac{\partial F}{\partial A} = 0. \tag{3.42}$$

Inserting (3.41) and rearranging yields

$$\frac{\partial}{\partial A} \int \frac{B^2}{2\mu} \, \mathrm{d}v = \int J \, \mathrm{d}v. \tag{3.43}$$

Now the problem region is discretized and a shape function based on the magnetic vector potential is set up for each element. Here the equivalence between flux density and the curl of the magnetic vector potential A

$$\boldsymbol{B} = \nabla \times \boldsymbol{A} \tag{3.44}$$

is used. Finally (3.43) is rewritten as an equation system

$$\boldsymbol{K} \cdot \boldsymbol{A} = \boldsymbol{J} \tag{3.45}$$

which represents the discretized problem. Here $\boldsymbol{K}$ denotes the stiffness matrix, $\boldsymbol{A}$ the unknown vector potentials and $\boldsymbol{J}$ the known input current densities. In general, $\boldsymbol{K}$ is a $n \times n$ matrix with number of nodes n. A high problem discretization results in a large number of nodes and the solution of the resulting equation system requires considerable computation time.

Due to the relevance of the FE method for the design of magnetic devices, a large number of software packages is commercially available. The finite element analysis (FEA) is a three step procedure [47]. The first step is the preparation of the problem for the solution (preprocessing). During this phase a high level of engineering knowledge is required. The problem can be simplified by omitting nonrelevant details. Exploitation of geometrical symmetries further helps to reduce simulation time. The preprocessing phase is organized as follows [9]:

1. Geometry: specification of the magnetic circuit's shape and dimensions.

2. Discretization: subdivision into finite elements.

3. Materials: specification of material parameters, in particular *B-H* curves for nonlinear magnetic materials.

4. Excitations: specification of input current sources or densities.

5. Boundary conditions: determination of flux conditions at the boundaries of the model.

After the model preparation, the equation system is set up and consequently solved in the second step. In the final analysis step the desired quantities such as flux distribution, force and inductivity are calculated (postprocessing).

In summary, the FEM allows for the consideration of complex actuator geometries and phenomena such as fringing flux and nonlinear material [60]. In transient simulations eddy current influence and even the mechanical armature motion caused by electromagnetic forces can be investigated. However, the analysis requires a very high computational effort. Therefore, transient FE models are not suitable for fast system simulation and control design.

3.4.3. Reduced Order Model

As discussed above, the main advantage of the MEC based approach is the compact analytical model, which allows for a fast system simulation and control design. For a detailed analysis of the magnetic circuit, a FE model is indispensable. Reduced Order Modeling (ROM) combines the advantages of numerical computations with an analytical model. The resulting mathematical description is suitable for implementation in a system simulator and allows for dynamic simulations. Furthermore, it can serve as a basis for control design. In the following a short outline of the modeling procedure is given. The application to magnetic reluctance actuators is described in Chapter 5.

The method is based on the energy conservation principle and uses energy functions as a physical principle for the system description. For the mathematical description of electromagnetic energy conversion devices, the co-energy is particularly suitable since relevant system parameters such as force and inductance can be derived from it. Furthermore, the co-energy values for the actuator can be calculated using standard FE software without major effort.

In a first step the discrete co-energy values for all relevant operating points are calculated during the FE system analysis. Then an analytical expression is determined by curve fitting. The relevant system parameters are obtained by derivation. The actual order reduction results from the analytical approximation and leads to a significantly reduced simulation time. The reduced model can be used for both transient system simulation and control design.

3.4.4. Comparison

During the work on this thesis all three described modeling methods were used. This section discusses relevant properties for the design of reluctance actuators. Among these are the suitability of the model for control design, the mapping of complex geometries and the consideration of complex effects such as saturation or fringing flux. In addition the computation speed and feasibility of transient simulations are compared. Table 3.2 gives an overview of the methods used for the actuator design. According to their suitability for different tasks, the methods are used in different design phases.

A simple and straightforward MEC model of the actuator is set up in the first design phase for the dimensioning of the magnetic circuit and a fast estimate of the static and dynamic properties. Furthermore, it enables parameter studies and facilitates the understanding of the influence of important design parameters. Section 4.7 gives a detailed description of the MEC used for the magnetic circuit design.

For the analysis of the magnetic circuit draft and a detailed design analysis FE methods are applied. They allow for a comprehensive consideration of all relevant effects. Using static FEM, the main performance maps for the characterization of the actuator are calculated by a variation of armature position and coil currents. For validation of the numerical computation the results from the circuit method are used. Additionally the co-energy values for the reduced order model are computed simultaneously. Thus the FE model is a keystone of the design process. Section 4.9 discusses the set up in detail.

Table 3.2.: Modeling methods for magnetic reluctance actuators, based on [92].

method	geometry mapping	nonlinear material	transient simulation	numerical cost	used for
MEC	limited	complex	feasible	low	dimensioning
static FEM	flexible	feasible	not feasible	high	design analysis
trans. FEM	flexible	feasible	feasible	very high	–
ROM	flexible	feasible	feasible	low	dynamic simulation

Transient FE models are not used due to computing time reasons. For dynamic simulations a reduced order model (ROM) is set up, which captures the distinct nonlinear characteristics of reluctance actuators. In Chapter 5 the method is applied to the developed actuators, while the simulation is validated by measurement results in Chapter 7.

3.5. Chapter Summary

This chapter has reviewed basic aspects of electromagnetic reluctance actuators and has given an overview of the magnetic force generation and the dynamics of magnetic circuits.

Power losses have a significant influence on the operating performance. For this reason, methods for the assessment of the main loss mechanisms – due to eddy currents, hysteresis and winding resistance – have been discussed. Eddy currents reduce the obtainable force in high dynamic actuators and the associated power loss increases with the square of the magnetization frequency. Therefore, the reduction of eddy current influence is important for the design of an improved reluctance actuator in Chapter 4.

For a systematic design, accurate models are indispensable. Here, network based models are compared to the numerical field calculation and a reduced order approach. For the actuator development in this thesis, linear reluctance circuits are used for calculation of the main actuator parameters during the first design phase, since the low computational cost facilitates parameter studies. Finite element methods serve as analysis tool for the magnetic circuit enabling a detailed evaluation of the flux density distribution and an accurate computation of the generated magnetic force. For dynamic simulations, a reduced order approach based on numerical co-energy calculations is applied. It preserves the main advantages of the FE model, particularly the accurate prediction of the nonlinear actuator characteristics, but enables fast system simulations.

4. Magnetic Design

This chapter aims at the magnetic design of enhanced reluctance actuators for vibration excitation. The magnetic part is complemented by the mechanical design and by the required information processing presented in Chapter 6, forming a mechatronic actuator system. The interaction of the individual design domains enables the realization of ambitious design objectives such as high force, high bandwidth and a stable operating behavior.

The design considerations are based on the results of previous actuator projects [33, 78] and influenced by the development of an industrial car test rig with four reluctance actuators [53] parallel to this thesis. The feedback from the practical application is incorporated into the proposed design methodology, which leads to enhanced reluctance shakers for the controlled excitation of vehicles and vehicle components.

Section 4.1 gives an overview of the design process for magnetic reluctance shakers. Point of departure for the development are the demands on actuators in NVH test rigs as discussed in Section 4.2. Based on given reference trajectories, an estimation of the required force and stroke is carried out. Section 4.3 deals with the selection of actuator topologies. Different configurations for polarized magnetic circuits are reviewed and a concept for an enhanced reluctance shaker is proposed. The magnetic circuit design is illustrated in Section 4.4 – 4.9. It covers the material selection, the magnetic circuit dimensioning and the design analysis. The reduction of eddy current influences by appropriate design measures is a major focus of the investigation.

4.1. Design Process

The overall design of reluctance actuators is a complex iterative process. The design of the magnetic subsystem is particularly challenging since many parameters such as material properties, airgap lengths, reluctance areas and coil data have to be considered. Therefore, it is difficult to formulate a closed-form expression for the design process. However, in order to achieve a systematic approach the following substeps are adapted from [47]:

1. specification of design objectives

2. topology selection

3. material selection

4. magnetic circuit dimensioning

5. coil design

6. magnetic design analysis: static and dynamic.

The structure of this chapter follows the proposed design steps. In the first phase the design objectives for the actuator are determined. These arise mainly from the respective application. In this thesis, reluctance actuators with a linear armature movement for the direct vibration excitation of specimen are considered. The main design objectives are a high force, stroke and dynamics as well as a low temperature rise and manufacturing costs. Further aspects are discussed in Section 4.2.

There are numerous possibilities for the basic actuator topology, which are only limited by the design objectives. The selection of an appropriate topology depends mainly on the planned motion pattern. Furthermore, the positioning of the permanent magnets influences the topology. Altogether, the design objectives and position of permanent magnets substantially constrict the amount of reasonable solutions. In addition, for the positioning of permanent magnets the mechanical and magnetic material properties have to be considered. After the selection process only a few basic topologies remain which have to be investigated in detail.

Once the topology is determined, the fundamental dimensioning of the magnetic circuit is carried out using a basic MEC model. The calculation considers only the reluctances of the working airgaps and permanent magnets. In addition, a simple leakage flux formulation is used and linear material properties assumed. The low computational cost of MECs allows for a fast investigation of several alternative topologies. If the main dimensions are known, further important parameters such as force and inductivity can be calculated. This enables the assessment of the static and dynamic actuator properties.

If the basic magnetic circuit meets the design requirements, the winding data is calculated based on the necessary MMF. The required actuator dynamics, the temperature rise and cooling system, as well as the actuator geometry influence the coil design. The temperature rise has to be considered during the design phase to ensure the stability of the permanent magnet bias against demagnetization. Furthermore, the characteristic magnetic values deteriorate with rising temperature. While the thermal management depends mainly on the designated coil area, the physical dimensions of the coil have a great influence on the overall actuator size and weight. Therefore, the final magnetic circuit dimensioning and coil design are closely related and often require an additional iteration loop. The design of the magnetic circuit and the windings is treated in Sections 4.7 and 4.8. The thermal evaluation is done by an estimation of the temperature rise using basic design guidelines.

Upon completion of the analytical magnetic circuit design, detailed magnetic field calculations are carried out. Here the characteristic maps of the actuator are calculated. In contrast to the simple MEC model, nonlinear material properties and leakage flux can be easily incorporated, so that the computation results are more accurate. In addition, the co-energy values are computed in the same process. The FEM analysis allows also for the visualization of flux lines, which is useful for the optimization of magnetic circuit details. If the analysis reveals that important design parameters have to be changed, the impact of a parameter variation on the calculation of coil and circuit values must be investigated.

A dynamic simulation is the final step in the magnetic circuit design. In this thesis an energy-based approach is chosen which combines the accuracy of the FE method with low computational cost. It captures the strongly nonlinear characteristics very

well and allows for a detailed prediction of the actuator dynamics, cf. Chapter 5.

Provided that the magnetic circuit design fulfills the established design objectives, the mechanical design process starts. The physical dimensions of the magnetic circuit influence the mechanical design and vice versa, hence mechanical design considerations might require a modification of the magnetic circuit design.

The flowchart in Figure 4.1 gives an overview of the design procedure for the magnetic circuit. Design algorithms for electromagnets with a special focus on polarized permanent magnets are presented in [89].

4.2. Design Objectives

The actuators designed in this thesis are intended for the use in vibration test rigs for cars and components. The objective is to simulate a real road drive on a simulator with four electromagnetic reluctance actuators, see Chapter 2. Hence the actuator must provide the excitation energy required for the accurate replication of squeak and rattle events in the road simulator. The foundation for the actuator specification is built by excitation profiles used in the vibration test rigs. Usually, the profiles are based on either synthetic or measured acceleration data. The demands on the actuator are derived using these files, considering the load influences caused by the cars or components under test. The main aspects are the required force, stroke and actuator dynamics.

Test Profiles

For NVH testing several well-established excitation profiles exist, which can be divided into two major signal groups [53]:

1. periodic signals
   - sinus (fixed frequency)
   - sinus (variable frequency)
   - square wave
   - sawtooth wave

2. noise signals
   - artificial noise signal
   - measured road signals.

For NVH testing usually rather low frequencies are used. At BMW Group a frequency range of 5 Hz to 60 Hz is considered to be sufficient for the assessment of most unwanted noises. The lower frequency limit is mainly determined by the maximum actuator stroke, which applies particularly to electrodynamic and electromagnetic reluctance shakers. The excitation of the car body with frequencies above 60 Hz contributes only insignificantly to the overall noise signal.

The most commonly used signals are nonperiodic road profiles, also called *rough road tracks*. These are e.g. cobble stone tracks, highway tracks with characteristic
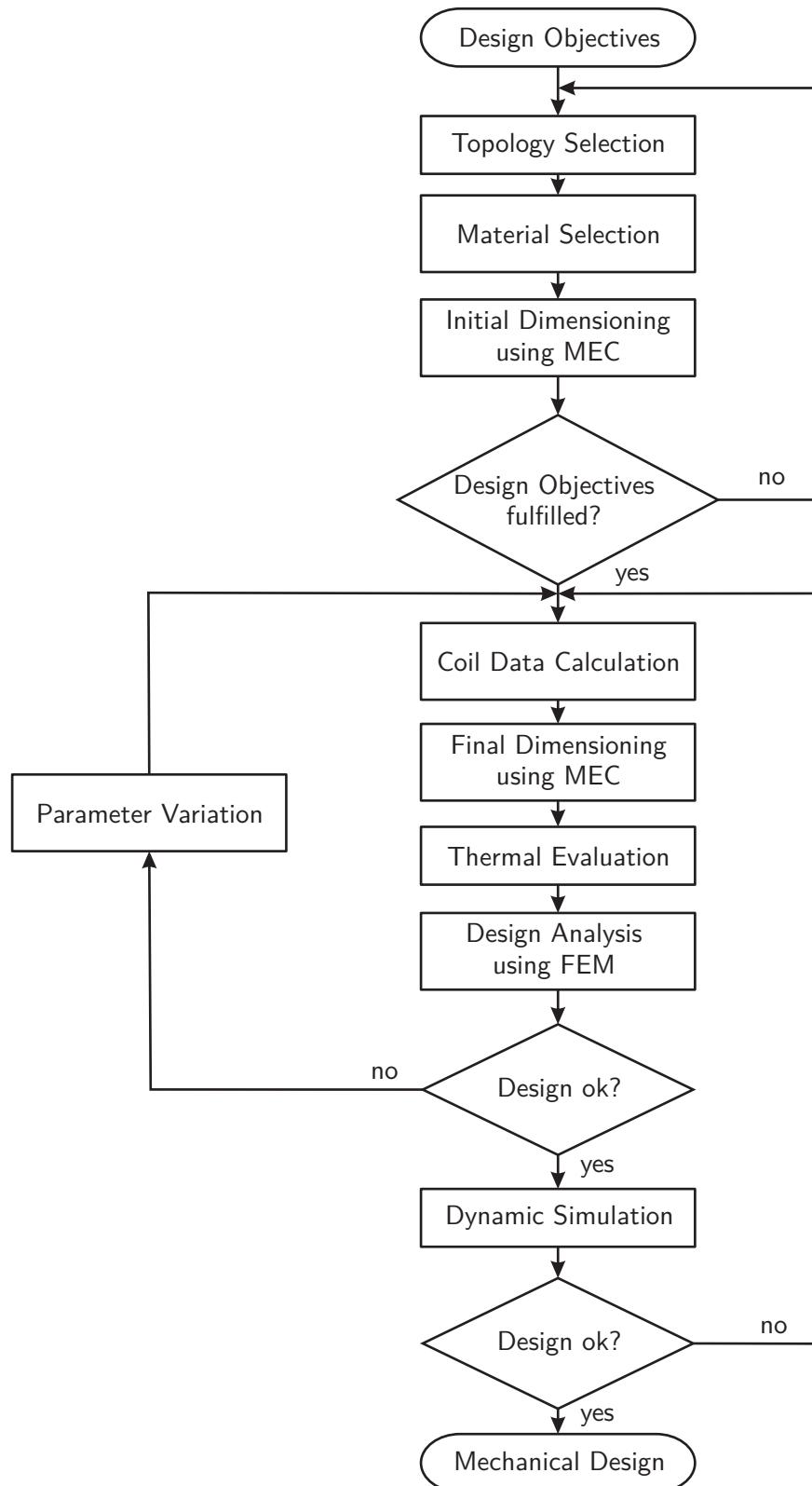
Figure 4.1.: Design algorithm for the magnetic circuit, adapted from [89].

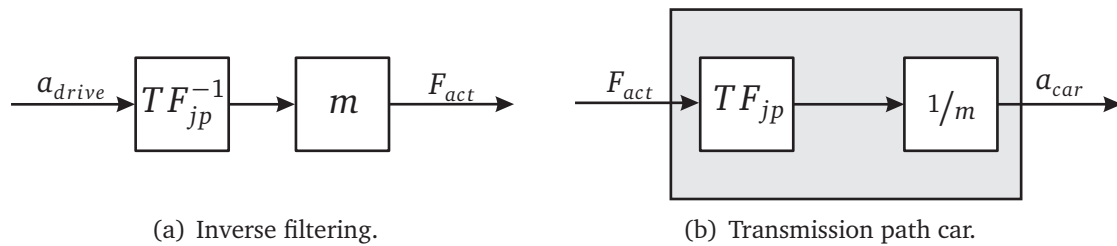(a) Inverse filtering.   (b) Transmission path car.

Figure 4.2.: Estimation of the required actuator force.

transverse joints and railroad crossing tracks. Compared to periodic signals with a sequential excitation of the various resonance frequencies, the unwanted noise is tested simultaneously over a broader frequency spectrum. MOOSMAYR compares the suitability of different signal types for noise and vibration testing. In [74] worst-case profiles are defined, which enable vehicle and road independent noise testings. For that purpose the profiles are generated from various measurements at the brake calipers and different points of the car body. The envelope of all measured data is the highest possible acceleration profile. In addition, the vehicles and the test tracks are varied. Consequently, the influence of different car types and roads is incorporated in the worst-case profile. The resulting four different characteristic road profiles map the relevant testing scenarios at BMW GROUP with increasing excitation energy.

The correct application of these testing profiles depends on the test rig in use. Hydraulic hydropulsers excite the vehicle under test via the chassis in a realistic way. Hence the induced acceleration is damped on the transmission path from the hydraulic post to the car body. Since the damping is chassis-specific, the resulting car body excitation varies for different chassis and cars. However, the test rig with reluctance actuators (see Chapter 2.3) excites the vehicle via the jacking points in an unrealistic way. Compared to the excitation via tires and chassis, particularly the damping of the jacking point has to be considered. In order to obtain excitation profiles with sufficient amplitudes, the original drive files are filtered with the inverse transfer function of the jacking point as shown in Figure 4.2(a).

Following this approach, an estimation of the required armature acceleration of the actuator can be calculated. In order to obtain the required actuator forces from the filtered acceleration data, two additional characteristics of the test rig have to be taken into account. First, the car test rig uses two or four magnetic reluctance actuators, such that actuated mass per actuator is equivalent to the half or respectively quarter of the total car mass. Second, a part of the actuated weight is supported by the ground. Thus the real equivalent weight is even lower and can be estimated as approximately $m = 180\,\text{kg}$ for a heavy luxury class vehicle (BMW 7 series) in a test rig with four actuators. Figure 4.2(b) shows the simplified block diagram for the transmission path from the actuator to an acceleration measuring point in the car.

Experiments

In addition to the calculations based on given acceleration profiles, the actuator specification is validated experimentally [119]. The measurements are carried out on the test rig developed in [53] using the proprietary drive file *KSF50* and a heavy luxury
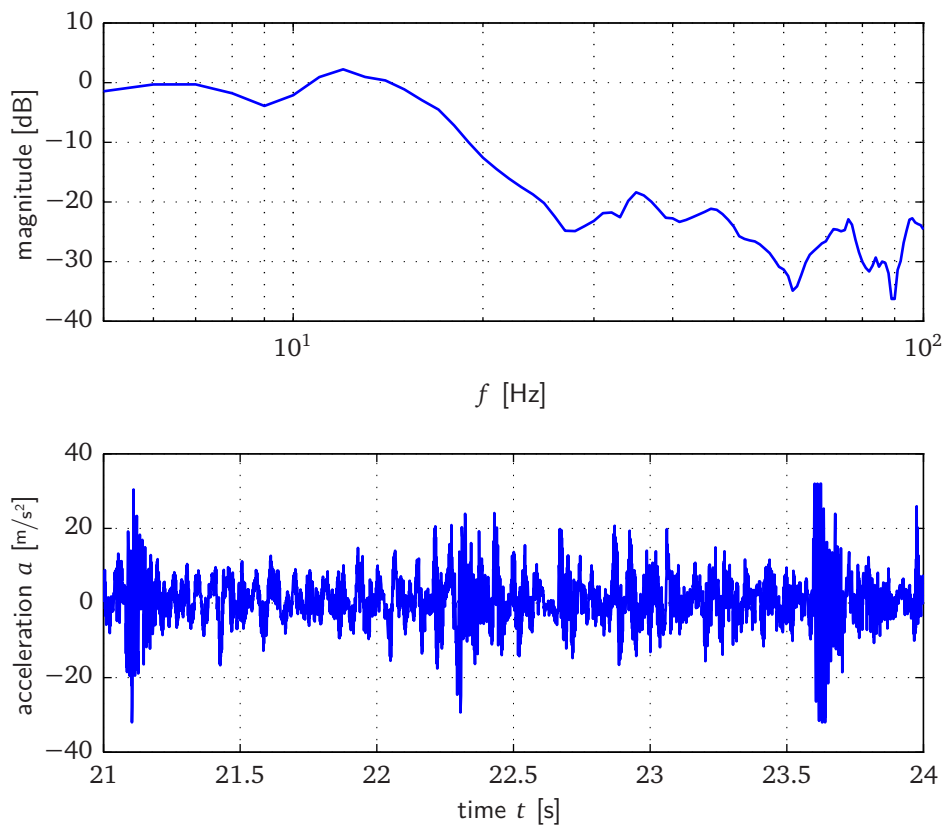
Figure 4.3.: Measured jacking point transfer function (top) and filtered acceleration profile (bottom).

car (BMW 7 series). This acceleration profile features the second-highest excitation energy of all analysis profiles used at BMW. At the time of experimental investigation, this was the most intense profile the test rig could replicate due to its prototype status. Figure 4.3 illustrates the measured transfer function of the jacking point and the already filtered acceleration profiles used for the excitation during the experiment. For the transfer function measurement the shaker armature is chosen as first sensor position. The second sensor is placed at the car underbody next to the jacking point with a distance of 100 mm. The system shows a typical resonance frequency at around 14 Hz and strong damping for higher frequencies. Consequently, the input acceleration profile for the excitation of the test rig shown in Figure 4.3 is more intense than the original drive file. In particular, signal parts with frequencies above the resonance frequency of 14 Hz are amplified in order to compensate the jacking point damping.

Moreover, the relevant actuator parameters are recorded. Figure 4.4 shows the measured actuator force and armature displacement during the experiment. A force of 5 kN and stroke of $\pm$ 2 mm are sufficient for a realistic road simulation with the profile in use. According to the power spectral density of the actuator force, most energy is required in the lower frequency range between 5 - 80 Hz which corresponds to the power density distribution of the acceleration profile. Due to stroke limitations the actuator is not capable of replicating the comparatively high displacements at very low
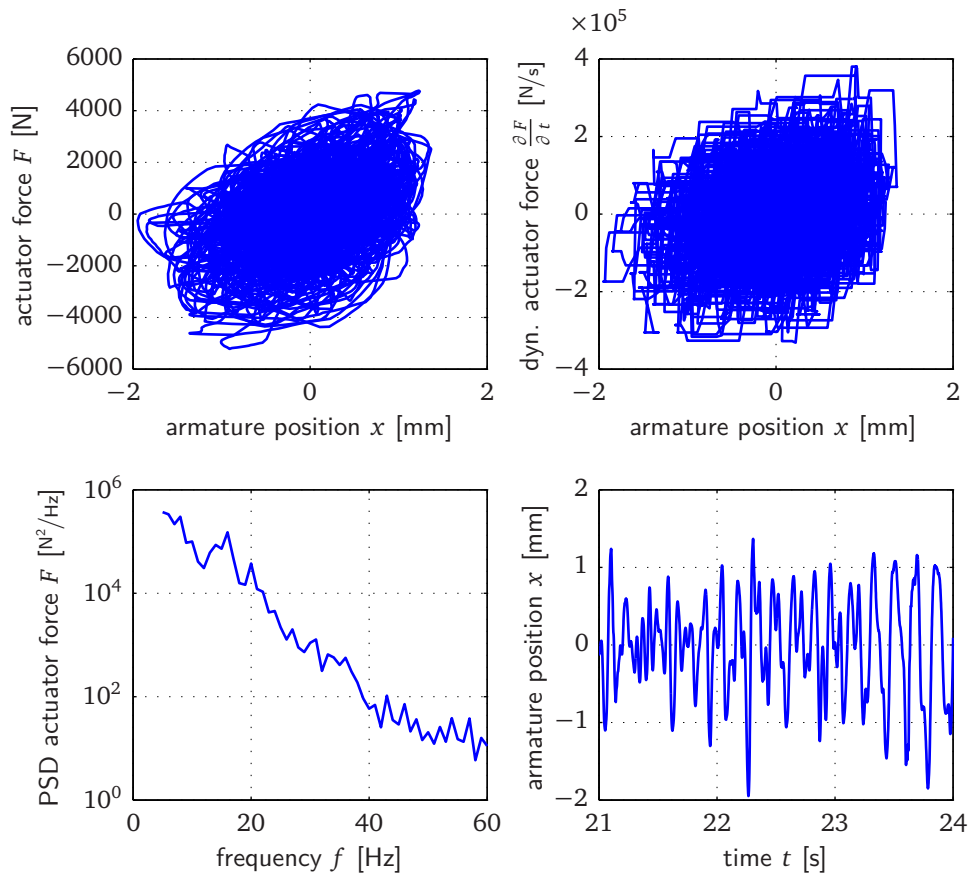
Figure 4.4.: Measured actuator force and stroke.

frequencies. Thus frequencies below 5 Hz are filtered out in the command signal [53].

Actuator Specification

Based on the calculations and experiments described above, the specification for a new actuator model is set up. Compared to the previously built prototypes [33], the following design objectives are formulated:

- increased force and stroke

- stable operating behavior without feedback control

- increased bandwidth of the magnetic subsystem by reducing eddy current influence

- cost reduction and simplified manufacturing.

The maximum actuator force is set to 8 kN resulting in a safety factor of 1.6 with respect to the minimum required force of 5 kN. The increased actuator force allows for the excitation of heavier vehicles and accounts for the additional weight of staff and test equipment on board of the vehicle. The maximum stroke is ±3.5 mm. This enables a displacement of 3 mm in each direction during experiments and leaves an additional

Table 4.1.: Design objectives for a reluctance actuator for automotive NVH testing.

design objective	value	description
force	$\pm 8\,\text{kN}$	maximum force
stroke	$7\,\text{mm}$	peak-peak
frequency range	$0\ldots 100\,\text{Hz}$	standard NVH testing
noise emission	minimal	noise sensitive testing situations
cooling system	passive	avoidance of additional noise emissions
installation space	minimal	small test rigs
robustness	maximal	industrial application
cost-effectiveness	high	industrial acceptance

safety airgap of 0.5 mm. Since typical drive files require the highest displacements at very low frequencies (0...5 Hz), the increased maximum stroke extends the frequency range which can be replicated. A stable behavior facilitates the application in test rigs and increases the robustness during the excitation of different test objects. Reducing eddy current influence in the magnetic circuit contributes to a higher bandwidth of the actuator. The overall operating range of the actuator is 0...100 Hz which covers the requirements of NVH testing. A cost-effective design is particularly advantageous for the application in car test rigs where four actuators are used.

Additional design objectives arise from the demands of typical NVH testing situations. The installation space should be minimized in order to enable the design of small test rigs. Auxiliary cooling systems are avoided due to the potential noise emission and required space. In order to prevent overheating, this requires a thermally safe design of the actuator. Here, a trade-off between the conflicting requirements of small size and low temperature rise must be found. Design measures for good trajectory tracking are compulsory for a realistic road simulation. In particular, the precise replication of oscillations with small amplitude must be ensured. Table 4.1 summarizes the actuator specification.

4.3. Topology

The topology selection is influenced by the design objectives described above. Main aspects are a bidirectional force generation, small actuator size, low heat generation and high robustness.

The key features of any topology to be evaluated are a permanent-magnetic bias, the superposition of coil MMF and permanent magnet MMF and the use of springs which provide the restoring force for the armature and fully compensate the negative magnetic stiffness caused by the permanent magnets. The positive influence of armature springs in terms of stabilization and dynamics is also investigated by Lequesne [67,68]. The use of permanent magnets enables a size reduction and better efficiency due to lower winding losses [8]. In addition, the working point on the reluctance force - magnetic flux density parabola is shifted from the origin to a higher base flux level [97], cf. (3.14). Consequently the current-force factor and force density increase.

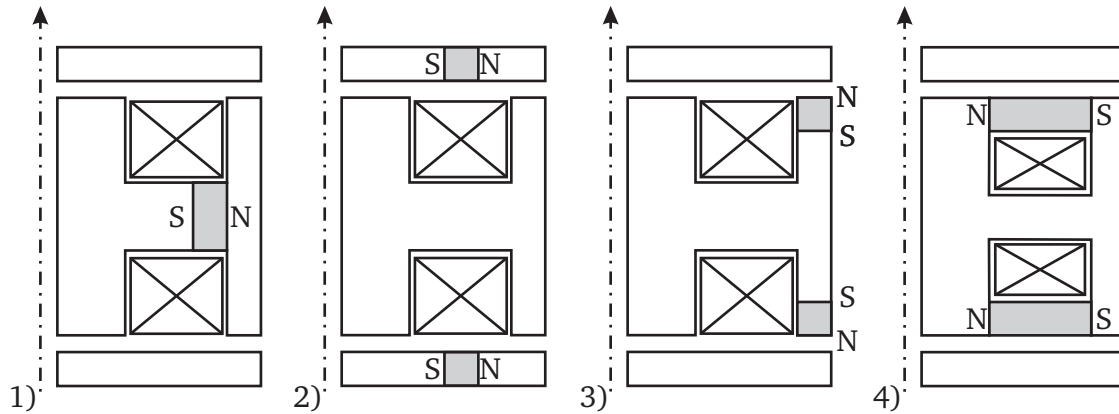The basic concept with two moving armature discs and a fixed core as already

Figure 4.5.: Polarized magnetic circuits (1-3 serial, 4 parallel).

proposed by OBERBECK [78] will be followed here, since it represents a powerful combination of two individual solenoids in a compact design. It combines high robustness even for laminated armatures with a simple assembly.

This section is divided into two parts. The first part discusses and compares several polarized topologies with respect to the application in reluctance shakers. The second part proposes a configuration for the new reluctance actuator HPS3 (high power shaker 3).

4.3.1. Polarized Magnetic Circuits

Polarized magnetic circuits can be configured in various ways, mainly because of the positioning options for the permanent magnets. A detailed study on the influence of the permanent magnet position is carried out in [89]. Figure 4.5 gives an overview of different serial and parallel polarized configurations. Based on the positive experiences with previously designed magnetic circuits [33, 78], the evaluation concentrates on modifications of the existing serial polarized topologies.

Topology 1 uses a central PM assembly position between the coils. Due to the serial configuration, the coil flux passes through the permanent magnet with its high reluctance. However, if both coils create the same MMF, the working point of the magnet remains essentially constant during a coil MMF variation, thereby preventing demagnetization effectively. From a mechanical perspective the setup is more complex since at least two core parts are required. During operation, the flux of force passes the magnets. Permanent magnets are brittle and usually bonded into the core, so that the fatigue strength of the assembly is a critical point. If the permanent magnet material is already magnetized during the assembly, the joining is challenging due to the occurring magnetic forces.

The magnetic circuit of topology 2 uses a magnet position in the armature. However, the armature of the shaker is subject to extreme shocks during operation, particularly in the event of faults. Sintered permanent magnets are brittle and shock-sensitive. The consequences are potential demagnetizations or material failures up to armature fracture. In addition, the design is complex with respect to both manufacturing and assembly [78].

In topology 3 the permanent magnets are placed on the core surface. Here, core and armature discs are made of single solid parts, thus avoiding mechanical problems during assembly and operation. Since the magnets sit directly at the airgap, a potential contact between armature and magnet is possible, requiring additional measures for the mechanical protection of the magnets. The magnets are subject to the full coil excited flux. Therefore, the working point is sliding on the characteristical demagnetization curve. A careful selection of permanent magnetic material is necessary in order to avoid irreversible demagnetization.

An alternative to the discussed serial polarized topologies is the parallel configuration of topology 4. This configuration maintains the minimum core dimensions of the serial polarized variants. Core and armature are single solid parts. However, coil width and permanent magnet length are coupled. From a magnetic perspective, the main drawback is the significant flux portion circulating in the magnetic shortcut instead of passing the working airgaps.

For the topology of the reluctance actuator HPS3 the configuration with surface magnets has been chosen which allows for a maximum rigidity and strength of the iron core and armature since both consist of only one part respectively.

4.3.2. Actuator Concept

Figure 4.6 illustrates the concept for the reluctance actuator HPS3. The magnetic circuit is composed of a fixed core and a moving armature. The armature consists of two discs connected by the actuator shaft. The system exhibits a vertical and horizontal symmetry, with the flux paths forming a parallel circuit with a common central flux path. In each branch the flux passes the airgap twice, so that a reluctance force according to (3.15) is generated at the inner and outer iron surfaces. Both coils and permanent magnets are used as magnetomotive force sources. For the magnetic bias surface-mounted permanent magnets are used which are magnetized in axial
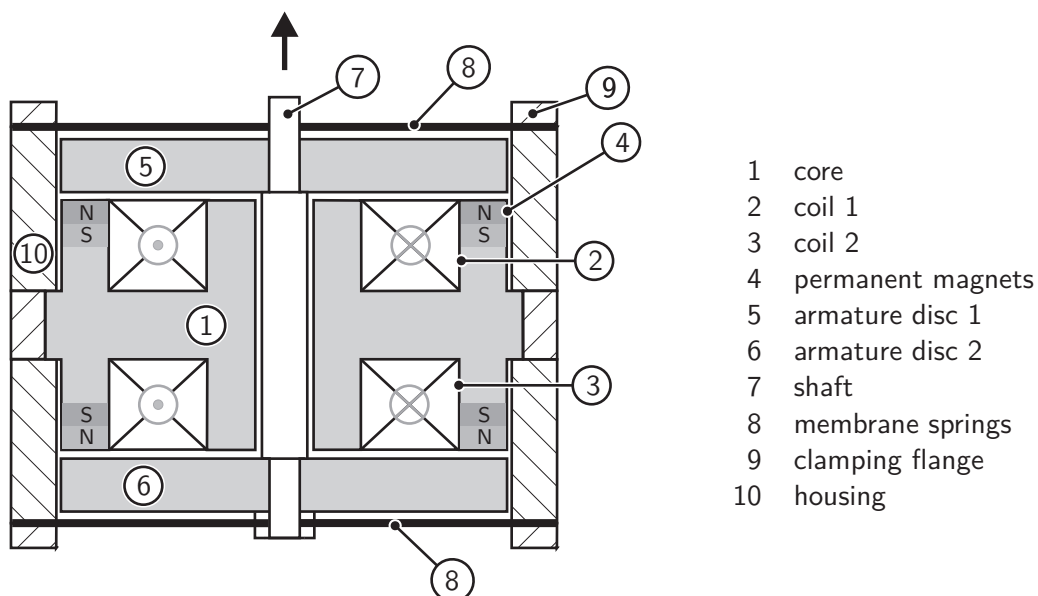

1	core
2	coil 1
3	coil 2
4	permanent magnets
5	armature disc 1
6	armature disc 2
7	shaft
8	membrane springs
9	clamping flange
10	housing

Figure 4.6.: Schematic view of the HPS3 actuator.

direction. Two coils allow for the control of the total magnetomotive force. The coils are separately driven and carry current in the same direction. Actuation is achieved by superposition of coil MMF and permanent magnet MMF. If the current is directed into the page in the right half-plane of the magnetic circuit and out of the page in the left half-plane, armature disc 2 is subject to more flux than armature disc 1 and consequently the armature moves upwards due to the reluctance forces at its surface. A current reversal results in a downward movement; at zero current and equal airgaps the forces are balanced so that the overall force is zero. Hence the setup allows for the required bidirectional force generation and linear motion. The detailed magnetic circuit design is described in Section 4.7.

Strong springs provide the restoring force for the armature and compensate the negative magnetic stiffness caused by the permanent magnetic bias. This way a stable operation without feedback control is achieved. Here, membrane springs combine the guidance of the shaft with the suspension. A comparison with other spring-guidance designs shows clear functional advantages such as low friction, stick-slip avoidance, small required space and customizable spring characteristics. These properties are particularly beneficial for the present application with respect to the high frequency operation at small stroke ranges as discussed in Section 6.2.4.

4.4. Magnetic Material Selection

The application of appropriate magnetic materials is essential in order to ensure a high performance of the magnetic circuit. The selection of magnetic materials involves both magnetically soft and hard substances. Soft magnetic materials are mainly used for the flux guiding in the magnetic circuit. In contrast, magnetically hard materials are used for the realization of the permanent magnetic bias and allow for a steady MMF without stationary coil currents. This section discusses properties of different materials and suitable selection criteria.

4.4.1. Soft Magnetic Materials

Important demands on soft magnetic materials with respect to actuator design are first of all magnetic characteristics (B-H curve), thermal and temporal stability but also mechanical characteristics, workability and other aspects such as price and availability [72]. Magnetic properties have a significant influence on the actuator performance: a high saturation induction allows for a compact actuator design, while a low coercivity and slim hysteresis loop diminish the magnetic loss. On the other hand, for high dynamic performance a low electrical conductivity and a small dynamic widening of the hysteresis loop are required. Soft magnetic materials consist mainly of iron, cobalt, nickel and their alloys [7]. For high performance actuators the alloys are more relevant.

CoFe alloys reach the highest saturation polarizations of up to 2.4 T. The coercivity ranges from 0.4 . . . 1.4 A/cm. Vacuumschmelze GmbH develops the Vacoflux series with various Co shares for high performance motors and solenoids with highest traction forces [112]. However, a higher Co share also raises the alloy cost.

Table 4.2.: Comparison of soft magnetic materials for reluctance actuators [108, 112]. Static values for solid material, dynamic values for sheets.

alloy		NiFe	CoFe	SiFe	
composition	%	45 - 50	17 - 50	3	
trade name		Permenorm	Vacoflux	Trafoperm	M250-35A
saturation level	T	1.55	2.35	2.03	1.90
coercivity	A/m	5	140	20	22
max. permeability		120000	9000	30000	-
dynamic 50 Hz		90000	12000	13000	8000
loss at 50 Hz, 1 T	W/kg	0.25	64 (2.0 T, 400 Hz)	1.0	0.95
sheet thickness	mm	0.2	0.35	0.3	0.35

SiFe is widely used in electrical machine design. The addition of silicium increases the specific electric resistance and helps to reduce the eddy current loss. Yet, with an increasing Si share the saturation polarization declines. For common alloys, the saturation polarization levels at approximately 2 T [72]. In most machine designs the alloy is used in form of sheets which are stacked to a lamination package.

NiFe shows clearly lower saturation polarizations which reach 1.6 T depending on the Ni share. VACUUMSCHMELZE GMBH offers alloys with 45-50% Ni under the trade name PERMENORM. Compared to pure iron, the specific electric resistance is about four times higher. The alloy features moreover small magnetic losses and high permeability values, which make it a good choice for dynamic actuators. It is used for the solid magnetic core of the HPS1 actuator [33].

Table 4.2 summarizes the magnetic characteristics of several materials for reluctance actuators. For high dynamic actuators, the material selection is closely related to the necessary eddy current reduction strategy, see Section 4.5. If no laminations are used, only a high specific electric resistance countervails eddy currents. For the shaker design in this thesis a SiFe alloy is chosen. The non grain-oriented electrical steel grade M250-35A is recommended for highly energy efficient applications in special purpose motors [108]. Figure 4.7 illustrates selected material characteristics. Due to the comparably low magnetic loss for electrical steels it is well suited for the high dynamic actuator operation with its frequent magnetization reversals. In Figure 4.8 the magnetization curves and dynamic losses of the materials described above are compared. Overall, M250-35A offers a good combination of saturation flux density, magnetic loss, price and availability.

4.4.2. Hard Magnetic Materials

Relevant magnetic properties of permanent magnets for the design of high performance actuators are high remanence, coercivity and good temperature stability. High remanence and coercivity yield a maximum energy density of the permanent magnet and allow for a compact actuator design. High coercivities and good temperature stabilities prevent permanent magnet demagnetization because of two reasons.

First, during operation the permanent magnets of polarized reluctance actuators are subject to opposing magnetic fields which weaken the permanent magnets' field.
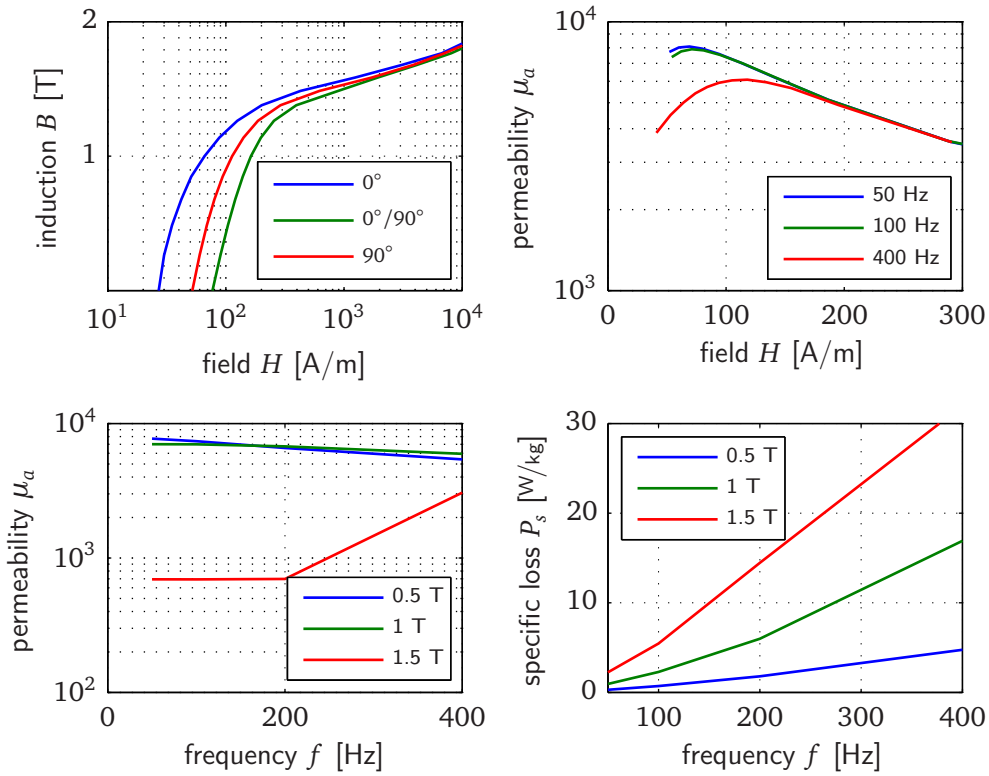
Figure 4.7.: Material properties of electrical steel M250-35A dependent on angle to rolling direction, frequency and peak induction [108].

top left: magnetization curve at 50 Hz   *top right:* amplitude permeability
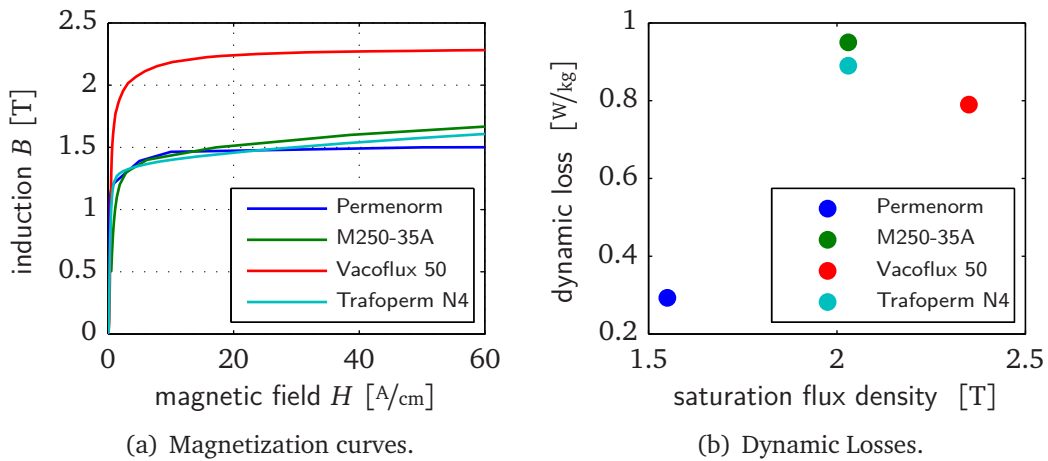*bottom left:* dynamic amplitude permeability   *bottom right:* specific total loss

(a) Magnetization curves.   (b) Dynamic Losses.

Figure 4.8.: Soft-magnetic material properties [108, 112]. Dynamic losses for $B = 1\,\mathrm{T}$, $f = 50\,\mathrm{Hz}$, material thickness $d = 0.35\,\mathrm{mm}$.
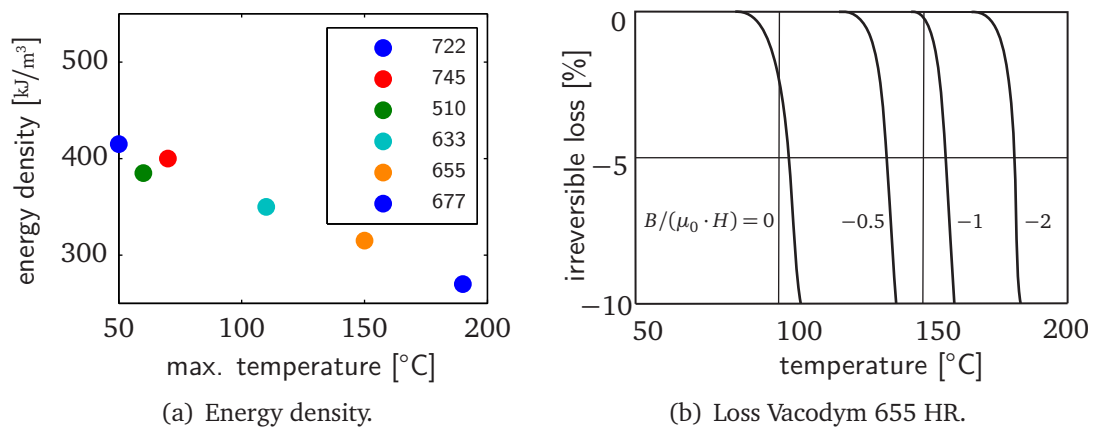
(a) Energy density.

(b) Loss Vacodym 655 HR.

Figure 4.9.: Vacodym HR magnets: energy density and maximum continuous operating
temperatures (left), typical irreversible losses for different operating points and temperatures (right) [113].

The second cause of demagnetization is the temperature rise due to winding losses
and external temperature influences. In the case of actuators for vibration testing, the
application in climatic chambers adds to the total thermal load. The specification of
permanent magnet materials is temperature-dependent. For increasing temperatures
the demagnetization curve is shifted towards lower flux densities. However, to prevent
irreversible damage the magnet's operating point must remain on the linear part of
the demagnetization curve above the knee.

Furthermore, nonmagnetic properties are relevant for the actuator design. The
sintered permanent magnet material is brittle. As a consequence, direct impact loads
on the magnet must be avoided by appropriate design measures, cf. Section 6.2. For
the application in a rough industrial testing environment, the influence of air moisture
and aggressive media must be taken into account. The chemical stability depends
mainly on the used alloy. However, for extreme environmental conditions additional
coatings are available to prevent corrosion.

Magnetically hard materials are mainly based on the ferromagnetic metals iron,
nickel and cobalt as well as rare-earth metals [72]. The most important material
compositions are aluminum-nickel-cobalt (AlNiCo) alloys and rare-earth alloys, which
can be subdivided into neodymium-iron-boron (NdFeB) alloys and samarium-cobalt
(SmCo) alloys. In the following, NdFeB permanent magnets are investigated since they
feature the highest energy densities currently available. The BH_{max} product is about
ten times higher compared to AlNiCo magnets, which leads to a considerable reduction
of the required magnetic volume. VACUUMSCHMELZE GMBH sells NdFeB magnets under
the trade name VACODYM. Figure 4.9(a) compares different magnet types of the HR
(high remanence) series.

The magnet type VACODYM 655 HR is chosen, which shows excellent magnetic
properties due to its strong magnetic matrix phase Nd_2Fe_14B featuring very high
saturation and high magnetic anisotropy [113].

The 655 HR type is isostatically pressed and offers a good tradeoff between energy
density and tolerable operating temperature. The demagnetization curves shown
in Figure 4.10 exhibit a linear characteristic in a large field range and illustrate the
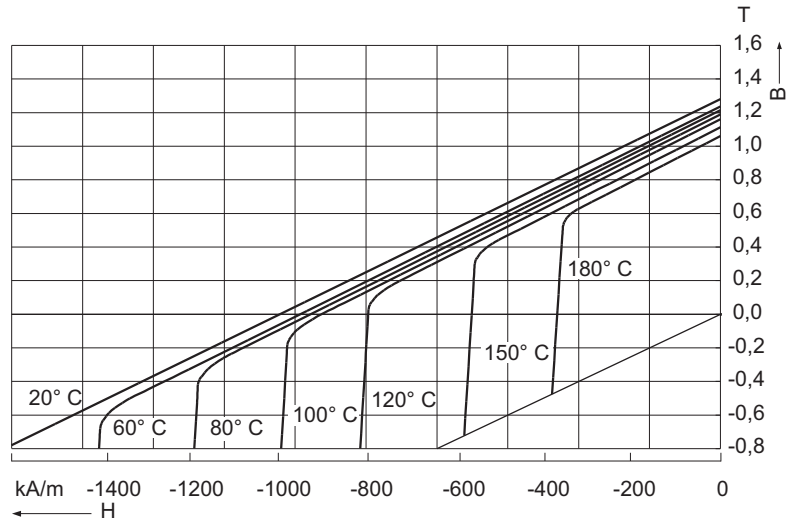
Figure 4.10.: Typical demagnetization curves of Vacodym 655 HR at different temperatures, adapted from [113].

resistance against permanent demagnetization. For normal operating temperatures the material permits a near complete demagnetization without irreversible loss. The correlation between irreversible loss for different temperatures and operating points is additionally illustrated in Figure 4.9(b). Table 4.3 summarizes the magnetic properties of the selected permanent magnet material.

Table 4.3.: NdFeB permanent magnet Vacodym 655 HR [113].

property	symbol	unit	typical	guaranteed
remanence	B_r	T	1.28	1.22
coercivity	H_{cB}	kA/m	990	925
	H_{cJ}	kA/m		1670
energy density	$(BH)_{max}$	kJ/m^3	315	280
relative permeability	μ_r		1.029	1.050
max. operating temperature	T_{max}	°C	150	

4.5. Eddy Current Reduction Strategies

During high dynamic operation the magnetic system is subject to fast changing fields. The time change in magnetic field strength is caused by the changing coil currents but also by the generated armature motion. Since the soft magnetic material used for the flux guidance in core and armature is electrically conducting, eddy currents occur (see Section 3.3.1). The consequences are a delayed force generation, higher losses and a frequency dependent transfer function of the magnetic circuit, which results from the damping and phase delay. Consequently, eddy currents limit the bandwidth of the reluctance actuator and deteriorate the performance of the controlled test rig.

In order to obtain a high bandwidth, methods for eddy current reduction have to be chosen in the design phase. Figure 4.11 shows a top view of sample magnetic
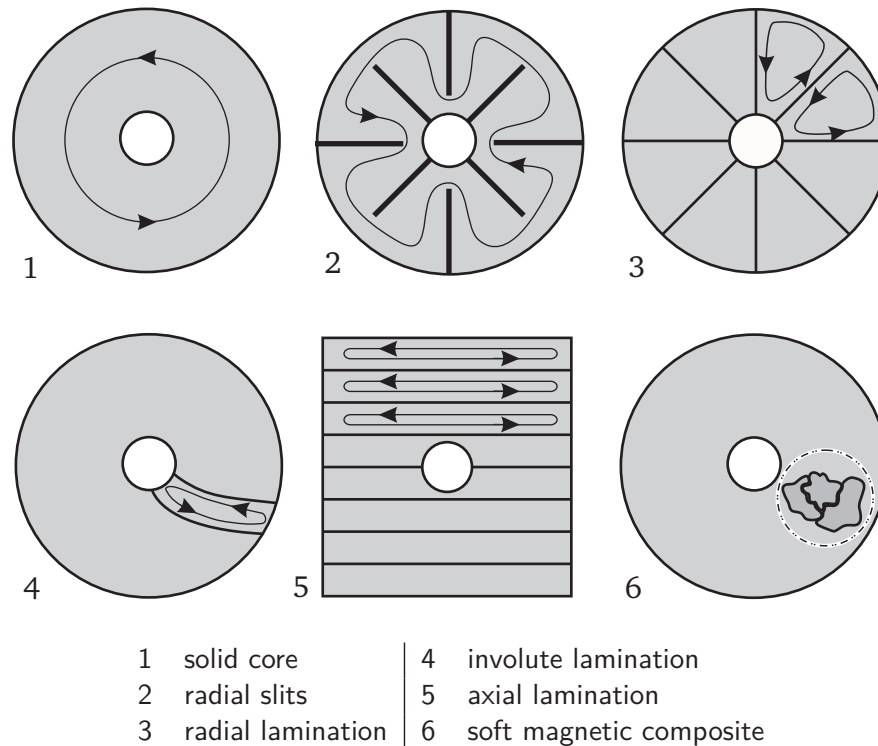
1	solid core	4	involute lamination
2	radial slits	5	axial lamination
3	radial lamination	6	soft magnetic composite

Figure 4.11.: Eddy current reduction strategies: top view on different magnetic cores with exemplary eddy current patterns. The time-varying magnetic field is directed out of the page.

cores with indicated eddy current flow patterns. The different reduction strategies can be classified into material based and laminated approaches. The measures are closely related to the selected soft magnetic material and actuator topology. Important design factors are efficiency for eddy current reduction, flux guidance restrictions, design complexity, resulting construction form, manufacturing complexity and the associated costs. In addition the design must withstand the high mechanical loads during vibration excitation.

From a mechanical design perspective solid cores (1) are advantageous since even complex shapes can be manufactured. Furthermore, the magnetic flux can be guided in all three dimensions. The coils can be embedded in a cylindrical core and coil ends are avoided which facilitates a small design. However, since there are no geometrical measures for eddy current reduction, materials with higher resistance have to be used, which implies lower saturation flux densities. For higher frequencies material based methods are not sufficient, so that eddy current losses and the associated drawbacks become dominant.

An alternative to solid cores is the insertion of slits in core and armature parts (2). These block the eddy current flow pattern and act like laminations [9, 90]. Slits can be incorporated into the established design concept. Yet, the cutting is expensive to manufacture and the eddy current reduction is comparatively low. Further restrictions are the decreased strength of the cut parts and limitations for the flux guidance.

The radial lamination (3) combines the concept of constructive measures for eddy current reduction with the cylindrical shape of solid cores. It is highly efficient in eddy

Table 4.4.: Evaluation of eddy current reduction strategies.

design concept	eddy current reduction	design complexity	material cost	design shape
solid core (1)	$--$	$++$	$--$	cylinder
radial slits (2)	$+$	$-$	$-$	cylinder
radial lamination (3)	$++$	$--$	$++$	cylinder
involute lamination (4)	$++$	$-$	$++$	cylinder
axial lamination (5)	$++$	$+$	$++$	cuboid
SMC (6)	$++$	$+$	$--$	cylinder

$++$ excellent, $+$ good, $-$ weak, $--$ poor

current reduction and enables compact designs. Flux guidance is basically restricted to two dimensions in order to avoid flux crossing between the single sheets, which would result in high losses. The main drawback is the complex manufacturing of the single sheets which have a variable thickness.

The involute lamination (4) avoids the complex shape of the single sheets and enables the use of sheets with a constant thickness [111]. The curvature is small enough to avoid flux crossing between the sheets and thus prevents high losses. While the concept maintains the favorable cylindrical shape with its maximum design space utilization, it requires the precise bending of the individual sheets.

The axial lamination (5) uses regular sheets with a constant thickness and no further processing. Flux guidance is restricted to the sheet planes which results in a cuboid shape of core and armature. The coil ends protrude over the core, thereby increasing the construction size. The main advantage is the simple design and the broad availability of standard sheets from different manufacturers.

An alternative located between solid cores and laminated cores are soft magnetic composites (SMCs, (6)). The material consists of metallic powder with a particle diameter ranging from 50-250 μm. Every individual particle is coated with an electrical insulation layer of approximately 30 nm [83]. Eddy currents are effectively restricted by the insulation, so that the material is suitable for use in alternating magnetic fields [95]. For frequencies above 300 Hz, eddy current loss is lower than in laminated cores. Furthermore, 3D flux guidance is feasible due to the isotropic magnetic properties. The solid material can be processed into complex shapes. However, the magnetic properties are inferior to those of electrical sheets. The permeability of the particle insulation is approximately the same as air. Therefore, SMCs reach a relative permeability of 500 - 1000, which is only about 10 - 20 % of electrical steels. The saturation flux density is lower as well.

Table 4.4 gives an overview of the eddy current reduction strategies discussed above. For the magnetic core of the HPS3 actuator an axial lamination is chosen. The concept can be easily integrated into the selected topology and electrical steel sheets in standard form are available from different manufacturers, which adds to the cost effectiveness.

4.6. Laminations

After choosing a lamination form, the sheet thickness is determined using the skin depth defined in (3.27). Lamination thickness should be approximately $0.5 - 1$ skin depth [9]. For the calculation a working point at $100\,\text{Hz}$ is assumed. With the material properties $\mu_r = 8000$ and $\sigma = 2.08 \cdot 10^6\,\text{S/m}$, an estimation of the required sheet thickness yields 0.2 - 0.4 mm. Consequently the standard thickness 0.35 mm is chosen. In general, a lower lamination thickness decreases the stacking factor, such that a trade-off has to be found between eddy current reduction and the resulting net volume of the magnetic material. Due to the actuator topology, the flux is guided in the sheet along the direction of grain and transverse to it. The non grain-oriented standard electrical steel M250-35A features isotropic properties and low losses.

Besides magnetic design issues, the manufacturing of the stack is important for the performance. The lamination stacks are subject to strong vibration and high forces during operation. Fabrication tolerances directly influence important actuator dimensions such as the airgap length. The application in an automotive test rig implies harsh industrial conditions, which requires mechanically robust laminations. The main manufacturing aspects are the fabrication of the lamination form and the packeting of the single sheets to a stack.

The single sheets for the prototype are laser cut due to cost and time constraints. Available manufacturing technologies for the stacks of armature and core include welding, riveting, stapling, interlocking and bonding. Here, bonding with the varnish technology has been chosen. The sheets are coated on both sides with a bonding varnish, the coating thickness being approximately $5\,\mu\text{m}$. The advantages in contrast to other manufacturing technologies are maximum stiffness and stability of the lamination stack. In addition, very high precision can be realized. The varnish seals and prevents moisture ingress between the individual sheets. Furthermore, an additional insulation of the individual sheets can be achieved [66]. Overall, the stack is very compact and vibration-resistant.

During the manufacturing process the individual coated sheets are first stacked and aligned. The assembly is then heated and pressed. The actual bonding is achieved by the temperature-triggered softening and the curing process during the cooling down phase.

4.7. Magnetic Circuit Dimensioning

The dimensioning of the magnetic system includes the calculation of the main static parameters such as the required reluctance area and the excitation by the coils and permanent magnets. Following hereon, the main dimensions of the magnetic system are determined. All calculations are based on a magnetic equivalent circuit.

4.7.1. Magnetic Equivalent Circuit

Based on the selected actuator topology (No. 3 in Figure 4.5), an equivalent network is set up. The characteristic equations allow for calculation of the main actuator
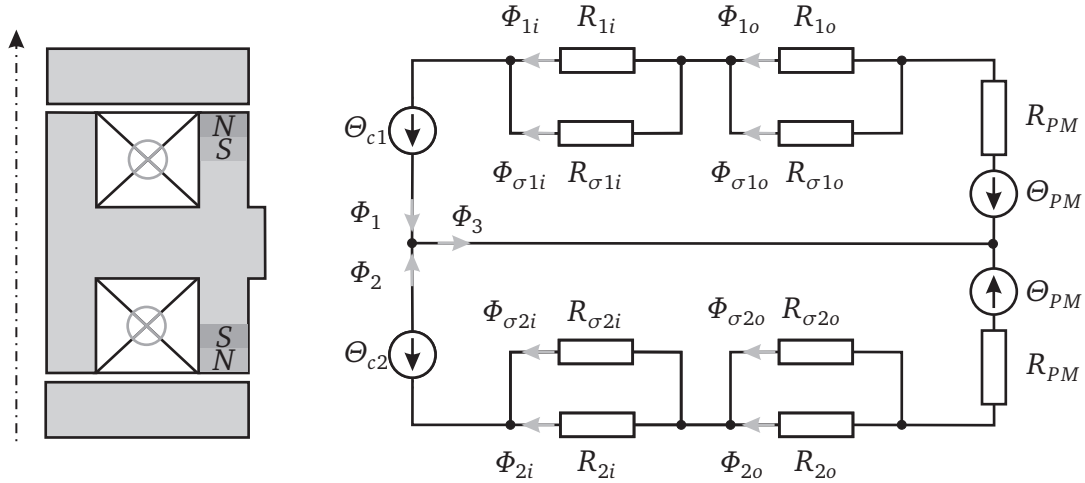
Figure 4.12.: Schematic view of the magnetic system and equivalent circuit.

parameters. In order to keep the design process straightforward, the model captures only the most important effects.

Figure 4.12 shows the magnetic equivalent circuit of the HPS3 magnetic system. The MMF of the coils and permanent magnets is represented by magnetic voltage sources. For this purpose the top and bottom coil are modeled by one excitation Θ_1, Θ_2 respectively. Similarly, each magnet row is modeled by a voltage source Θ_{PM} and the associated reluctance R_{PM} of the magnet. In addition, the circuit accounts for the working airgaps at the top and bottom with main R_{jk} and leakage $R_{\sigma jk}$ reluctances.

For the first design step only the leakage at the working airgaps is included while minor leakage flux paths across the coil windows are neglected. The magnetic voltage drop in the core material is not incorporated due to its high permeability. The main flux passes each working airgap twice, which is mapped in the MEC by four main reluctances connected in parallel to the respective leakage reluctances. Leakage is incorporated using a leakage factor σ_k

$$0 < \sigma_k < 1 \qquad \text{with} \qquad k = \{i, o\} \tag{4.1}$$

which is defined by the ratio of leakage flux and total flux in each branch. The main reluctances of the working airgaps R_{jk} and the permanent magnets R_{PM} are defined by their material and geometrical parameters

$$R_{jk} = \frac{x_{jk}}{\mu_0 A_k} \qquad \text{with} \qquad j = \{1, 2\},\ k = \{i, o\} \tag{4.2}$$

$$R_{PM} = \frac{h_{PM}}{\mu_{PM} A_{PM}}. \tag{4.3}$$

Here x_{jk} denotes the length of airgap j and A_k the associated reluctance area. Accordingly, the reluctance of the permanent magnet is characterized by its height h_{PM}, permeability μ_{PM} and flux normal area A_{PM}. The ratio between working flux Φ_{jk} and

total flux Φ_j in each branch

$$\Phi_{jk} = \frac{R_{\sigma jk}}{R_{jk} + R_{\sigma jk}} \Phi_j \overset{!}{=} (1 - \sigma_k)\Phi_j \tag{4.4}$$

is defined by the associated reluctance ratio on the one hand and equivalently by the leakage factor on the other hand. Here $R_{\sigma jk}$ denotes the leakage reluctance which is given as a function of the airgap reluctance by:

$$R_{\sigma jk} = \left(\frac{1}{\sigma_k} - 1\right) \cdot R_{jk}. \tag{4.5}$$

The total MMF results from the superposition of coil MMF and permanent magnet MMF and is combined to

$$\Theta_1 = \Theta_{PM} - \Theta_{c1} \tag{4.6}$$
$$\Theta_2 = \Theta_{PM} + \Theta_{c2}. \tag{4.7}$$

Finally, the network equation system can be written in matrix-vector form with the excitation vector $\boldsymbol{\Theta}$, the flux vector $\boldsymbol{\Phi}$ and the reluctance matrix $\boldsymbol{R}$:

$$\boldsymbol{\Theta} = \boldsymbol{R} \cdot \boldsymbol{\Phi} \tag{4.8}$$

$$\boldsymbol{\Theta} = \left(\begin{array}{ccccccccccc} \Theta_1 & \Theta_2 & 0 & 0 & 0 & 0 & 0 & 0 & 0 & 0 & 0 \end{array}\right)^T \tag{4.9}$$

$$\boldsymbol{\Phi} = \left(\begin{array}{ccccccccccc} \Phi_1 & \Phi_2 & \Phi_3 & \Phi_{1i} & \Phi_{\sigma 1i} & \Phi_{1o} & \Phi_{\sigma 1o} & \Phi_{2i} & \Phi_{\sigma 2i} & \Phi_{2o} & \Phi_{\sigma 2o} \end{array}\right)^T \tag{4.10}$$

$$\boldsymbol{R} = \left(\begin{array}{ccccccccccc}
R_{PM} & 0 & 0 & R_{1i} & 0 & R_{1o} & 0 & 0 & 0 & 0 & 0 \\
0 & R_{PM} & 0 & 0 & 0 & 0 & 0 & R_{2i} & 0 & R_{2o} & 0 \\
0 & 0 & 0 & R_{1i} & -R_{\sigma 1i} & 0 & 0 & 0 & 0 & 0 & 0 \\
0 & 0 & 0 & 0 & 0 & R_{1o} & -R_{\sigma 1o} & 0 & 0 & 0 & 0 \\
0 & 0 & 0 & 0 & 0 & 0 & 0 & R_{2i} & -R_{\sigma 2i} & 0 & 0 \\
0 & 0 & 0 & 0 & 0 & 0 & 0 & 0 & 0 & R_{2o} & -R_{\sigma 2o} \\
1 & 1 & -1 & 0 & 0 & 0 & 0 & 0 & 0 & 0 & 0 \\
-1 & 0 & 0 & 1 & 1 & 0 & 0 & 0 & 0 & 0 & 0 \\
-1 & 0 & 0 & 0 & 0 & 1 & 1 & 0 & 0 & 0 & 0 \\
0 & -1 & 0 & 0 & 0 & 0 & 0 & 1 & 1 & 0 & 0 \\
0 & -1 & 0 & 0 & 0 & 0 & 0 & 0 & 0 & 1 & 1
\end{array}\right) \tag{4.11}$$

The equation system is used for two purposes. Given a known reluctance matrix $\boldsymbol{R}$, in the first design phase the required excitations through coils and permanent magnets can be calculated by defining a desired flux vector $\boldsymbol{\Phi}$. This approach is used for the dimensioning of the magnetic circuit in the next section. Once the excitation vector $\boldsymbol{\Theta}$ is determined and the geometry of the magnetic circuit is calculated, the system can be solved for unknown fluxes. Consequently, other parameters such as force and inductance can be calculated.

4.7.2. Static Parameters

In this section the required reluctance area, the MMF of the coils and permanent magnets and the static force are calculated using the equivalent circuit in Figure 4.12 and its describing equations. Point of origin is the desired static force as determined in Section 4.2; the main design parameters are listed in Table B.4.

In the following, the approach proposed by HERRMANN is adapted [33]. The magnetic circuit is considered linear and the design is subject to the following constraints [118]:

1. The desired maximum static force $F_{s,max}$ is defined by the design objectives.

2. The armature is in neutral position $x = 0$, i.e. the length of equivalent working airgaps is equal $x_{1k} = x_{2k}$.

3. Both coils contribute the same MMF $\Theta_{c1} = \Theta_{c2} = \Theta$.

4. The permanent magnet MMF generates half of the desired flux density $B_{max}/2$ at zero coil MMF.

5. Coil field and permanent magnetic field are superimposed. For a maximum coil MMF Θ_{max} the bottom flux path is subject to the maximum desired flux density B_{max}, while the top flux path is flux-free. In that case the maximum positive magnetic force $F_{s,max}$ is generated. If the coil MMF is reversed, the force direction is so as well.

6. The leakage factor is considered to be uniformly $\sigma_k = \sigma = 0.15$, which corresponds to 15 % leakage flux. The lamination stacking factor is assumed to be $k_{st} = 0.15$.

7. The relevant reluctance surfaces are equal for all airgaps $A_k = A_0$.

Reluctance Area

Basis for the calculation of the required reluctance surface is the reluctance force defined in (3.14). In the HPS3 topology the main flux crosses each airgap twice. Apart from the desired actuation force $F_{s,max}$, the required surface

$$A_0 \geq \frac{1}{2k_{st}} \frac{2\mu_0 F_{s,max}}{((1-\sigma)B_{max})^2} \tag{4.12}$$

depends mainly on the permitted maximum flux density $B_{max} = 1.4\,\text{T}$ in the soft magnetic part of the circuit which is made from M250-35A. Consequently, materials with a high B_{max} enable a significant reduction of the overall actuator size. The applied approach for the surface calculation implies an unlimited reluctance area for leakages $\sigma \rightarrow 1$. However, a realistic design aims at leakage minimization $\sigma \rightarrow 0$, which yields reasonable actuator parameters in practice.

Coil MMF

Due to the given design constraints, half of the permitted magnetic flux in each iron branch is generated by the maximum current in the coils. If the MMF of the permanent magnets is set to zero, the specific flux follows from the permitted flux density and reluctance surface. Using the KVL in the top or bottom branch, the required maximum coil MMF is obtained.

$$\Phi_j\big|_{\Theta_{PM}=0} = \frac{B_{max}}{2}A_0 \tag{4.13}$$

$$|\Theta_{c,max}|\big|_{\Theta_{PM}=0} = \Phi_j R_{PM} + \Phi_{ji}R_{ji} + \Phi_{jo}R_{jo} \tag{4.14}$$

Permanent Magnet MMF

The same approach is used for the calculation of the required permanent magnet excitation. If the MMF of the coils is set to zero, the desired flux results from the permitted flux density and reluctance surface. Applying the KVL in the top or bottom branch yields the required permanent magnet MMF:

$$\Phi_j\big|_{\Theta=0} = \frac{B_{max}}{2}A_0 \tag{4.15}$$

$$|\Theta_{PM}|\big|_{\Theta=0} = \Phi_j R_{PM} + \Phi_{ji}R_{ji} + \Phi_{jo}R_{jo}. \tag{4.16}$$

The MMF of a permanent magnet row is given by its material-dependent coercivity $H_{cB} = 925\,\text{kA/m}$ (Vacodym 655 HR, see Table 4.3) and the height in direction of magnetization h_{PM}. The height is chosen such that the required Θ_{PM} is obtained

$$\Theta_{PM} = H_{cB} \cdot h_{PM} \tag{4.17}$$

$$h_{PM} = \frac{1}{H_{cB} - \frac{\Phi_j}{\mu_{PM}\mu_0 A_{PM}}} \cdot \left(\Phi_{ji}R_{ji} + \Phi_{jo}R_{jo}\right). \tag{4.18}$$

Due to the design, the magnet area is determined by the required reluctance area $A_{PM} = A_0$. Up to this point, the design is characterized by the desired flux values which are used for the calculation of the excitations required therefor.

In addition, the equation system (4.8) for the description of the MEC contains the reluctance matrix R and the excitation vector Θ. The reluctance matrix is parameterized by the chosen leakage factor and airgap length as well as the reluctance area calculated in (4.12). Once the excitations calculated in (4.13)-(4.18) are known, the system can be solved for unknown fluxes.

Magnetic Force

In the final step the total magnetic force is calculated by inserting the working flux in each airgap in the basic equation for the reluctance force (3.14). The flux passes the inner and outer reluctance surface in each airgap. Thus both Φ_{ji} and Φ_{jo} contribute to the force generation. The total force is a result of the superposition of the reluctance

force at the top and bottom airgap

$$F_m = F_{m2} - F_{m1} = \frac{\Phi_{2i}^2 + \Phi_{2o}^2}{2\mu_0 A_0} - \frac{\Phi_{1i}^2 + \Phi_{1o}^2}{2\mu_0 A_0}. \tag{4.19}$$

4.7.3. Main Geometric Dimensions

After the calculation of the static parameters, the main geometric dimensions of the magnetic system are determined. Basically, the ratio of width, length and height determine the resulting form factor of the actuator. The results are used for its mechanical design.

The coil dimensions, which are determined in Section 4.8.1, and the calculated reluctance area A_0 are the main parameters for the actuator footprint. Here, different rectangular layouts are feasible which can be classified by their width and length ratio. For the HPS3 actuator a quadratic footprint is chosen. This approach implies advantages for the membrane spring design, see Section 6.2.4. Yet, the drawback compared to a more elongated design are larger coil ends which increase the winding loss.

Figure 4.13 (left) shows a top view of the magnetic core with the main dimensions indicated. In order to obtain an approximately quadratic footprint, the following condition must hold:

$$l_a + 2w_c = 2w_a + 2w_c + w_{spt}. \tag{4.20}$$

Here l_a denotes the length of the reluctance area A_0 and w_a the width. The coil width is represented by w_c, which results from the coil winding area A_w. The additional distance w_{spt} maps the width of the armature support structure, which is required due to mechanical design reasons (see Section 6.2.2). It is made of steel with low magnetic permeability, hence the influence on the magnetic system is insignificant. However, its area adds to the actuator footprint. Inserting l_A from (4.20) in (4.21) and rearranging
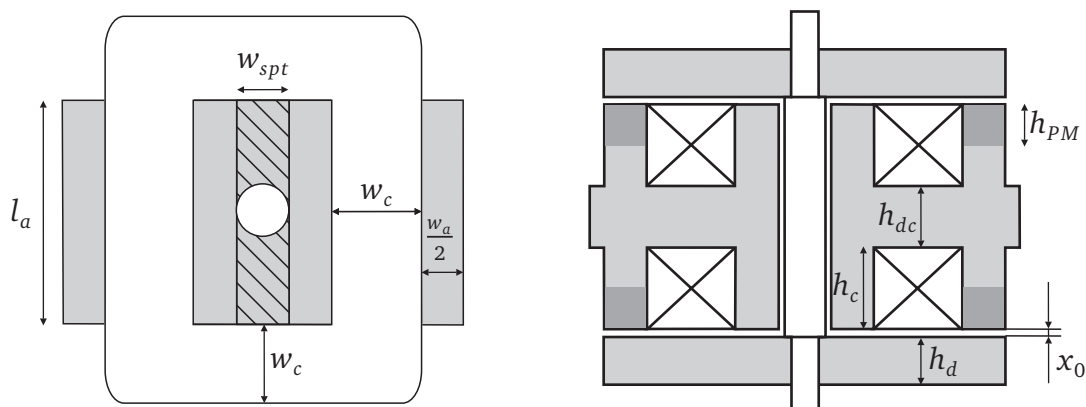

Figure 4.13.: Actuator main dimensions. Schematic top view (left, core only) and sectional view (right, core and armature).

yields the desired width

$$A_0 = l_a \cdot w_a \tag{4.21}$$

$$w_a = \frac{-w_{spt} \pm \sqrt{w_{spt}^2 + 8A_0}}{4}. \tag{4.22}$$

Here only positive results for w_a are used.

For the determination of the vertical dimensions, a constant cross-sectional area of the flux tubes in the magnetic system is assumed. Since the length of the magnetic system as calculated above is constant, the height h_d of the armature plates and the distance between the coils h_{dc} equals the afore calculated width w_a of the reluctance area. The coil height results from the coil winding area A_w which is calculated in Section 4.8.1. The length of the airgaps x_0 is given by the design objectives and the magnets' height h_{PM} is calculated in (4.18), so that the total height h_{ms} of the magnetic system is given by

$$h_d = w_a \tag{4.23}$$

$$h_{dc} = w_a \tag{4.24}$$

$$h_{ms} = 2(h_d + h_c + x_0) + h_{dc}. \tag{4.25}$$

The section view in Figure 4.13 (right) shows the main vertical dimensions.

4.8. Coil Design

4.8.1. Parameter Calculation

The coil data and in particular the wire diameter depend mainly on the maximum coil magnetomotive force $\Theta_{c,max}$, which is calculated in Section 4.7.2. The coil design influences the overall actuator performance considerably and directly determines the actuator's heating, size, weight and cost. A larger coil implies a lower current density for the same magnetomotive force and thus a lower specific thermal load. However, due to the increased coil winding area, this is achieved at the cost of size and weight.

In the following the main coil data is calculated. This includes the winding number, rated current, electric resistance, wire size and coil winding area. The approach follows the method proposed by BRAUER and KALLENBACH [9, 46].

Point of origin is the calculation of the required coil winding area A_w for a given MMF

$$A_w = \frac{\Theta_{c,max}}{J_r k_{co}}. \tag{4.26}$$

The rated current density J_r depends on the duty cycle, the mounting position and insulation of the coil and the actuator size and cooling. In addition, the load profile is important which makes an accurate determination of J_r complex. Due to experimental experiences with previously built actuators of similar setups, the current density is set to $5\,\text{A/mm}^2$ for 100 % duty cycle. The rather conservative design seems reasonable

since the HPS3 actuator has no active cooling system. For the packing factor k_{co} a copper filling of 70% is assumed which can be realized technically.

The required MMF $\Theta_{c,max}$ from (4.14) can be also written in terms of the rated voltage U_r, the temperature-dependent winding resistance R_{th} and winding number w

$$\Theta_{c,max} = i_r \cdot w = \frac{U_r}{R_{th}} \cdot w. \tag{4.27}$$

The electric resistance of the winding depends on its specific resistance $\rho_{th,r}$ at rated temperature T_r and geometrical specifications

$$R_{th,r} = \frac{\rho_{th,r} l_m w}{A_{co}} \tag{4.28}$$

$$\rho_{th,r} = \rho_{T_0} \left[1 + \alpha(T_r - T_0)\right]. \tag{4.29}$$

Here l_m denotes the average winding length and A_{co} the copper cross-sectional area. For the calculation of the specific temperature-dependent resistance the reference temperature is set to $T_0 = 20\,°C$, with a temperature coefficient of $\alpha = 3.93e^{-3}\,\mathrm{K}^{-1}$ and a specific resistance $\rho_{T_0} = 1.710^{-2}\,\Omega\mathrm{mm}^2/\mathrm{m}$. Inserting in (4.27) yields:

$$\Theta_{c,max} = \frac{U_r \cdot A_{co}}{\rho_{th} \cdot l_m}. \tag{4.30}$$

For circular wires the MMF is rewritten as:

$$\Theta_{c,max} = \frac{U_r \cdot \pi d_{co}^2}{4\rho_{th} \cdot l_m}. \tag{4.31}$$

Rearranging

$$d_{co} = \sqrt{\frac{4\Theta_{c,max}\rho_{th}l_m}{\pi U_r}} \tag{4.32}$$

yields the required copper diameter d_{co} of the wire for the given parameters. Finally, the required winding number

$$A_{co} \cdot w = A_w \cdot k_{co} \tag{4.33}$$

$$w = \frac{4A_w k_{co}}{\pi d_{co}^2} = \frac{A_w k_{co} U_r}{\Theta_{c,max}\rho_{th}l_m} \tag{4.34}$$

is calculated using the copper packing factor k_{co}.

Consequently, the winding resistance is calculated with the known winding number w using (4.28). The rated current is specified by

$$I_r = \Theta_{c,max}/w \tag{4.35}$$

which leads to the winding loss

$$P_{w,r} = I_r^2 R_{th,r}. \tag{4.36}$$

4.8.2. Inductance and Time Constant

The coil design significantly influences the actuator dynamics. Calculating the coil inductances allows for the analysis of the current rise time and the actuator's force dynamics. In addition to the static analysis, the equivalent magnetic circuit of Figure 4.12 enables the calculation of the coil inductances. For this purpose the previously calculated coil parameters of Section 4.8.1 are required. A convenient approach to the inductance determination is based on the total magnetic energy W_m of the network [33], which is stored in the N reluctances. For linear systems ($\mu = $ const.) the relation

$$W_m = \frac{1}{2}\Psi_0 I_0 = \frac{1}{2}LI_0^2 = \frac{1}{2}\sum_{l=1}^{N} V_l \Phi_l = \frac{1}{2}\sum_{l=1}^{N} \Phi_l^2 R_l \tag{4.37}$$

holds, where V_l is the magnetic voltage drop at reluctance R_l. The following assumptions are made for the analytical determination of the coil dynamics:

1. Inductance is calculated separately for each coil.

2. Mutual inductances are neglected.

3. Motion induced voltages are neglected.

Therefore, the analytical model provides only a rough assessment of the actuator dynamics. However, the precalculated inductances are useful during the first design phase. The numerical analysis illustrated in Section 4.9 enables a detailed calculation of the inductance characteristics.

The solution of the describing circuit equation system in (4.8) delivers the flux through each reluctance in the network. For the calculation the permanent magnetic MMF is set to zero since only the influence of the coil as an active MMF source on the induced current is investigated. However, the reluctances R_{PM} must be incorporated, since they restrict the coil flux.

Rearranging (4.37) yields the inductances of both coils:

$$L_1 = \frac{1}{i^2} \left(\sum_{l=1}^{N} \Phi_l^2 R_l \right) \Bigg|_{\Theta_{PM}=0, \Theta_{c2}=0} \tag{4.38}$$

$$L_2 = \frac{1}{i^2} \left(\sum_{l=1}^{N} \Phi_l^2 R_l \right) \Bigg|_{\Theta_{PM}=0, \Theta_{c1}=0}. \tag{4.39}$$

The dynamic of each coil is mainly characterized by the electrical response time

$$\tau = \frac{L}{R_{th}}, \tag{4.40}$$

where L denotes the respective inductance and R_{th} the electric coil resistance.

The time constant is independent of the winding number w of the coil for a given coil area A_w and copper packing factor k_{co} [9, 47]. The inductance can be written as a function of the winding number w and overall reluctance R_m, cf. (3.23). The resistance in contrast is basically calculated using (4.28). Inserting (4.26) and (4.27) yields

$$R_{th,r} = \frac{\rho_{th,r} l_m w^2 J_r}{\Theta_{c,max}} = \frac{\rho_{th,r} l_m w J_r}{I_r}. \tag{4.41}$$

With this result the time constant τ is rewritten as

$$\tau = \frac{k_{co} A_w}{\rho_{th,r} l_m R_m}. \tag{4.42}$$

4.9. Finite Element Analysis

For the FE analysis the software package ANSYS Release 12.0 from ANSYS INC.[1] is used. The numerical investigation aims at the calculation of performance indices such as force and inductivity. In addition, the information about the flux density distribution is used for the revision and refinement of the preliminary analytical design from Sections 4.7 - 4.8.

A 3D magnetostatic analysis with a scalar potential formulation is carried out thereby modeling the coils by SOURC36 elements. For all inner model regions SOLID96 elements are used, while the far field decay is mapped with an edge layer around the surrounding air region using INFIN111 elements. The model is implemented using the ANSYS proprietary scripting language (Ansys Parametric Design Language, ADPL) [1]. The implementation is fully parametric and enables the automatized geometry creation, meshing and postprocessing.

For the geometry creation the top-down method is used, starting with the definition of single volumes that are afterwards combined into the final shape. The axial lamination with regular electric steel sheets results in a cubic design, therefore a 3D modeling approach is used in order to incorporate edge effects that come along with the non rotation-symmetric magnetic system. Due to symmetry of the magnetic circuit, a quarter model is set up with the actuator shaft as symmetry axis (see Figure 4.14). This has two advantages: first, the meshing effort is reduced. Second, the computation time decreases due to the lower number of elements required for the volume that has to be analyzed [73, 98]. The coils are realized as primitive sources without discretization using the `race` macro which facilitates the definition of racetrack-shaped windings. The representation of the permanent magnet cuboids is simplified by conversion into one large volume per magnet row.

The material attributes of M250-35A are assigned to the soft magnetic core and armature components. Here the 50 Hz B-H curve of Figure 4.7 is used in form of a look-up table. Hysteresis effects are neglected since the hysteresis loop of the material is small. The characteristic of the permanent magnet material VACODYM 655HR is
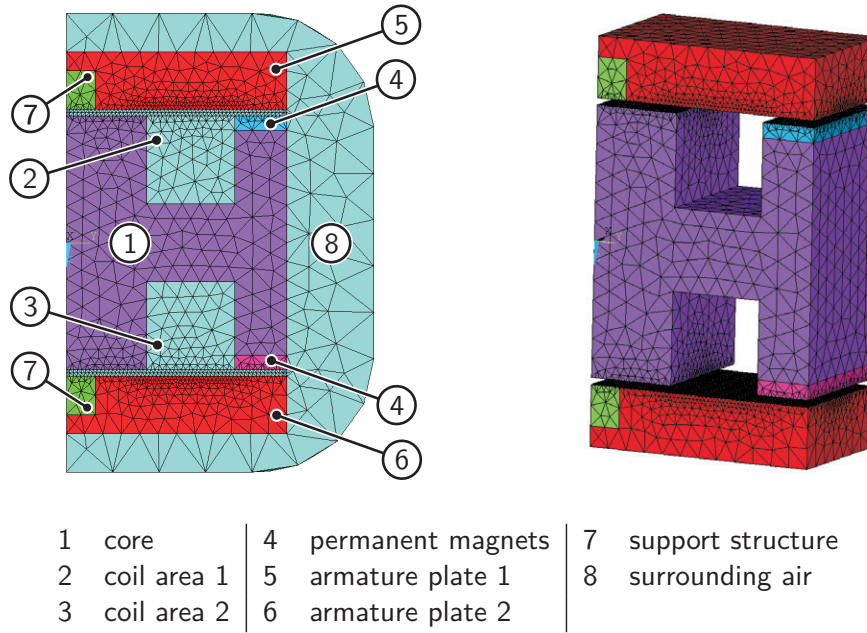
---

1   http://www.ansys.com/

1	core	4	permanent magnets	7	support structure
2	coil area 1	5	armature plate 1	8	surrounding air
3	coil area 2	6	armature plate 2		

Figure 4.14.: Actuator geometry and associated FE discretization, quarter model: lateral view (left) and 3D view (right).

described by μ_{PM}, B_r and H_{cJ}, as illustrated in Table 4.3. An axial magnetization direction parallel to the symmetry axis is chosen. All non-magnetic materials are considered as air and assigned with $\mu_r = 1$.

The meshing is automated using ADPL commands. The working airgaps are discretized by a layer thickness of at least two elements in axial direction. A smaller mesh size has no significant influence on the computed force values. But due to the 3D model, more elements have the cost of a considerably higher computation time, particularly for large characteristic diagrams of the full actuator operation range. Overall, the applied approach allows for the calculation of force values with adequate accuracy and computation time.

The flux is set to be parallel to the shaft (symmetry axis) as boundary condition. Where the boundary adjoins air regions, the far-field decay is modeled by an INFIN111 layer. In addition to the permanent magnets, the coil MMF is predefined as parameter for the magnetic excitation. The current value for each coil is adjusted individually. Force boundary conditions for the magnetic virtual work and magnetic virtual displacements are applied to the elements of soft magnetic components in order to enable the force calculation during the postprocessing.

For the investigation of a predefined operating point, the associated coil currents i_1 and i_2 are applied at a given armature position x. The model is implemented in form of nested loops. In order to minimize the computation time, the calculation is executed for all current combinations holding the armature position constant. Before the armature is moved to the next position, the model is remeshed and the calculation cycle starts again. For the total magnetic force calculation the virtual work forces on both armature plates are summed up. The ADPL macro senergy allows for the calculation of the co-energy values. The current and position input, and the computed force and energy values are exported to a text file which is used for the reduced order
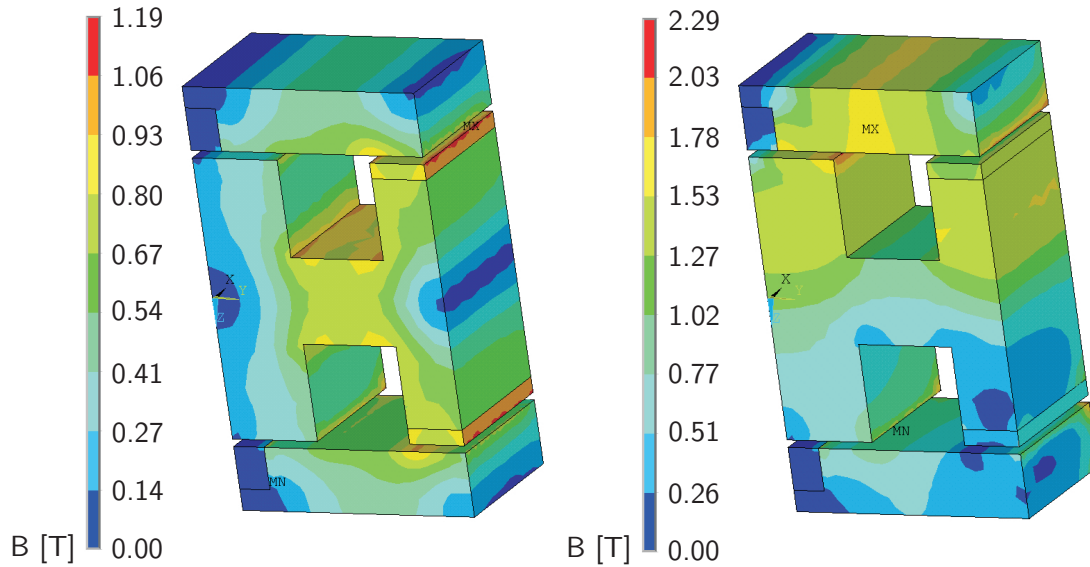
Figure 4.15.: Computed magnetic flux density distribution B [T] for a 3D quarter model of the reluctance actuator.

left: $x = 0\,\text{mm}$, $i_1 = i_2 = 0\,\text{A}$, $F = 0\,\text{N}$ *right:* $x = 0\,\text{mm}$, $i_1 = i_2 = -8.0\,\text{A}$, $F = -8076\,\text{N}$

model described in Chapter 5. The additional generation of an image file for each operating point facilitates the visual assessment of the flux density characteristics.

Figure 4.15 illustrates the computed magnetic flux density distribution for two different operating points. In both cases the armature is in neutral position, i.e. the armature displacement is zero. If no coil current is imposed, the resulting magnetic force is zero due to the symmetric design of the actuator. Based on the magnetic circuit, the required force in each armature position is achieved by superposition of coil and permanent magnet MMF, which in the case of Figure 4.15 (right) results in an increased flux in the upper path and flux cancellation in the lower path. Hence a negative force and resulting armature movement downwards is generated. Due to the position of the magnets at the airgaps and close to the armature, a remaining flux in the non-active path can still be observed. The flux density in the middle branch of the core is low for this specific operating point. However, for armature displacements $x \neq 0$ this part carries considerably more flux.

Figure 4.16 shows the computed force-current characteristic for different armature positions. All curves are calculated for equal coil currents $i_1 = i_2$. In the middle of the stroke range (armature position $x = 0$ mm) the force generation is linear with respect to the coil currents. The required force of 8 kN is reached for a coil current of 8 A. However, if the armature is positioned at the boundaries of the operating range, the force-current characteristic is nonlinear due to saturation (e.g. $x = -3$ mm, $i = -8$ A) and overcompensation of the permanent magnetic MMF by the coil MMF (e.g. $x = -3$ mm, $i = 8$ A).
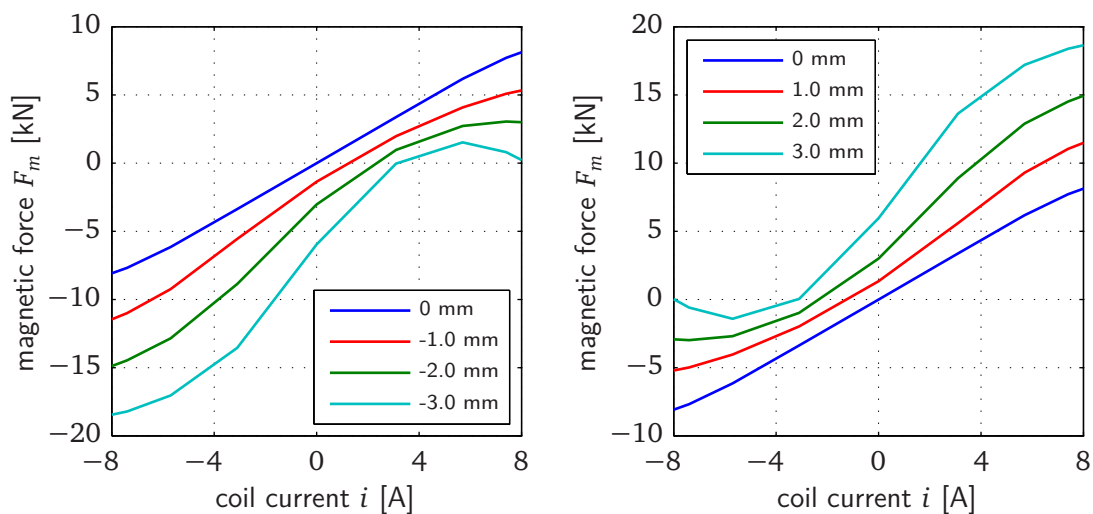
Figure 4.16.: Magnetic force at different armature positions for coil current $i_1 = i_2$.

4.10. Chapter Summary

This chapter has presented the concept for a magnetic reluctance actuator for vibration excitation and the development of the magnetic circuit. First of all, a design process for reluctance shakers is proposed. Point of departure for the design considerations are reference trajectories in form of acceleration profiles (drive files) which enable a calculation of the required actuator force. The results of comparative measurements with a passenger vehicle confirm that for a realistic road simulation a force of 5 kN and a stroke of $\pm\,2\,\text{mm}$ at frequencies up to 60 Hz are necessary.

Based on these requirements the specification of a performance enhanced actuator HPS3 is formulated. The maximum magnetic force is 8 kN with a stroke of $\pm\,3.5\,\text{mm}$, which allows for the excitation of heavier test objects and extends the range of frequencies which can be replicated. For the reluctance shaker, a topology with two armature plates and two coils is proposed. The magnetic circuit is serially polarized with surface mounted magnets close to the airgaps. The resulting negative magnetic stiffness is fully compensated by mechanical springs which enable a robust and stable operation.

The properties of different soft magnetic materials are discussed. For the flux-guiding parts of the core and the armature the electrical steel M250-35A is chosen which offers a good combination of saturation flux density, magnetic loss and price. NdFeB permanent magnets with a very high energy density provide the magnetic bias. Core and armature are fully laminated in order to avoid eddy currents and enable high dynamics.

A linear magnetic equivalent circuit model is used for the dimensioning of the magnetic system. This includes the determination of the required pole surfaces, the magnetomotive force of the permanent magnets and the calculation of the coil data. The derivation of the geometrical actuator dimensions complements the first design. Finally, a 3D finite element model allows for a detailed magnetic analysis and the accurate prediction of the generated force in the entire operating range of the actuator.

5. Energy-based Modeling and Simulation

For the preliminary design static and dynamic lumped parameter models were used. An important tool for the accurate prediction of the actuator performance is a detailed dynamics simulation. The challenges lie in the characterization of nonlinearities due to saturation and the time-varying airgap length of translatory reluctance actuators. The simulation must cope with the partly contradictory demands for high accuracy, low computational cost and sufficient flexibility.

This chapter describes an energy-based simulation approach in which the dynamic system, the actuator, is seen as an energy transformation device. The method combines the high accuracy of FE simulations with the fast computation of a reduced order analytical model. First of all, the role of co-energy for the description of nonlinear magnetic systems is explained. Moreover, the reduced order approach and the approximation of co-energy hypersurfaces by polynomials are described. Finally, the mechatronic model structure is presented in detail. The system allows for the simulation of translatory reluctance actuators with one or two energized windings.

5.1. Co-Energy

Energy methods are widely used for the calculation of torque or force in nonlinear magnetic systems. There are several motivations for adopting an energy-based perspective as described in the systematic overview by JELTSEMA and SCHERPEN [41]. First, complex physical systems can be understood as a set of simpler subsystems with a mutual energy exchange. Notably, magnetic actuators represent electro-magneto-mechanical energy transformation devices. Second, energy modeling is not restricted to a certain physical domain or to linear systems only. Therefore, energy descriptions are particularly suitable for the modeling of reluctance actuators with electric, magnetic and mechanical subdomains and typically nonlinear characteristics. Third, energy models can serve as basis for the design of control strategies [31, 79, 107].

KALLENBACH establishes the following minimal model of a solenoid using a source of electric energy (voltage source) and an energy storing element. The storage is realized in form of magnetic field energy. Furthermore, the storing element dissipates a part of its energy and converts another part into mechanical energy [47]. The simple solenoid has a current-carrying coil, a moving iron armature and a nonlinear magnetic circuit. The coil is driven by a voltage source u_0 and an internal resistance R_i, as shown in Figure 5.1. Using simple circuit elements the inductive energy-storing element is modeled as a coil with resistance R_c and flux linkage $\Psi(l, i)$, where l is the airgap length of the solenoid and i the coil current.

Applying the induction law

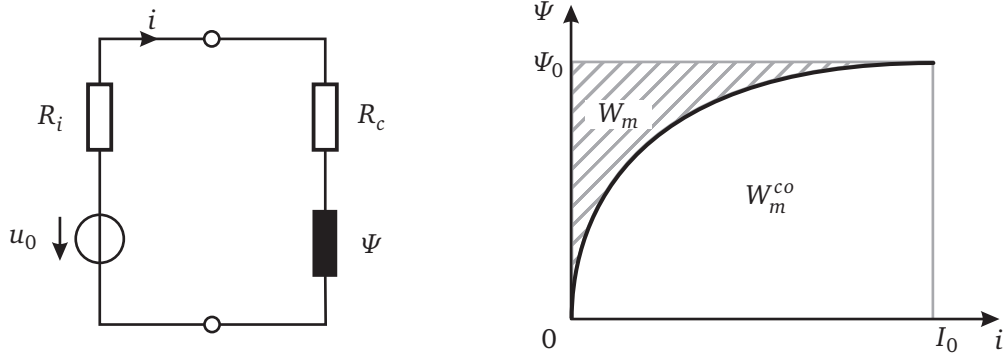$$u = \frac{\mathrm{d}\,\Psi}{\mathrm{d}\,t} \tag{5.1}$$

Figure 5.1.: Electric circuit for a simple magnetic device (left) and Ψ-i characteristics of a nonlinear magnetic circuit (right) [47].

and Kirchhoff's voltage law (KVL), the voltage equation for the simple circuit can be formulated as

$$u_0 = i(R_i + R_c) + \frac{\mathrm{d}\Psi}{\mathrm{d}t}. \tag{5.2}$$

Multiplying with $i\,\mathrm{d}t$ and integrating over time yields the total energy of the system

$$\int_0^{t_0} u_0 i \,\mathrm{d}t = \int_0^{t_0} i^2(R_i + R_c)\,\mathrm{d}t + \int_0^{\Psi_0} i\,\mathrm{d}\Psi \tag{5.3}$$

which is equivalent to

$$W_{el} = W_{therm} + W_m. \tag{5.4}$$

When the armature is fixed, the electric energy W_{el} provided by the voltage source is partially dissipated in the resistors (W_{therm}). The remaining part is stored in the current-carrying coil in form of the magnetic field energy W_m

$$W_m = \int_0^{\Psi_0} i\,\mathrm{d}\Psi. \tag{5.5}$$

In general, the relation between flux linkage and current is nonlinear due to saturation. The magnetic energy can be visualized by the area between the graph and the Ψ-axis in Figure 5.1. The complementary area between graph and i-axis is the magnetic co-energy

$$W_m^{co} = \int_0^{I_0} \Psi\,\mathrm{d}i. \tag{5.6}$$

As Figure 5.1 shows, the total energy $\Psi_0 I_0$ is composed by both areas with $W_m \neq W_m^{co}$

due to the nonlinear magnetic circuit

$$W_m + W_m^{co} = \Psi_0 I_0, \tag{5.7}$$

or more general

$$W_m + W_m^{co} = i(t)\Psi(t). \tag{5.8}$$

Unlike the magnetic energy, the co-energy has no direct physical meaning. However, it can be used as a general quantity for the derivation of important parameters in magnetic systems (see Section 5.4).

5.2. Reduced Order Approach

Problems in the modeling of magnetic actuators arise mainly from their inherent nonlinear properties. This is basically due to two reasons. First, the reluctance force is nonlinear with respect to the length of the active airgap and accordingly to the armature position, see (3.15). Second, the generated force exhibits in many cases a nonlinear relation to the injected coil current, which is caused by the B-H curve of the soft magnetic material. In order to obtain a small overall actuator size, the material is often operated well into the saturation range for advanced designs. In addition to these two main concerns, magnetic devices show other complex characteristics such as fringing flux, which complicates detailed modeling.

General Objectives

The objective of the advanced model presented in this section is an accurate and fast simulation of the developed magnetic actuators HPS2 (see Section 6.2.4) and HPS3. The model should be suitable for direct implementation in a system simulation software package and allow for control design. Furthermore, important phenomena such as the nonlinearity of magnetic force with respect to coil currents and armature position as well as flux leakage should be incorporated.

Basically three requirements on a simulation model can be formulated according to [50]:

- high accuracy

- acceptable computational cost

- sufficient flexibility.

Coupled Simulation

As discussed in Section 3.4.4, there is no single modeling method which is capable of fulfilling all these requirements. Thus a hybrid approach is chosen [49,80], which couples two simulation programs. Here a FE simulation program and a system simulation program are used.
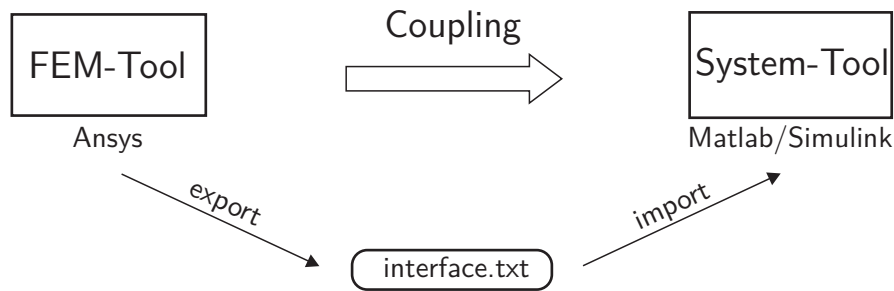
Figure 5.2.: Overview of the modeling and simulation procedure.

As illustrated in Figure 5.2, the data exchange between the two programs is executed one way only and not at simulation time, therefore the process is classified as an offline coupling [50]. The method uses energy values as basis for the data exchange. This seems reasonable, since the actuator is an energy converter and can be essentially described by energy functions as presented in Section 5.4. From the energy values, which are computed in the FE simulation, an analytical description is derived. During this step a significant model order reduction is carried out. This is achieved by formulating an analytical approximation for the discrete energy values which serve as interface between the two programs.

Reduced Order Modeling Procedure

Figure 5.3 shows the basic procedure for the reduced order modeling process. The entire modeling process is structured in five substeps. Starting point is the actuator as an electromechanical system. In order to capture the complex physics, a FE model is set up, see Section 4.9. The model must be parametric and allow for the calculation of discrete co-energy values for arbitrary points in the operating range of the actuator. In the case of the actuators considered in this thesis, the co-energy is a function of coil currents and armature position. Hence the model must allow for variation of these three parameters.

In the second step the computed co-energy values are saved in a lookup table and exported as text file. In Figure 5.4 a typical co-energy table for reluctance actuators is shown.

Consequently, an approximation of the stored values by analytical functions is calculated, see Section 5.3. This yields a compact description of the co-energy values, which is used for the derivation of important system parameters, as explained in Section 5.4.

Finally, the analytical approximation is implemented in a system simulation program and used to simulate the dynamic behavior of the actuator. The same implementation can be used for control design purposes as well.

Advantages

The reduced order model has several advantages compared to the other modeling methods and integrates very well into the standard actuator development process. As described in Section 3.4.2 and Section 4.9 a FE model is required for a detailed analysis
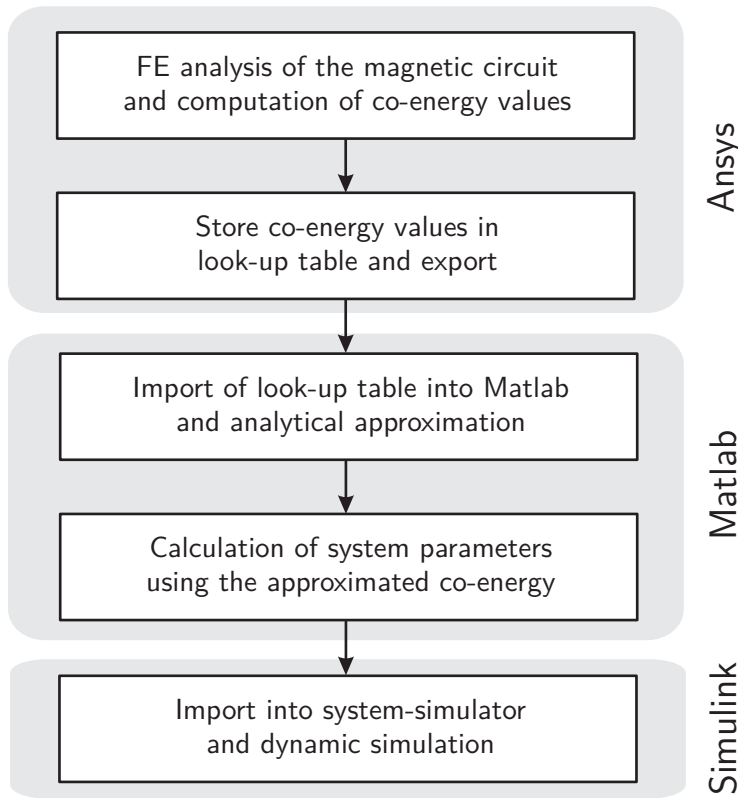
Figure 5.3.: Modeling procedure of the reduced order approach.

```
#################################
 x[mm]    i[A]      F_mag[N]    W_co[J]
#################################
 1.1      2.50      5995.546    125.170
 1.10     3.00      6339.593    129.399
 1.10     3.50      6622.677    134.050
 1.10     4.00      6854.689    139.121
 1.10     4.50      7039.732    144.575
 1.10     5.00      7163.660    150.407
 1.20    -5.00     -5035.799    135.991
 1.20    -4.50     -4934.963    130.435
 1.20    -4.00     -4709.850    125.462
 1.20    -3.50     -4343.577    121.097
 1.20    -3.00     -3773.789    117.384
 ...      ...       ...         ...
```

Figure 5.4.: Interface text file: listing of FEM results.

of the magnetic circuit. The model must be parametric with respect to the electrical excitation and armature position to allow for the inspection of different operating points. The calculation of co-energy values is just a minor extension to the already existing model implementation and requires only a small additional computation effort.

FE models are typically very large with many DOFs, and the resulting equation system has a high computational cost. In contrast, the energy based modeling method allows for an order reduction during the approximation process. The size of the analytical reduced order model is determined by the degrees of the ansatz functions chosen for the approximation of the co-energy hypersurfaces. In typical applications a satisfying approximation result can already be obtained with a low polynomial degree. However, as pointed out in [51], the analytical model can be subjected to further mathematical order reduction methods, such as the singular value decomposition or balanced truncation.

The outcome is a very compact analytical model, suitable for dynamic simulation in typical system simulation programs. In contrast to the static FE computations, this approach enables a time-dependent inspection of the actuator. Instead of characteristic diagrams for the steady state behavior, a full model of the actuator dynamics is available.

Due to the co-energy computation during the FE simulation, phenomena such as saturation and flux leakage are easily incorporated. Furthermore, the variable airgap length of the translatory reluctance actuator is included as well.

A detailed comparison with other modeling methods is given in Section 3.4.4. The core advantages are as follows:

- order reduction: compact, fast simulation model

- dynamic simulation model

- sufficient accuracy

- incorporation of flux leakage

- incorporation of nonlinearities due to saturation and reluctance principle

- suitability for control design

- easy integration into the development tool chain.

Implementation

The FE model is implemented using the simulation package ANSYS. Main features of the model are an adjustable armature position and current-fed coils. A script written in the ANSYS proprietary programming language ADPL enables the model parameterization and the computation of the characteristic co-energy table. Details of the model setup are given in Section 4.9. For the computation of the co-energy values ADPL provides the macro `senergy`, cf. [1, 80]. The script allows handling and storing essential model parameters which are exported upon completion of the computation to an ASCII file.

The subsequent approximation of the co-energy hypersurface, the derivation of system parameters and the parameterization of the simulation is subdivided into three modules. This approach facilitates debugging and the developing of add-ons, e.g. for data analysis and visualization. The implementation is realized in the numerical computing environment and programming language MATLAB/SIMULINK (R2011b) from MATHWORKS[1], which offers a wide range of possibilities for matrix manipulation and plotting of data and functions. This way, the full numerical possibilities of the provided toolboxes can be used, such as least squares fitting and spline approximation.

SIMULINK has been chosen for system simulation since it offers tight integration with the rest of the MATLAB environment and the model can be parameterized from MATLAB. This allows for an easy analysis of parameter variations. In addition, the combination of both programs is well suited for control design, as described in Section 5.6.

Furthermore, the MATLAB/SIMULINK implementation integrates very well into the DSPACE-based experimental setup, see Section 6.3. This reduces the time required for the experimental validation of simulation results significantly.

5.3. Approximation Methods

The discrete co-energy values are described by an analytical function. For this purpose a polynomial approximation using the least-squares method is carried out [23]. If the actuator is in a single-phase operating mode and both coils are connected in series, the characteristic co-energy map is a two-dimensional function of armature position x and coil current i. Initially, for each current value an optimal polynomial with degree m in position direction is calculated. The coefficients of these polynomials show a current-dependency which is again approximated by a least-squares fit in current direction with degree n polynomials.

The introduction of position and current vectors

$$\boldsymbol{x}^T = \begin{pmatrix} x^m & x^{m-1} & \ldots & x & 1 \end{pmatrix} \tag{5.9}$$

$$\boldsymbol{i}^T = \begin{pmatrix} i^n & i^{n-1} & \ldots & i & 1 \end{pmatrix} \tag{5.10}$$

enables the formulation of the co-energy function in matrix-vector notation as

$$W_m^{co} = f(x,i) = \boldsymbol{x}^T \cdot \boldsymbol{C} \cdot \boldsymbol{i} = \sum_{j=0}^{m} \sum_{k=0}^{n} c_{j,k} x^j i^k. \tag{5.11}$$

Here, the single coefficients $c_{j,k}$ are combined in the coefficient matrix $\boldsymbol{C}$ which contains the weights for all products of x_j and i_k. Besides the concise representation, the notation as a bilinear form enables a straightforward implementation in the system simulation software [117]. For the determination of relevant system parameters as derivatives of the co-energy function only the position and current vectors are modified while the coefficient matrix remains unchanged.
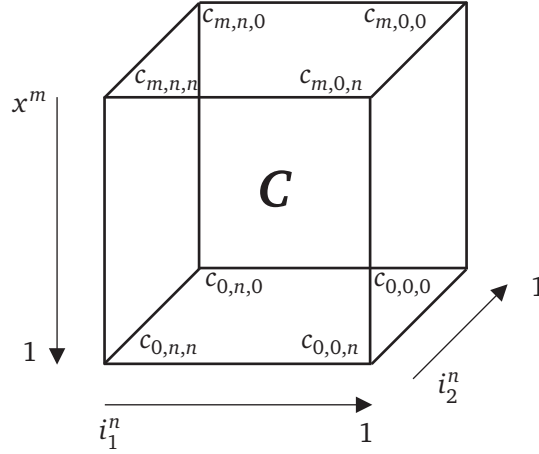
---

1 http://www.mathworks.com/

Figure 5.5.: Implementation of the coefficient tensor as a three-dimensional array.

If both windings of the HPS3 actuator are individually driven and carry different currents, the model must be extended by one dimension. Now two current vectors

$$\boldsymbol{i_1}^T = \begin{pmatrix} i_1^n & i_1^{n-1} & \dots & i_1 & 1 \end{pmatrix} \tag{5.12}$$

$$\boldsymbol{i_2}^T = \begin{pmatrix} i_2^n & i_2^{n-1} & \dots & i_2 & 1 \end{pmatrix} \tag{5.13}$$

are introduced in addition to the position vector for the approximation. The co-energy is then written as

$$W_m^{co} = f(x, i_1, i_2) = \boldsymbol{C} \cdot \boldsymbol{x} \cdot \boldsymbol{i_1} \cdot \boldsymbol{i_2} = \sum_{j=0}^{m} \sum_{k=0}^{n} \sum_{l=0}^{n} c_{j,k,l} x^j i_1^k i_2^l. \tag{5.14}$$

Here the coefficients $c_{j,k,l}$ represent the weight of all combinations of x^j, i_1^k and i_2^l. In addition to the notation as summation, the co-energy can be represented more concise as a vector-tensor product with the coefficient tensor $\boldsymbol{C}$ of order three. For implementation purposes the coefficient tensor can be interpreted straightforward as a multidimensional array, as illustrated in Figure 5.5. As in the bivariate case, the derivation of relevant system parameters is possible by manipulating the current and position vectors only.

For the simulations in this thesis, polynomial degrees of $m = 5$ and $n = 4$ are used which enable a sufficient approximation accuracy and maintain a very compact model with a 6×5 coefficient matrix C. The influence of errors in the basic data on the approximated values is important for the overall approximation quality. For an assessment the Lebesgue constant is used which represents the absolute condition number of the approximation [102]. For equidistantly distributed nodes the Lebesgue constant grows exponentially. Thus non-equidistant Chebyshev nodes are used, which minimize the condition number by a concentration of nodes at the boundaries of the approximation range and yield an only logarithmically growing condition number.

Chebyshev nodes ξ_r of the second kind [4] are defined by

$$\xi_r = \cos\left(\frac{r\pi}{s}\right), \qquad r = 0, 1, \ldots, s \tag{5.15}$$

in the interval $[-1, 1]$. In order to cover the operating range of the actuator, a linear transformation is used

$$x_r = a + \frac{b-a}{2}(\xi_r + 1) \tag{5.16}$$

with x_r being the nodes in the arbitrary interval $[a,b]$. For the approximation nine nodes are used ($s = 8$), since a higher node number has no significant influence on the simulation results.

The Chebyshev distribution is already incorporated in the FE model for the numerical computation of the co-energy values at the respective nodes. Therefore, an excessive overshoot at the boundaries of the approximation range can be avoided and oscillations of the approximation polynomials are effectively reduced.

5.4. System Parameters

For the sake of clarity, the determination of the system parameters is first carried out for the single winding case [86]. Then the representation is expanded for two energized windings as it will be used for the HPS3 actuator. A detailed introduction to the energy conversion of nonlinear permanent magnet systems with multiple windings is presented by STRAHAN in [105].

5.4.1. Single Energized Winding

The law of energy conservation for a magnetic actuator

$$dW_{el} - dW_{therm} = dW_m + dW_{mech} \tag{5.17}$$

states that the differential change of electrical input energy dW_{el} can be split up into the change of dissipated energy dW_{therm}, stored magnetic energy dW_m and mechanical energy dW_{mech}. The net input energy on the left side of (5.17) can be formulated with (5.2) as

$$dW_{el} - dW_{therm} = u_0 i \, dt - (R_i + R_c) i^2 dt = i \, d\Psi. \tag{5.18}$$

For the determination of the magnetic force F_m the concept of virtual work is applied

$$F_m \cdot dx = dW_{mech}, \tag{5.19}$$

which yields due to the energy conservation expressed in (5.17):

$$\begin{aligned} dW_m &= i \cdot d\psi - dW_{mech} \\ &= i \cdot d\psi - F_m \cdot dx. \end{aligned} \tag{5.20}$$

The differential of $(i\Psi)$ is described by

$$d(i\Psi) = i \cdot d\Psi + \Psi \cdot di. \tag{5.21}$$

Then the differential form of (5.8) can be written with (5.20) and (5.21) as

$$
\begin{aligned}
dW_m^{co}(x,i) &= d(i\psi) - dW_m(\psi,x) \\
&= i \cdot d\Psi + \Psi \cdot di - i \cdot d\Psi + F_m \cdot dx \\
&= \psi \cdot di + F_m \cdot dx.
\end{aligned} \tag{5.22}
$$

Generally, the magnetic co-energy is a time-dependent function of coil current i and armature displacement x, $W_m^{co} = f(x(t), i(t))$, which leads to the differential

$$dW_m^{co}(x,i) = \frac{\partial W_m^{co}(x,i)}{\partial i} \cdot di + \frac{\partial W_m^{co}(x,i)}{\partial x} \cdot dx. \tag{5.23}$$

By comparing (5.22) and (5.23), expressions for magnetic force

$$F_m = \frac{\partial W_m^{co}(x,i)}{\partial x} \tag{5.24}$$

and flux linkage

$$\Psi = \frac{\partial W_m^{co}(x,i)}{\partial i} \tag{5.25}$$

are derived. Furthermore, the induced voltage in the winding is denoted by

$$u_{ind} = \frac{d\Psi}{dt} \tag{5.26}$$

and can be finally rewritten using the magnetic co-energy as:

$$u_{ind}(i,x) = \frac{\partial^2 W_m^{co}}{\partial i^2} \cdot \frac{di}{dt} + \frac{\partial^2 W_m^{co}}{\partial i \partial x} \cdot \frac{dx}{dt}. \tag{5.27}$$

5.4.2. Two Energized Windings

The derivation of system parameters from the magnetic co-energy is now extended for the case of two windings that are energized with currents i_k ($k = \{1,2\}$) respectively. Similar to the case of a single winding, the basis for the derivation is the conservation of energy. Point of departure is (5.18), which is modified for the two-phase case:

$$
\begin{aligned}
dW_{el} - dW_{therm} &= u_1 \cdot i_1 \cdot dt + u_2 \cdot i_2 \cdot dt - (R_{i1} + R_{c1})i_1^2 dt - (R_{i2} + R_{c2})i_2^2 dt \\
&= d\Psi_1 \cdot i_1 + d\Psi_2 \cdot i_2.
\end{aligned} \tag{5.28}
$$

The differential magnetic energy is then given by (cf. (5.20))

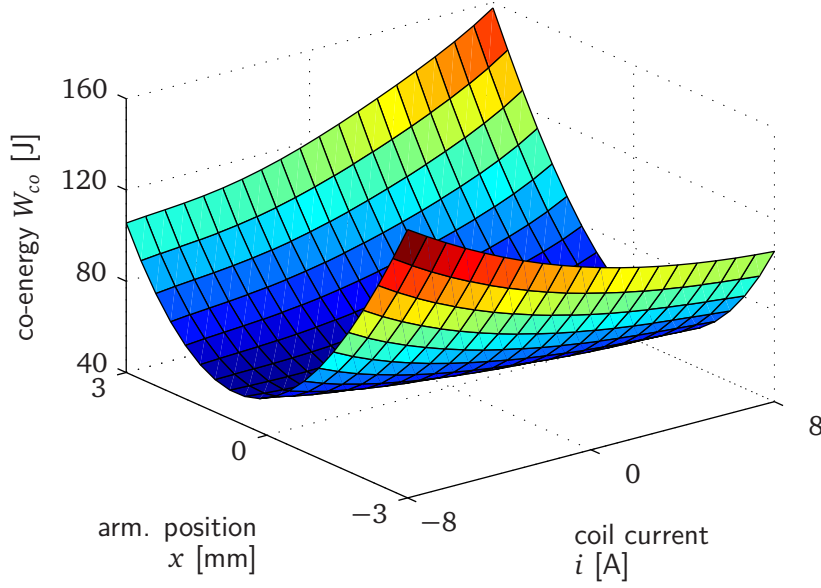$$dW_m = i_1 \cdot d\psi_1 + i_2 \cdot d\psi_2 - dW_{mech}$$

Figure 5.6.: Co-energy function for coil currents $i_1 = i_2$.

$$= i_1 \cdot \mathrm{d}\psi_1 + i_2 \cdot \mathrm{d}\psi_2 - F_m \cdot \mathrm{d}x. \tag{5.29}$$

In the case of two windings

$$W_m(x, i_1, i_2) + W_m^{co}(x, i_1, i_2) = i_1 \cdot \Psi_1 + i_2 \cdot \Psi_2 \tag{5.30}$$

holds according to [105]. Considering

$$\mathrm{d}(i_1 \Psi_1 + i_2 \Psi_2) = i_1 \cdot \mathrm{d}\Psi_1 + \Psi_1 \cdot \mathrm{d}i_1 + i_2 \cdot \mathrm{d}\Psi_2 + \Psi_2 \cdot \mathrm{d}i_2 \tag{5.31}$$

and inserting (5.29), the differential magnetic co-energy yields:

$$\begin{aligned}
\mathrm{d}W_m^{co}(x, i_1, i_2) &= \mathrm{d}(i_1 \psi_1 + i_2 \psi_2) - \mathrm{d}W_m(x, \psi_1, \psi_2) \\
&= \psi_1 \cdot \mathrm{d}i_1 + \psi_2 \cdot \mathrm{d}i_2 + F_m \cdot \mathrm{d}x.
\end{aligned} \tag{5.32}$$

In the general case the magnetic co-energy is a function of coil currents i_k and armature displacement x, thus $W_m^{co} = f(x, i_1, i_2)$. Accordingly the total differential of W_m^{co} is calculated as:

$$\mathrm{d}W_m^{co}(x, i_1, i_2) = \frac{\partial W_m^{co}(x, i_1, i_2)}{\partial i_1} \cdot \mathrm{d}i_1 + \frac{\partial W_m^{co}(x, i_1, i_2)}{\partial i_2} \cdot \mathrm{d}i_2 + \frac{\partial W_m^{co}(x, i_1, i_2)}{\partial x} \cdot \mathrm{d}x. \tag{5.33}$$

In order to obtain the equations for force and flux linkage, this result is compared to (5.32) which leads to the final equation for magnetic force

$$F_m(x, i_1, i_2) = \frac{\partial W_m^{co}(x, i_1, i_2)}{\partial x} \tag{5.34}$$
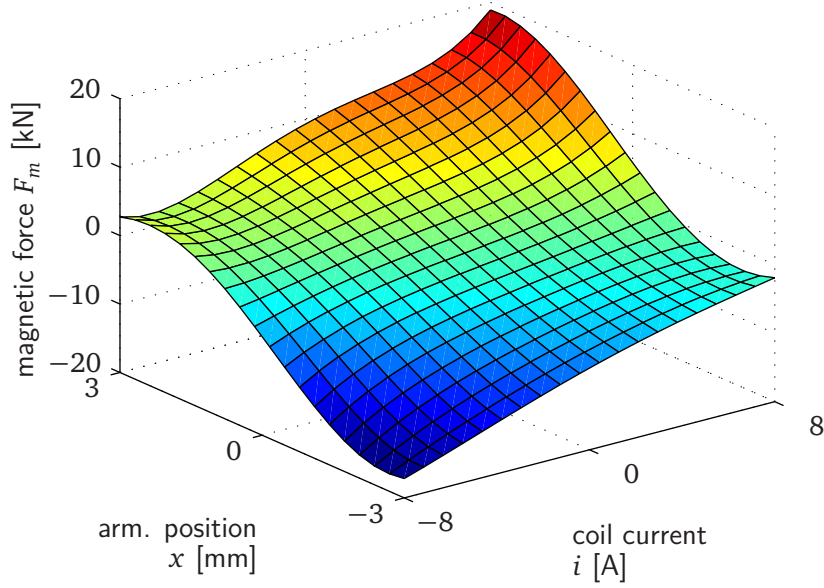
and flux linkage

Figure 5.7.: Magnetic force function for coil currents $i_1 = i_2$.

$$\Psi_k(x, i_1, i_2) = \frac{\partial W_m^{co}(x, i_1, i_2)}{\partial i_k} \quad \text{with} \quad k \in \{1, 2\} \tag{5.35}$$

for two current-carrying coils. The induced voltages are calculated by time derivation of flux linkage $\Psi_k(t)$

$$u_{k,ind} = \frac{d\Psi_k(t)}{dt}, \tag{5.36}$$

which can be expressed as a function of magnetic co-energy $W_m^{co}(x(t), i_1(t), i_2(t))$ as well:

$$u_{1,ind} = \frac{d}{dt}\left(\frac{\partial W_m^{co}(x(t), i_1(t), i_2(t))}{\partial i_1(t)}\right) =$$

$$= \underbrace{\frac{\partial^2 W_m^{co}}{\partial i_1^2(t)}}_{\mathscr{L}_1} \cdot \frac{di_1(t)}{dt} + \underbrace{\frac{\partial^2 W_m^{co}}{\partial i_2(t)\partial i_1(t)}}_{\mathscr{L}_{12}} \cdot \frac{di_2(t)}{dt} + \underbrace{\frac{\partial^2 W_m^{co}}{\partial i_1(t)\partial x(t)}}_{\mathscr{V}_1} \cdot \frac{dx(t)}{dt} \tag{5.37}$$

and

$$u_{2,ind} = \frac{d}{dt}\left(\frac{\partial W_m^{co}(x(t), i_1(t), i_2(t))}{\partial i_2(t)}\right) =$$

$$= \underbrace{\frac{\partial^2 W_m^{co}}{\partial i_2^2(t)}}_{\mathscr{L}_2} \cdot \frac{di_2(t)}{dt} + \underbrace{\frac{\partial^2 W_m^{co}}{\partial i_1(t)\partial i_2(t)}}_{\mathscr{L}_{21}} \cdot \frac{di_1(t)}{dt} + \underbrace{\frac{\partial^2 W_m^{co}}{\partial i_2(t)\partial x(t)}}_{\mathscr{V}_2} \cdot \frac{dx(t)}{dt}.$$

$$\tag{5.38}$$

For the sake of better readability the following symbols are introduced:

$$\mathscr{F}_m = \mathscr{F}_m(x(t), i_1(t), i_2(t)) = \frac{\partial\, W_m^{co}(x(t), i_1(t), i_2(t))}{\partial\, x(t)} \tag{5.39}$$

$$\mathscr{L}_1 = \mathscr{L}_1(x(t), i_1(t), i_2(t)) = \frac{\partial^2\, W_m^{co}(x(t), i_1(t), i_2(t))}{\partial\, i_1^2(t)} \tag{5.40}$$

$$\mathscr{L}_2 = \mathscr{L}_2(x(t), i_1(t), i_2(t)) = \frac{\partial^2\, W_m^{co}(x(t), i_1(t), i_2(t))}{\partial\, i_2^2(t)} \tag{5.41}$$

$$\mathscr{L}_{12} = \mathscr{L}_{12}(x(t), i_1(t), i_2(t)) = \frac{\partial^2\, W_m^{co}(x(t), i_1(t), i_2(t))}{\partial\, i_2(t)\,\partial\, i_1(t)} \tag{5.42}$$

$$\mathscr{L}_{21} = \mathscr{L}_{21}(x(t), i_1(t), i_2(t)) = \frac{\partial^2\, W_m^{co}(x(t), i_1(t), i_2(t))}{\partial\, i_1(t)\,\partial\, i_2(t)} \tag{5.43}$$

$$\mathscr{L}_{12} = \mathscr{L}_{21} \tag{5.44}$$

$$\mathscr{V}_1 = \mathscr{V}_1(x(t), i_1(t), i_2(t)) = \frac{\partial^2\, W_m^{co}(x(t), i_1(t), i_2(t))}{\partial\, x(t)\,\partial\, i_1(t)} \tag{5.45}$$

$$\mathscr{V}_2 = \mathscr{V}_2(x(t), i_1(t), i_2(t)) = \frac{\partial^2\, W_m^{co}(x(t), i_1(t), i_2(t))}{\partial\, x(t)\,\partial\, i_2(t)}. \tag{5.46}$$

Here $\mathscr{L}_i$ denotes the self-inductances, $\mathscr{L}_{ij}$ the mutual inductances and $\mathscr{V}_i$ the back electromotive force (EMF) factors. Figure 5.6 illustrates the magnetic co-energy function of the HPS3 actuator for the case of equal winding currents. The magnetic force obtained by partial derivation for position is shown in Figure 5.7.

5.5. Actuator Model

Magnetic actuators realize an electro-magneto-mechanical energy-conversion. Hence the overall actuator model is divided into the three domains of electrics, magnetics and mechanics. The advantage is a straightforward setup of each subsystem while the coupling between the subsystems is realized on the top level. The differential equations for the individual domains can be expressed in form of block diagrams which in turn are well suitable for direct implementation in the system simulator. BRAUER delivers the following description for the standard transient operation of electromagnetic actuators which illustrates the interaction of the individual subsystems [9]:

1. The coil is energized by a voltage and consequently supplies a current.

2. The coil current rises, determined partly by the electrical time constant.

3. The magnetic flux density increases, determined partly by the magnetic diffusion time.

4. The force rises as the magnetic flux density rises.

5. The force produces an acceleration of the armature and attached load, acting back on the magnetic flux and coil current via induction.

5.5.1. Electric Circuit

The electric circuit converts the input voltages into coil currents. The HPS3 actuator features two separate windings which are fed by an independent voltage source respectively

$$u_k(t) = R_k \cdot i_k(t) + u_{k,ind}(t) = R_k \cdot i_k(t) + \frac{d\Psi_k(t)}{dt}, \quad k = \{1,2\}. \tag{5.47}$$

This setup can be modeled by two simple RL circuits which are extended by a coupling inductivity and a speed dependent voltage source as illustrated in Figure 5.8. However, with the exception of resistances R_k, which are assumed to be constant,
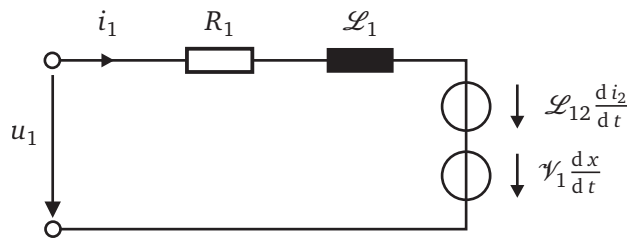

Figure 5.8.: Equivalent electric circuit of coil 1.

these parameters are nonlinear functions of coil currents and armature position, since the armature motion causes large changes in flux linkage. Flux linkage itself varies nonlinearly with current as well which is due to nonlinear material properties causing saturation. Both circuits are coupled indirectly by the functions for inductivities L_k and back-emf factors V_k. Direct coupling is modeled via the mutual inductance L_{12}. Using the co-energy representation for induced voltages (5.37) and (5.38) the electric subsystem is represented by:

$$u_1(t) = R_1 \cdot i_1(t) + \mathscr{L}_1 \cdot \frac{di_1}{dt} + \mathscr{L}_{12} \cdot \frac{di_2}{dt} + \mathscr{V}_1 \cdot \frac{dx}{dt} \tag{5.48}$$

$$u_2(t) = R_2 \cdot i_2(t) + \mathscr{L}_2 \cdot \frac{di_2}{dt} + \mathscr{L}_{21} \cdot \frac{di_1}{dt} + \mathscr{V}_2 \cdot \frac{dx}{dt}. \tag{5.49}$$

Figure 5.9 shows the block diagram for the electric subsystem.

5.5.2. Magnetic Force

The magnetic subsystem realizes the magneto-mechanical force generation of the actuator. In this process the coil currents are converted via a magnetic field into a magnetic force F_m. As shown in the case of a simple solenoid in Section 3.1, the reluctance force

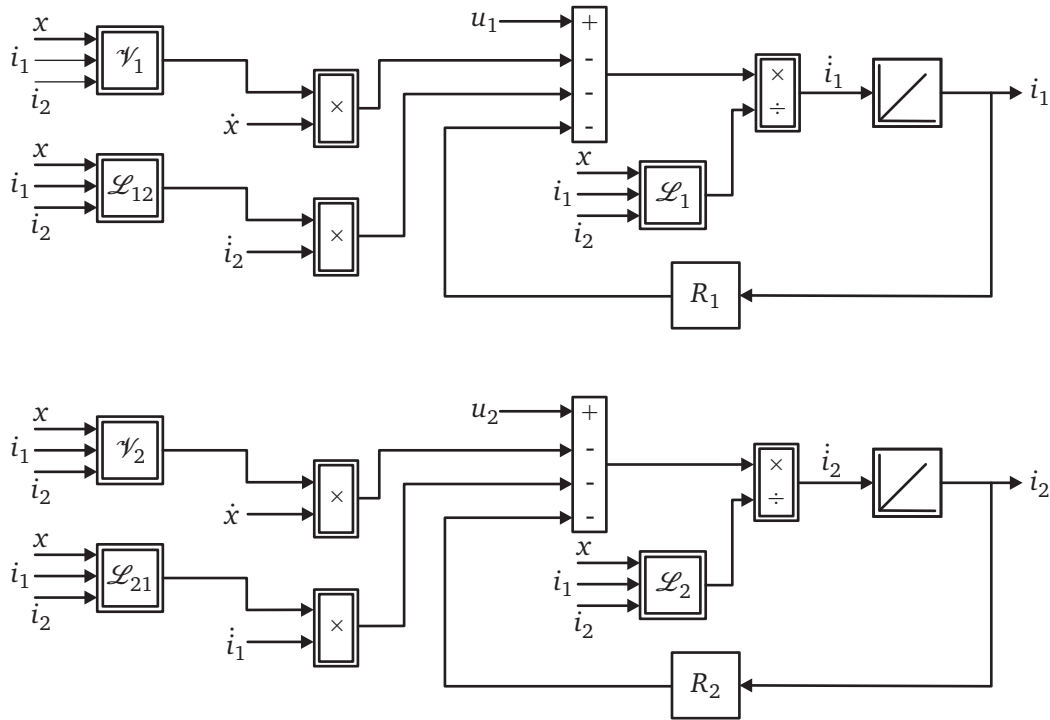$$F_{re} = \frac{1}{2}\frac{\mu_0 A}{l^2}(wi)^2 \tag{5.50}$$

Figure 5.9.: Block diagram of the electric circuit with input voltages u_k and output currents i_k.

is nonlinear with respect to current i and airgap length l. According to (5.34) the force is computed by deriving the magnetic co-energy for armature position x

$$F_m = \mathscr{F}_m(x(t), i_1(t), i_2(t)) = \frac{\partial\, W_m^{co}(x_1(t), i_1(t), i_2(t))}{\partial\, x(t)}.$$ (5.51)

Consequently, the block diagram for the magnetic subsystem consists of a single block representing $\partial W_m^{co}/\partial x$ as shown in Figure 5.10. A comparison between the analytical function of the magnetic force and the numerical results from the FE computation is illustrated in Figure 5.11. For this purpose both coils are loaded with the same current. The plots clearly show the nonlinearity of the generated magnetic force with respect to the coil current and armature position. The approximation yields a good match in the entire operating range.
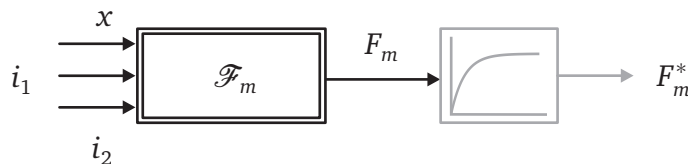

Figure 5.10.: Block diagram of the magnetic force generation with input coil currents i_k and armature position x. Output is the magnetic force F_m. The optional low-pass filter for eddy current modeling is drawn in grey.
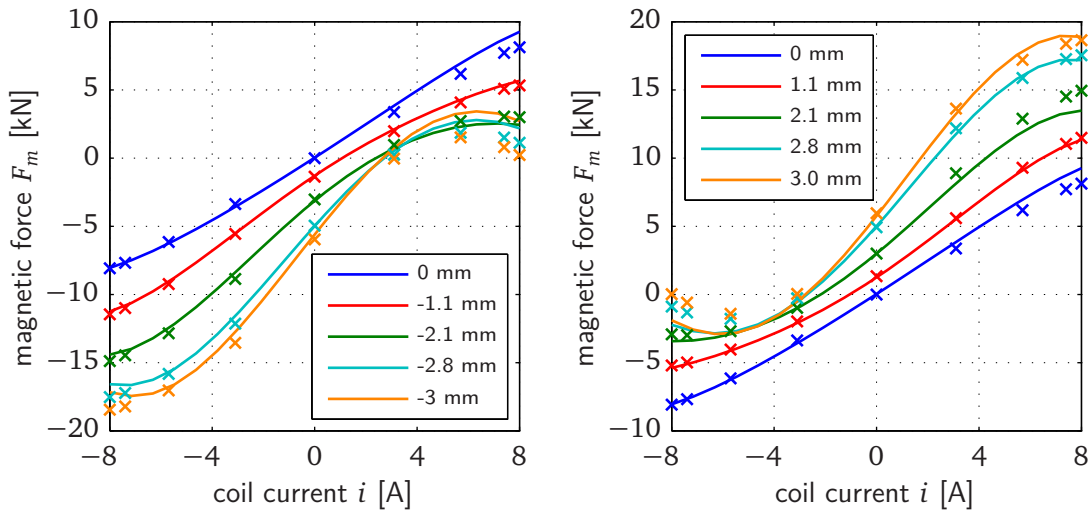
Figure 5.11.: Magnetic force at different armature positions for coil current $i_1 = i_2$. Numerical results from FE computation [×] and analytical approximation by co-energy model [–].

5.5.3. Eddy Currents

A dynamic operation requires a fast variation of coil currents and armature position, which causes additional losses due to eddy currents. The influence can be neglected for the HPS3 actuator since its flux-carrying parts are fully laminated. However, the soft-magnetic parts of the HPS2 actuator, which is presented in Section 6.2.4, are made of PERMENORM 5000 H2. Although the alloy combines low hysteresis losses with a comparatively high specific electric resistance ρ, eddy current losses have a significant influence at higher frequencies due to the solid construction of the core and armature.

Various approaches for the incorporation of eddy current influence in the modeling of the electromagnetic energy conversion are given in the literature, concerning both the electric and magnetic subsystem. A classic approach is the insertion of an eddy current resistance parallel to the inductance of the respective coil which allows for the calculation of transients in a simple way [47]. For the determination of a suitable resistance value the system is loaded with a voltage pulse, thereby measuring the current profile. In [80] the introduction of an additional eddy current excitation is described so that the co-energy is a function $f(x, i, i_e)$ of armature position, coil current and eddy current. The method has the advantage that the effects on both the electric and magnetic subsystem are expressed clearly owing to the incorporation of the eddy current influence in the co-energy formulation. However, for this purpose the eddy current distribution and magnitude must be estimated prior to simulation which is challenging.

The consideration of the frequency-dependent characteristics of the electric and magnetic system via transfer functions is described in [25, 124, 126]. This approach is also chosen for modeling the eddy current influence on the force generation within the co-energy model. The main advantage is a comparatively easy experimental determination of the current-force transfer function. For this purpose a frequency sweep of the injected coil currents is carried out while simultaneously the generated

magnetic force is measured in a force test rig, cf. Section 7.1.1. The frequency-dependent damping and phase lag is modeled by a first-order low pass filter which has the following transfer function in the Laplace domain

$$G_{lp}(s) = \frac{F_m^*}{F_m} = \frac{1}{1 + s \cdot {}^1\!/_{2\pi f_c}}. \tag{5.52}$$

In order to realize a frequency-dependent transfer function of the magnetic system, the filter is connected in series with the already existing force generation block. Experimental results show a cutoff-frequency of $f_c \approx 45\,\text{Hz}$ for the HPS2 actuator [18]. The positive influence of the eddy current modeling is clearly visible in the validation by experimental results presented in Chapter 7.

5.5.4. Mechanics

In the model of the mechanic system only actuator components are incorporated. Mounted loads - as during normal operation in vibration test rigs - are explicitly not considered here. However, it is worth noting that the attached load significantly influences the overall system properties. For the controlled excitation of mechanically more complex test objects with several oscillating masses, knowledge of the eigen behavior is beneficial. Multibody-models for the vibration testing of components and cars are described in [33, 53].

The mechanical subsystem converts the magnetic force produced in the process of electro-magnetic force generation into an armature motion. The main mechanical parts are the moving armature and the stationary core. The armature is composed of two pull plates connected through the armature shaft. The guiding via membrane springs provides both the necessary radial bearings for the motion and the compensation of the negative stiffness caused by the embedded permanent magnets. The iron core of the stator is attached to the surroundings via a fixed support through the casing. Therefore, the reluctance force acting on the surfaces of armature and core leads to an armature motion relative to the stationary core.

If the armature is considered as a rigid body with one degree of freedom (DOF) along the axis, a mass-spring-damper model can be set up. There are four force components in the system: magnetic force F_m, gravitational force mg, damping force F_d and spring force F_s. The application of Newton's second law

$$m \cdot a(t) = \sum_i F_i(t) \tag{5.53}$$

leads to the differential equation describing the armature motion in x-direction:

$$m \cdot \ddot{x}(t) = F_m(t) - F_s(t) - F_d(t) - mg. \tag{5.54}$$

The magnetic force F_m is directly obtained from the co-energy function by position derivation according to (5.34).
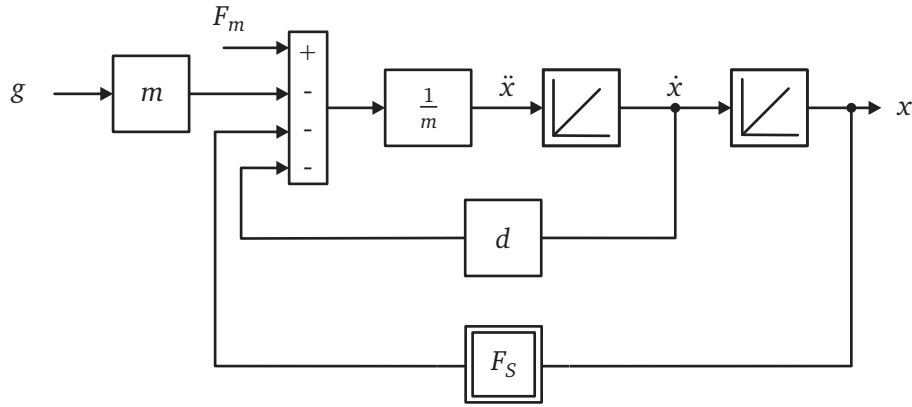
Figure 5.12.: Block diagram of rigid armature motion with magnetic force F_m as input and armature position x as output.

Assuming viscous damping a simple linear damping model is given by

$$F_d(t) = d \cdot \dot{x}(t) \quad \text{with} \quad d > 0. \tag{5.55}$$

Here the damping force is proportional to the armature velocity. The damping constant d is obtained from experiment results as described below. The restoring force of the spring set with n_s membranes exhibits a nonlinear characteristic and is represented by a polynomial of degree 3.

$$F_s(t) = n_s \cdot \left(c_0 + c_1 x(t) + c_2 x^2(t) + c_3 x^3(t) \right) \tag{5.56}$$

The block diagram in Figure 5.12 illustrates the mechanical model of the actuator defined by (5.54). Essential signals are the magnetic force F_m as main input and the armature position and velocity as main output for the simulation.

Spring Stiffness

In order to capture the spring stiffness, the actuator shaft is displaced by an increasing distance covering the entire operating range. Consequently the spring is deflected and generates a restoring force. During the spring design process the resulting force can be simulated for each armature deflection using FEM as described in Section 6.2.4. After the assembly the simulated values are verified by experiments.

The coefficients c_i of the spring characteristics F_s are determined by a least-squares fit. Here n_s denotes the number of membrane springs assembled as a spring package. Experiments confirm a good linearity of the spring force with respect to the amount n_s of springs in the package.

Damping

The actuators are high dynamic devices and realize fast armature motions in typical shaker applications. The membrane springs required for the armature support and the generation of a restoring force also introduce damping into the system during
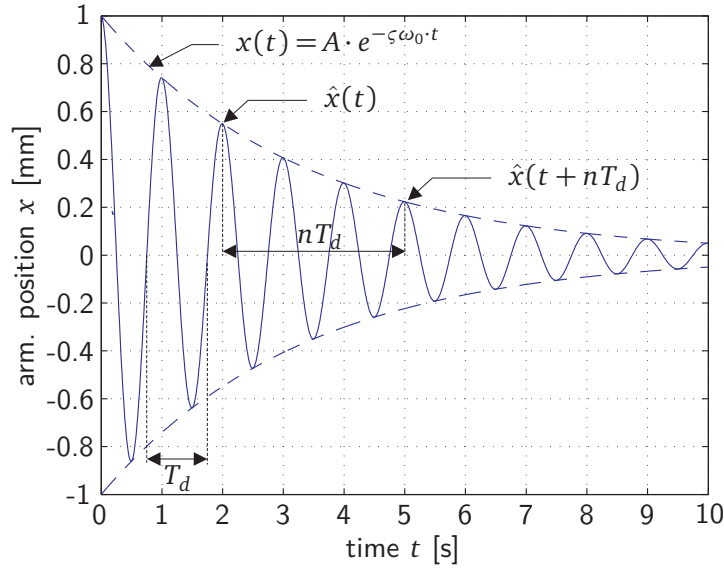
Figure 5.13.: Determination of spring package damping constant. Typical damped oscillation after impulse excitation.

high frequency operation. In the following the damping constant d of the mechanic model (5.55) is determined. For this purpose attenuation experiments are carried out where the armature is excited via an impulse force. To exclude any additional damping effects due to magnetization reversals only the mechanical system is examined. Hence the actuator is assembled without the magnetic core, consisting now only of the casing, membrane springs, pull plates and the armature shaft. This way influences of eddy currents or hysteresis on the damping measurement are avoided. During the measurement, the system is axially excited at the top of the armature shaft with a hammer and the resulting damped armature oscillation is recorded.

A characteristic waveform for this experiment is the sinusoidal function plotted in Figure 5.13. Here T_d denotes the damped oscillation period, $\hat{x}(t)$ the amplitude of armature position x at time t, and $\hat{x}(t + nT_d)$ the amplitude n full periods later. The logarithmic decrement of the considered oscillation is defined by

$$\delta_d = \ln \frac{\hat{x}(t)}{\hat{x}(t + nT_d)}. \tag{5.57}$$

Using the known mass of moving parts m, the damping ratio $\zeta = \frac{d}{2m\omega_0}$ and the natural angular frequency of the undamped system $\omega_0 = \frac{2\pi}{T_d}$ yields:

$$\delta_d = \ln \frac{\hat{x}(t)}{\hat{x}(t + nT_d)} = \ln \frac{A \cdot e^{-\zeta \omega_0 t}}{A \cdot e^{-\zeta \omega_0 (t + nT_d)}} = \ln \frac{1}{e^{-\zeta \omega_0 nT_d}} = n \cdot \zeta \omega_0 T_d = n \cdot \frac{d}{2m} \cdot T_d. \tag{5.58}$$

Finally this equation is rearranged for the damping coefficent:

$$d = \frac{2m}{nT_d} \cdot \delta = \frac{2m}{nT_d} \cdot \ln \frac{\hat{x}(t)}{\hat{x}(t + nT_d)}. \tag{5.59}$$

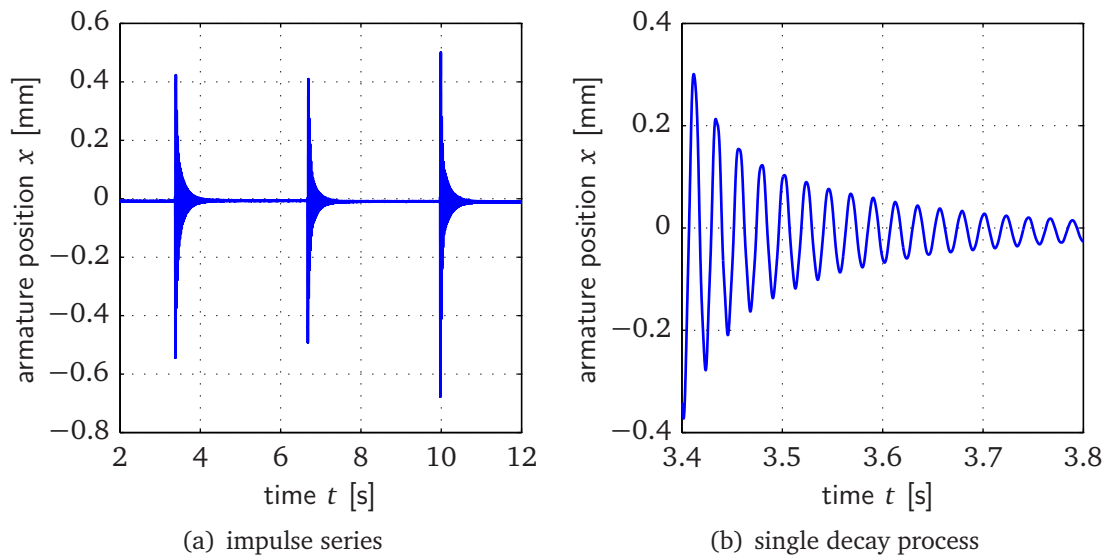(a) impulse series   (b) single decay process

Figure 5.14.: Experimental determination of the damping coefficient for the membrane spring package of the HPS3 actuator.

With the equation above a damping coefficient $d \approx 217\,\mathrm{Ns/m}$ is determined from experimental results. Figure 5.14 illustrates the procedure for the HPS3 actuator. The left side shows an impulse series with three hammer strokes. The right side illustrates a single decay process. The equilibrium position of the oscillation is displaced slightly downwards due to the gravitation influence on the armature mass.

5.5.5. Mechatronic System

From a mechatronic perspective the actuator model consists of the three subsystems electrics, magnetics and mechanics, which are described by (5.48), (5.49), (5.51) and (5.54) respectively. The single subsystems are coupled internally and among each other, forming a closed loop transfer function as illustrated in Figure 5.15. In addition to the actuator itself, the actual technical system includes additional peripherals, which are described in detail in Section 6.3.

Important system parameters such as the coil currents, armature position and acceleration are measured by sensors. A typical signal path includes an analog anti-aliasing filter, followed by an analog to digital converter (ADC), the microprocessor, a pulse width modulation (PWM) unit and finally the power electronics which convert the control signals into the required coil voltage (cf. Figure 6.7). Out of these components only the sensors and the power electronics are included in the simulation model since all other components have only a minor influence in the typical operation range.

In order to obtain realistic simulation results and simplify a subsequent control design, the model allows for the incorporation of sensor noise. The power electronic circuits are not modeled in detail. However, since the maximum coil currents are limited by the power electronics, additional saturation blocks are used in the simulation of the electrical subsystem.
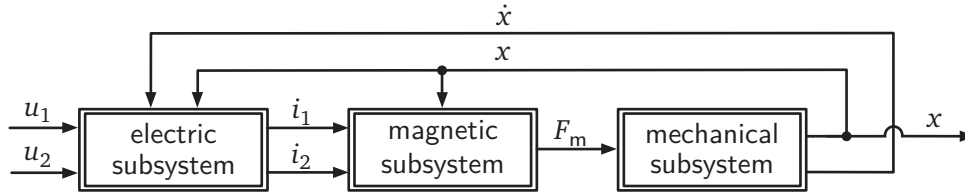
Figure 5.15.: Block diagram for the actuator with three subsystems modeling the electric, magnetic and mechanical domain.

The simulation model is implemented using MATLAB/SIMULINK as described in Section 5.2. The block oriented interface of SIMULINK facilitates the transfer of the developed block diagrams for the actuator and the peripherals. Since the software allows for hierarchical modeling and customized subsystems, the mechatronic approach used for the mathematical model can be maintained for simulation purposes. This way the required implementation time is minimized while the structure of the model and an excellent overview are preserved.

5.6. Outlook: Control

Besides simulation, the co-energy based model can be used for control design. For that purpose, a nonlinear state space model is set up based on the describing equations for the electric subsystem (5.48), (5.49), the magnetic subsystem (5.51) and the mechanical subsystem (5.54). Additionally to the context of this thesis, a proof of concept for a two-degree-of-freedom control structure consisting of a flatness-based feedforward controller and a simple linear feedback controller has been established [31, 107].

The design aims at the trajectory control of the armature position, thereby using the nonlinear state space representation directly or in a linearized version which simplifies the design process considerably. The model-based feedforward unit ensures the basic trajectory tracking while the feedback controller eliminates remaining deviations due to parameter uncertainties and disturbances. For the described actuator modeling, two basic approaches are feasible. If both coils are loaded with equal voltages, the armature position x is used as flat output in a SISO design. If the coils are loaded with individual voltages, a MIMO control design is required; in that case, the armature position x and the coil current i_1 are chosen as outputs.

The resulting feedforward structure is rather complex, if the nonlinear model is used. In that case, a significant computing time reduction is achieved by implementing lookup tables instead of calculating the nonlinear control functions in each time step. During first experiments with an actuator prototype, a good trajectory tracking quality could be achieved at low frequencies ($1 \ldots 10\,\text{Hz}$).

5.7. Chapter Summary

This chapter has given an overview of the co-energy based simulation model developed for both actuators. The method preserves all major advantages of the FE analysis such

as the incorporation of saturation by using the nonlinear B-H curve and the detailed mapping of complex geometries and flux leakage. In particular, the model enables the accurate description of the magnetic force and the inductance as a function of the armature position and coil currents.

In comparison to the numerical analysis, a significant order reduction is achieved by an approximation of discrete co-energy values which are calculated during static FE simulations. The force and inductivity functions for the electromagnetic model are obtained by derivation of the analytical co-energy description. For the curve fitting, polynomials with a low degree are sufficient resulting in a small coefficient matrix. Hence, the co-energy based approach enables the setup of a simulation model which is suitable for dynamic system simulation and control design due to its low computational cost.

Moreover, the simulation is completed by a description of the actuator mechanics. Assuming a rigid armature, a spring-mass-damper model is set up which maps the nonlinear spring characteristic and the damping during high dynamic actuation.

The presented block diagrams of the mechatronic modeling approach can be directly used for the implementation in a system simulation program. Therefore, an accurate analysis of the dynamic behavior of the developed reluctance shakers is possible.

6. Mechatronic Design Aspects

The development of high performance reluctance shakers requires an integrated mechatronic approach. In order to increase the power density and enhance the operating behavior, the consideration of mechanical and information processing issues in addition to the conventional magnetic design is inevitable. This chapter presents key aspects of the mechanical design and the control unit.

Section 6.1 illustrates the setup of the realized prototype device. The associated mechanical design procedure is described in Section 6.2. Important aspects are the consideration of high loads on the actuator components during vibration excitation and the design of a high-strength laminated armature. The integration of membrane springs allows for the compensation of the negative stiffness due to the permanent magnet bias while simultaneously improving the tracking quality.

Finally, Section 6.3 concludes the mechatronic design with a discussion of the information processing system required for the controlled excitation of vibration. This includes the sensor selection and suitable control hardware and software.

6.1. Actuator Design

In Section 4.3.2 the magnetic concept was presented. The realization of the developed design objectives and the transfer of the magnetic circuit concept into a functional prototype is the topic of this section. Mechanical design issues of the individual assemblies are treated in Section 6.2.
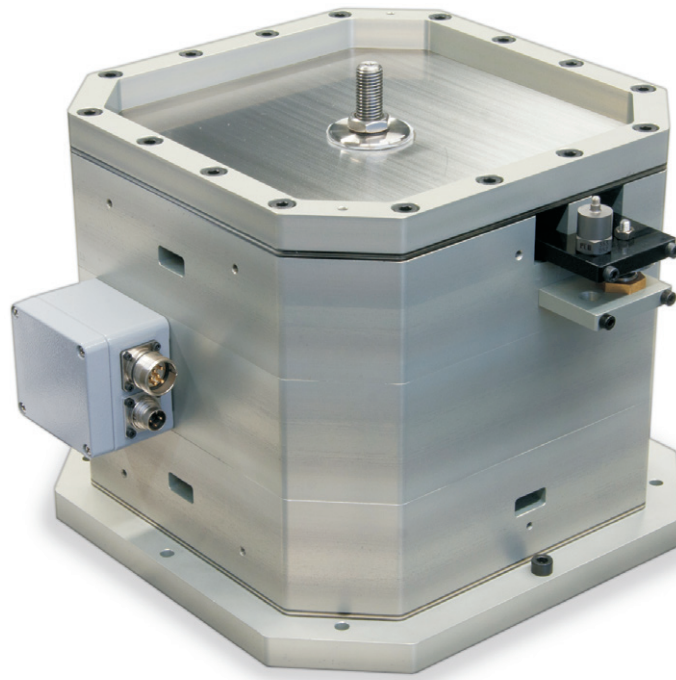
Figure 6.1(a) shows a picture of the realized reluctance actuator HPS3. For the detailed geometric design of all components and the extraction of technical drawings for manufacturing, the 3D CAD system Catia V5 from Dassault Systèmes[1] is used.

The section view of the CAD model in Figure 6.1(b) provides an overview of the actuator design. The mechanical construction is subdivided into six units: core, armature, housing, spring system, sensor system and the electric terminal.
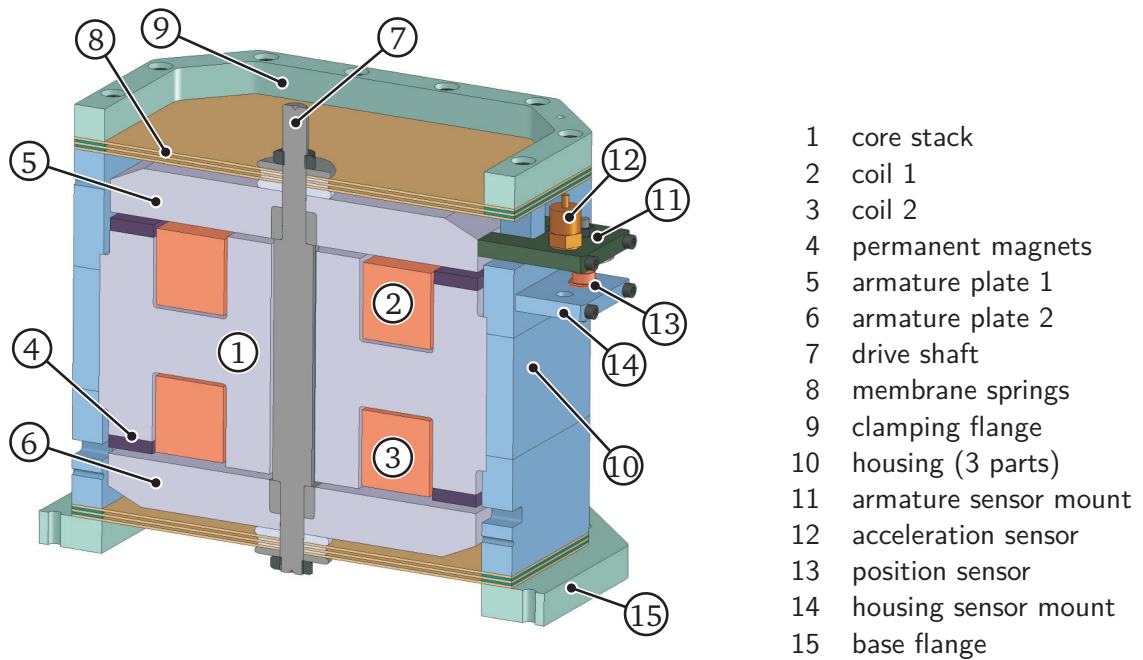
The core is composed of the core lamination stack (1), the coils (2) and (3), and the permanent magnet rows (4). The core is fixed by force closure via the clamping in the housing and rests during operation. Its movable counterpart is the armature, composed of the armature plates (5) and (6) and the shaft (7). During operation in a test rig, the load is directly flange-mounted to the shaft via a thread and an extension rod.

The spring packages (8) at the top and bottom act as shaft bearings in the horizontal plane and provide the required restoring force in vertical direction. The springs are clamped to the shaft and the housing via force closure. The inner bearing point at the shaft is realized using a fixing washer and a nut sitting on the upper shaft thread. The outer fixing is achieved by the screw connection of the clamping flange (9) to the lower

---

1   http://www.3ds.com/

(a) General view of the realized actuator.

1	core stack
2	coil 1
3	coil 2
4	permanent magnets
5	armature plate 1
6	armature plate 2
7	drive shaft
8	membrane springs
9	clamping flange
10	housing (3 parts)
11	armature sensor mount
12	acceleration sensor
13	position sensor
14	housing sensor mount
15	base flange

(b) CAD section view showing the main components.

Figure 6.1.: Permanent magnet reluctance actuator HPS3.

housing parts. The membrane springs realize a functional integration of guidance and suspension for the armature. This is achieved by exploiting the comparatively low axial stiffness for a linear armature displacement. In contrast, the high radial stiffness is used for the centering of the shaft.

The housing (10) receives the flow of forces from the core (1) and membrane springs (9) and transfers it to the base flange (15) where the actuator is mounted to its environment.

A position sensor (13) measures the armature stroke. Since many vibration testing applications require a direct acceleration measurement, an additional acceleration sensor (12) is used. The armature sensor mount (11) is rigidly screwed to the top armature plate and therefore moves with it. In order to enable a stroke measurement it carries the counterpiece for the position sensor (13). In contrast, the housing sensor mount (14) is attached to the housing and made of aluminum. Furthermore, a temperature sensor is embedded in the insulating compound of each coil for heat monitoring purposes. For an improved flexibility and easier calibration process during experiments, the sensor system is led out of the housing. However, the design envelope of the housing is not fully occupied by the armature and core at the chamfered edges. Therefore, the design can be altered to a fully integrated version for the application in industrial test rigs where a better sealing against pollutants and moisture is important.

The electric terminal incorporates the junction for the power supply of both coils and the lead out of the sensor signal cables. A commercial waterproof terminal box (see Figure 6.1(a)) mounted at the housing shields the electric connection from environmental conditions. Again, for industrial purposes the terminal board could be mounted inside the housing. Power and signal cables would then be led out via angular connectors yielding a compact design with a closed housing.

6.2. Mechanical Design Aspects

6.2.1. Core

Figure 6.2(b) illustrates the configuration of the fully assembled core. The core consists of the soft magnetic lamination stack (5), which is equipped with four permanent magnet rows (2) and two racetrack shaped coils (4) and (6). In contrast to the armature it is stationary and thus called stator. Besides housing the core components its mechanical function is the transmission of the magnetic force from the armature to the housing in order to enable the armature movement.

Core Lamination

The soft magnetic core stack is made of silicon iron with 0.35 mm thick laminations (electrical steel M250-35A, see Section 4.4.1). High precision and dimensional stability are necessary since deviations of the pole dimensions directly influence the pole area and particularly the airgap length. Therefore, the single sheets are laser cut, stacked and bonded using a water-dilutable epoxy resin[2] [22, 66], see Section 4.6 for details

---

2   Varnish: DuPont Voltatex E 1175W.

(a) Core lamination stack.

1   core hole
2   permanent magnets
3   limit stop
4   coil 1
5   core lamination
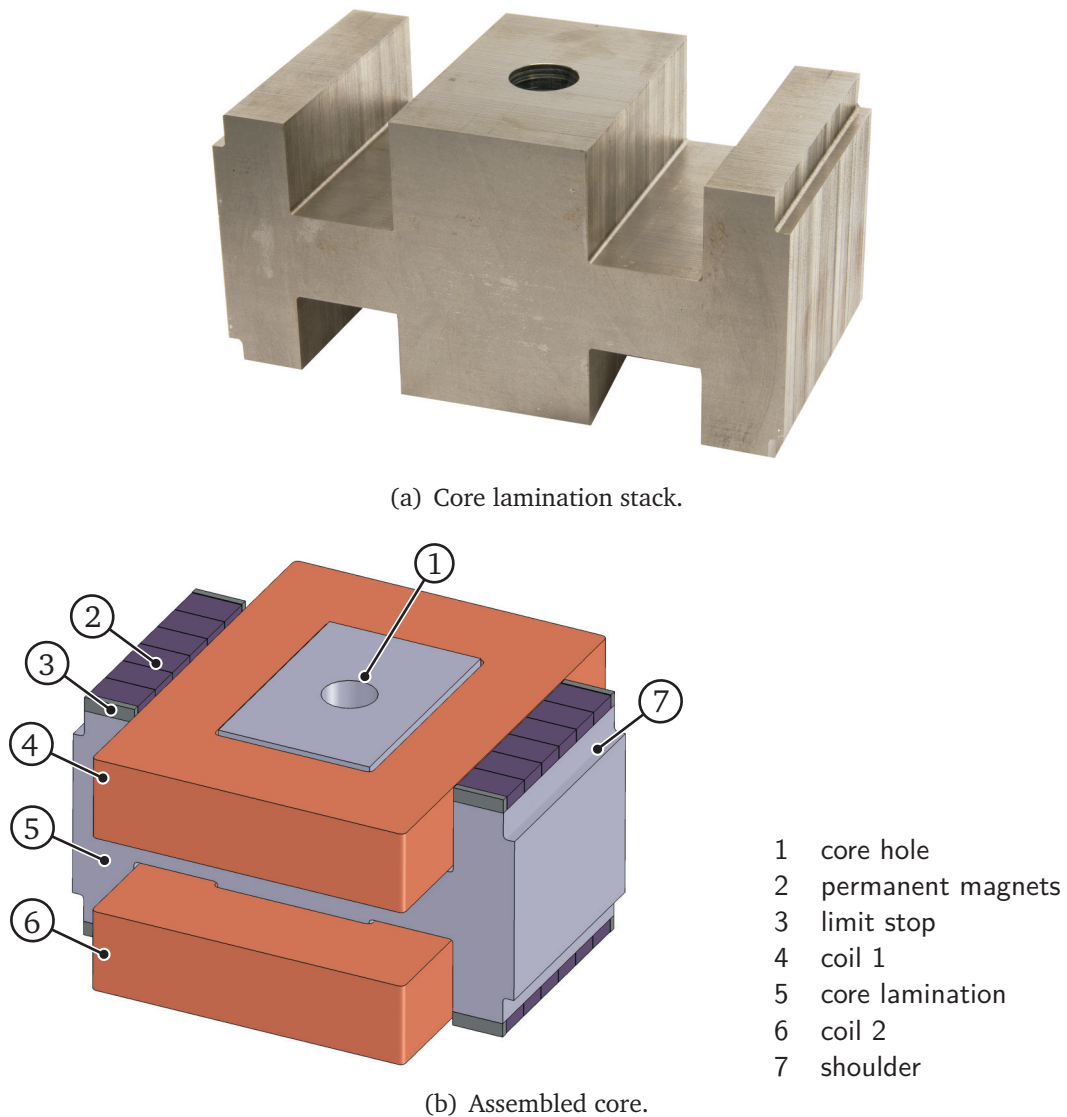6   coil 2
7   shoulder

(b) Assembled core.

Figure 6.2.: Mechanical design of the actuator core.

on the lamination. A picture of the manufactured core stack is shown in Figure 6.2(a). The core has a double E-shape with a total of six legs, providing six pole surfaces for the generation of the required reluctance forces. It carries the permanent magnets on the outer legs, while the coils embrace the inner legs.

During operation the armature may collide with the stator in case of an actuator malfunction or operator misuse. The resulting shock load can damage the permanent magnetic material due to its brittle structure. Therefore, a direct armature impact must be prevented by appropriate design measures. This is achieved in two ways. First, the top and bottom stator teeth in the core center are extended, so that in the case of contact the armature plates impact on the inner stator teeth only. These carry no magnets and are consequently more robust. The additional mechanical clearance inserts a parasitic airgap which reduces the magnetic force. Here, a tradeoff between

excessive force reduction and sufficient safety margin must be found. The safety clearance is thus set to 0.1 mm [88]. However, in the case of armature tilting a contact cannot be completely prevented by this measure only. Therefore, additional limit stops at the end of each magnet row are mounted. For this purpose solid stainless steel blocks are used, whose dimensions are chosen such that the overall height of the inner and outer teeth are equal, see Figure 6.2(b).

For the lead-through of the armature shaft the core features a through bore. Possible burrs from drilling must be removed thoroughly in order to avoid lamination bypasses. The shoulders on each side of the core are intended for the fixation via force fitting in the housing.

Strength Assessment

The core features high stability and stiffness since the force flow is guided in the sheet planes. A major advantage of using surface mounted magnets is the realization of a single core lamination stack. The main loading of the core sheets are the generated magnetic forces, which are distributed to the 371 sheets (core length 130 mm, sheet thickness 0.35 mm). The maximum magnetic force of $F_m = 20$ kN at an armature position of $x = 3.0$ mm results in a force of 54 N per sheet, thus the load on the single bonding areas is reasonably low[3]. Overall, a very rigid core is achieved due to the large sheet surfaces [103], additionally every single sheet is fixed by the housing via the clamping shoulders.

Coils

The rectangular form of the core lamination requires racetrack shaped coils. Due to flexibility and assembly reasons a bonding-varnish coated wire has been chosen, so that the finished coil is comparatively rigid. Based on the calculated value for the wire diameter the next available wire size is selected [19]. The realized coils have a nominal wire diameter of 1.6 mm at $w = 825$ windings. A temperature class H (180 °C) rating ensures a high thermal load capacity.

The coils are casted using a minerally filled, cold-curing 2-component resin based on polyurethane. Main objectives are the thermal connection and the mechanical fixation of the coil material in the core. The coil experiences mechanical loads due to two reasons. First, leakage flux across the coil winding volume leads to the generation of LORENTZ forces on the wires. Second, the actuator core is exposed to the general vibration in the test rig. The chosen resin combines good thermal conductivity with high mechanical strength without being brittle.

Permanent Magnets

The permanent magnets provide the magnetic bias. Due to the magnetic circuit topology they are directly mounted on the pole surfaces of the outer core legs. The magnets are axially magnetized so that the north pole faces the respective airgap. The required magnetic volume is split into smaller magnet blocks. The segmentation

---

3   The shear strength of the used bonding varnish is rated at 19 N/mm², DIN EN 1465 [22].

facilitates the handling during assembly and reduces possible eddy current losses in the magnets. In addition, damaged magnets could be replaced individually. Two limit stops per row shield the magnets from mechanical loads due to armature impacts as described above. For the prototype actuator, the magnets are mounted in an already magnetized state. In order to handle the occurring forces and achieve a satisfying precision, an assembly device is necessary which is described in Appendix A. For the bonding connections, a one component acrylic adhesive is used which yields outstanding shock and peel resistance.

6.2.2. Armature

The armature is the moving counterpart to the stationary core. Figure 6.3 gives an overview of the design. The armature is composed of the shaft (1) and a support structure (2) for the top armature plate (3) and bottom armature plate (4). During the operation in a vibration test rig, specimen are flanged to the shaft via coupling bars.

Shaft

The shaft connects both armature plates and transfers the actuator force to the attached load. It features two shoulders which provide the bearing area for the respective support structure. Two threads on each end allow for the force-closed fixation of the armature plates via countering.
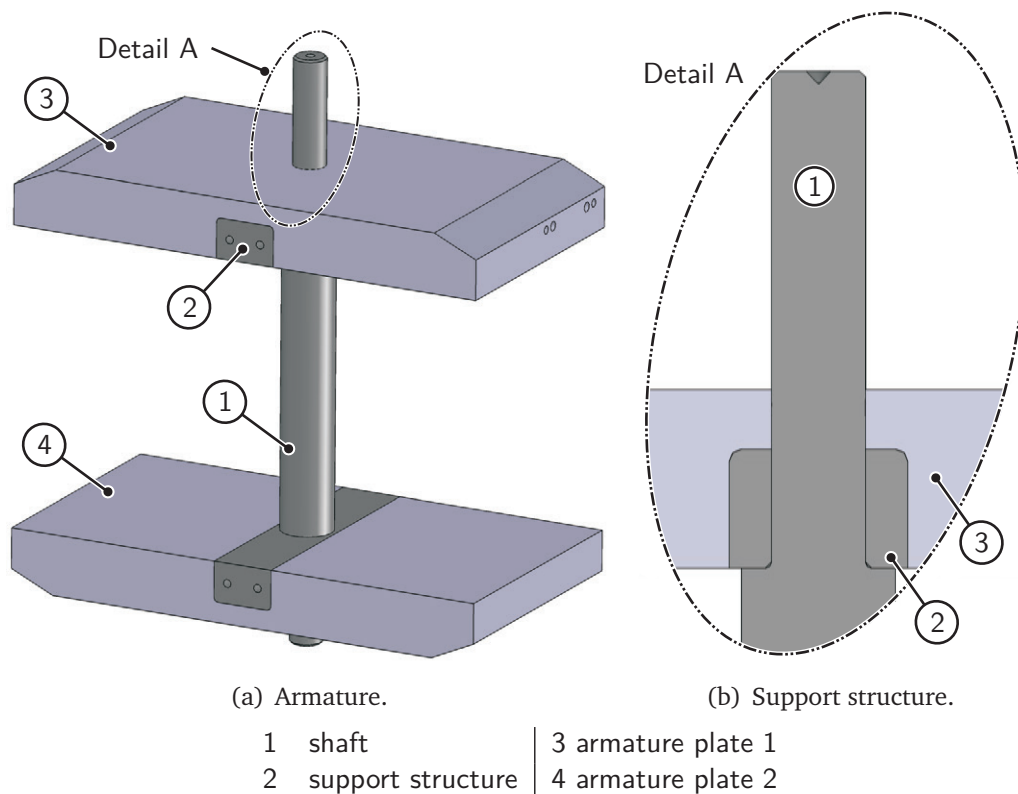

(a) Armature.   (b) Support structure.

| 1 | shaft | 3 armature plate 1 |
| 2 | support structure | 4 armature plate 2 |

Figure 6.3.: Mechanical design of the armature.

The shaft is subject to high stresses during operation and therefore made of stainless steel[4]. The almost nonmagnetic material shows no influence on the magnetic circuit which facilitates both assembly and maintenance.

Armature Plates

The required reluctance force is generated on the pole surfaces of the two armature plates. They have a rectangular shape due to the chosen axial lamination with the sheet planes parallel to the shaft. The edges opposing the pole surfaces are chamfered since the material is magnetically unused in the respective volumes. Both plates feature a groove for the incorporation of the support structure.

The material is silicon iron with 0.35 mm thick laminations[5] which are also used for the core. Again, high precision and particular strength of the laminated stack are required. For manufacturing the same process as for the core is chosen: laser cutting of the single sheets and a bonding varnish based stack.

Due to the axial lamination, a reinforcement of the armature laminations is indispensable. For this purpose a bar serves as support structure for each stack. Every individual lamination sheet sits directly on the supporting structure which is bonded into the armature grove. A high-strength one component adhesive[6], which is suitable for the application in shock and vibration intensive applications, is used. Following this concept the magnetic force pulling on each sheet is directly diverted to the solid steel part of the armature as illustrated in Figure 6.3(b). Therefore, particularly shear loads which pose a threat to the long term stability of the bonded lamination stack are absorbed. Without the bar, only the few sheets sitting on the shaft could transfer their load directly to the solid part. The magnetic force on all other sheets would be transmitted via the adhesive layer between the single sheets.

Due to the high stresses during operation, the support structure is made of stainless steel[4]. The resistance of the bonding is less critical since the bonding area is rather large and the armature is additionally countered on the shaft.

Strength Assessment

The maximum magnetic force of 20 kN at an armature position of $x = 3.0$ mm is distributed to 371 sheets (armature length 130 mm, sheet thickness 0.35 mm), thus the force on each sheet is approximately 54 N. An FEM analysis is carried out in order to assess the behavior of the armature. Figure 6.4 shows the stress distribution and deflection of a single sheet assuming a fixed support at the grove. The resulting maximum stress of 52 N/mm^2 is well below the fatigue limit of the material[7] and allows a safe operation. The armature deflection is reasonably low as well. Influences on the force characteristics due to a reduction of the effective airgap can be neglected.

---

4 X8CrNiS18-9 (EN 10027-2)
5 electrical steel grade M250-35A (EN 10027-1)
6 chemical type: urethane methacrylate
7 The yield strength of the used electrical steel is rated at 425 N/mm^2 [108].
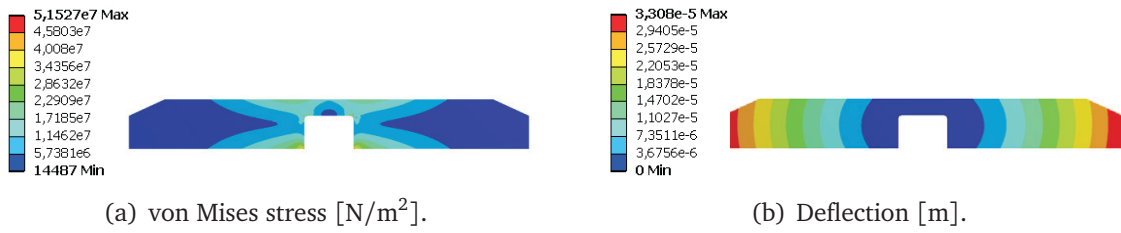
(a) von Mises stress $[\text{N/m}^2]$.

(b) Deflection $[\text{m}]$.

Figure 6.4.: FEM based strength assessment of an armature sheet (magnetic force modeled as distributed surface load, support structure not shown).

6.2.3. Housing

The housing shields the core and armature from the surroundings. It fixes the core and transfers the actuation force from the core to the flange. In order to facilitate manufacturing, assembly and maintenance of the actuator, it is designed in five modular parts, see Figure 6.1(b).

The top part (9) serves as a flange for the upper membrane spring package. The base flange (15) fixes the bottom membrane spring package and enables the flanging of the actuator to its environment. Both flanges are bolted with the three middle parts (10) which fix the core via shoulders and serve as counterpart to the flanges.

The housing has a quadratic footprint. The edges are chamfered since the associated design space is not occupied by the magnetic system. In order to save weight and improve the handling all parts are made of a high-strength aluminum alloy[8]. The fixation of the membrane springs via force closure requires high bolting torques. The use of thread inserts enables maintaining the lightweight construction of the aluminum housing.

For the application in the harsh environment of an industrial test rig, an additional sealing against moisture is required. Particularly problematic are the condensation of climatic chambers and splash from the vehicle underbody.

6.2.4. Membrane Springs

The integration of springs is an essential element of the actuator concept. They provide a restoring force and contribute to the total actuator force in addition to the magnetic forces. In particular, the springs allow for the compensation of the negative magnetic stiffness caused by the permanent magnet bias, thereby enabling a stable actuator operation without feedback control. For this purpose the mechanical spring stiffness F_s/x must be higher than the destabilizing magnetic stiffness F_m/x for all armature positions x.

$$\frac{F_s}{x} \geq \frac{F_m(x,0,0)}{x} \tag{6.1}$$

Since only the force component caused by the permanent magnet flux is relevant, the magnetic force $F_m(x,0,0)$ with zero coil currents $i_1 = i_2 = 0$ must be used for the force

---

8   EN-AW 7075 T651

specification of the mechanical spring.

In addition to the stabilization, the spring force supports the acceleration of the armature at the boundaries of the stroke range during the inversion of the travel direction. Here the attractive force is generated in a relatively large airgap and is therefore weak at the beginning of motion. The performance enhancement of long-stroke solenoids by the use of springs is also described in [67].

The springs considerably improve the operating characteristics of the actuator with respect to its application in vibration test rigs. Within the context of this thesis experiments were carried out in a car test rig with stable and unstable reluctance actuators featuring identical magnetic circuits. It could be shown that the bandwidth and tracking quality of the controlled test rig are conserved when using mechanically stabilized shakers. However, with respect to the application in test rigs the following key advantages are acknowledged [53]:

- Guaranteed stability of the test rig: feedback control can be replaced by a feedforward control concept.

- Simplified testing of different vehicles: model adjustments for the controller design are not required.

- Lower demands on the performance of the control hardware.

- Armature idles in stable central position: simplified docking process.

- Powerless maintaining of the central armature position, lower temperature rise.

Membrane springs are chosen to functionally integrate the generation of spring forces and the armature guiding. In contrast to other spring designs such as screwed pressure springs, the required installation space is low facilitating the design of flat actuators. Further advantages of membrane springs include customizable spring characteristics, a backlash-free operation and very low friction, which make them well suitable for high-precision positioning with small armature displacements [109]. In contrast to roller bearings or plain bearings, problems with stick-slip phenomena which would deteriorate the tracking quality are avoided.

For the spring design an FEM based approach is chosen clamping the membrane at its border and center. The force characteristics are determined by displacing the center and calculating the generated restoring force in the stroke range. The required force curve results from the magnetic force at different armature positions without current feed. Since the restoring force of a single membrane spring is not sufficient, several springs are combined to a spring package. Spacers at the inner and outer clamping avoid friction between the individual membranes. The necessary number of springs results from the acceptable stress level for fatigue strength per spring.

Figure 6.5 illustrates the design and the compensation of the destabilizing magnetic force. In the case of the HPS3 actuator the restoring force is distributed to four springs. For the membranes the spring steel C75S+Qt (1.1248) with a thickness of 1.5 mm is chosen, which offers a tensile strength of 1500-1700 $\mathrm{N/mm^2}$. The stress distribution exhibits a peak around the center clamping of the spring for the maximum armature displacement. The load is adequately low (542 $\mathrm{N/mm^2}$) and indicating a fatigue-proof operation.

(a) von Mises stress $[N/m^2]$.

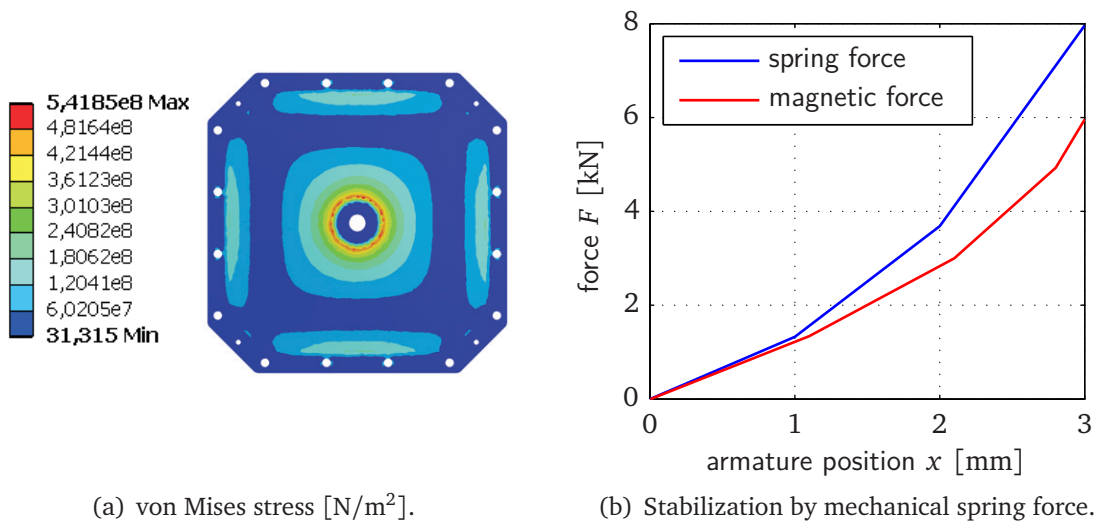(b) Stabilization by mechanical spring force.

Figure 6.5.: HPS3: FEM based strength assessment of a single membrane spring and comparison of magnetic and mechanical force for a set of four springs.

While the design of isotropic membranes for the spring guiding is straightforward, their force characteristic is nonlinear. Notably for large displacements, the destabilizing magnetic force is overcompensated so that the actuator performance decreases unnecessarily as illustrated in the right half of Figure 6.5.

Therefore, the adjustment of the force characteristics by insertion of holes is investigated. For this purpose the magnetic circuit developed in [33] is extended by an improved housing and a stabilizing spring system. A stiff housing and flange combined with thread inserts and high bolting torques (M8 bolts, 20 Nm torque) enables a slip-proof clamping of the membrane springs. The resulting enhanced actuator HPS2 is shown in Figure 6.6(a).
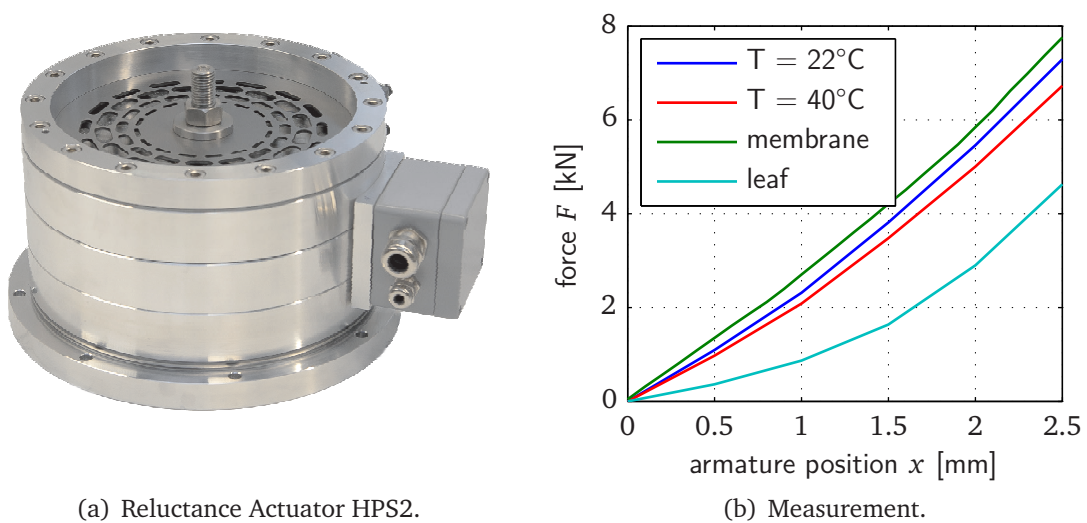

(a) Reluctance Actuator HPS2.

(b) Measurement.

Figure 6.6.: Reluctance Actuator HPS2: Comparison of the magnetic force at two operating temperatures (20 °C, 40 °C) and the spring force (membrane spring set, leaf spring set).

Table 6.1.: Influence of membrane geometry parameters on the spring force components.

parameter	variation	linear force component	cubic force component
membrane thickness	+	+++	+
hole number and area	+	−	−
hole displacement and length	+	0	−

+++ cubic increase, + linear increase, 0 no variation, − linear decrease

The membrane geometry determines the spring characteristic via the thickness, number, area and position of the holes. The membrane thickness contributes cubically to the linear component of the restoring force (coefficient c_1 in (5.56)), but only linearly to the cubic force component (coefficient c_3 in (5.56)). A larger number and area of the holes decreases both the linear and cubic component of the spring force. By displacing and varying the tangential length of the holes, mainly the cubic force component can be influenced as illustrated in Table 6.1. Overall, the described relations are used for a semi-empirical design of the spring characteristics [69].

Figure 6.6(b) compares the magnetic force of the HPS2 actuator at different armature positions with zero coil current and the restoring force of the membrane spring package. To incorporate temperature effects on the permanent magnets, the magnetic force is measured for an operating temperature of 20 °C and 40 °C. The membrane springs compensate the magnetic force of the permanent magnets with a small offset. Therefore, a sufficient stabilization is ensured without force loss through overcompensation as in the case of isotropic membranes. For comparison, the displacement-force diagram of the leaf spring package used in [33] is shown as well. Here, a rather nonlinear characteristic is observable with insufficient spring forces. The destabilizing force of the permanent magnet bias is not compensated.

6.3. Information Processing

In order to enable a controlled excitation of test objects, the actuator hardware must be extended by an information processing system. This includes the selection of sensors, the control unit and the software system. The result is a mechatronic shaker system which allows for the control and observation of the excited vibration.

6.3.1. Sensors

During laboratory experiments and the operation in an industrial vibration test rig, six relevant system states are captured: the temperature and the current of each coil, and the armature position and acceleration. In the following, the measuring principles and sensors are briefly described.

During experiments with car test rigs, up to four actuators are used simultaneously. To guarantee the safe operation of the test rig, a temperature watchdog is implemented in the control program. Furthermore, the coil temperature is used for an additional

Table 6.2.: Sensors for the shaker system.

measured parameter	measuring principle	manufacturer	model	accuracy [%]
temperature	thermistor	EPCOS	G350	$< \pm 5$
current	hall effect	LEM	HX03-P	$< \pm 1$
position	eddy current	Micro-Epsilon Messtechnik	eddyNCDT 3010 - U6	0.005
acceleration	piezoelectric	PCB Piezotronics	353B52	± 5

evaluation of the coil resistance during the simulation model validation. The temperature in the windings is mainly measured due to safety reasons. This allows for the implementation of an emergency shutdown in the case of an improper temperature rise which can damage the casting compound. Temperature rises can be the result of high currents caused by undetected malfunctions of the control software.

Small size and robust design are the main requirements on the temperature sensors. Therefore, glass-encapsulated thermistors are used. Each coil is equipped with one sensor which is placed in the embodying cast resin. The sensors are embedded during the grouting of the resin.

The current sensors are integrated into the power electronic boards of the power supply. The current in each coil is measured individually with a standard hall-effect based sensor.

The armature state is measured both in the form of armature position and acceleration. The position sensor is essential due to the airgap-dependency of important system parameters such as the magnetic force and inductivity. Furthermore, measuring the armature position allows for the observance of a minimal safety airgap (0.5 mm) which prevents damages caused by an armature impact on the stator. An eddy-current based sensor is chosen. In order to protect the sensor from inevitable shocks and the constant vibration of the armature, it is attached to the housing and thus stationary. The required metal counterpart, in which the eddy currents are generated by the measurement system, is mounted on the moving armature. This setup enables a noncontacting, wearless and maintenance-free measurement. Therefore, the concept is well suited for industrial purposes. During experiments in the lab a high-resolution sensor is used. However, for most industrial applications such as car test rigs, a simple inductance based sensor, as used in factory automation, is sufficient.

Recording the armature acceleration is not necessarily required for a safe actuator operation. However, many NVH testing situations are based on the replication of given acceleration data. The additional sensor allows for a straightforward comparison of the tracking quality during experiments. Furthermore, the acceleration sensor can also be removed from the armature and placed directly on the load. This enables the application of iterative-learning based control concepts, thereby ensuring high local tracking qualities [53]. Table 6.2 summarizes important sensor features.

Prior to the analog-digital conversion, all sensor signals are low-pass filtered. For this purpose analog electronic Butterworth filters of fourth order are used. The cutoff frequency is adjusted to 400 Hz, which ensures proper anti-aliasing without
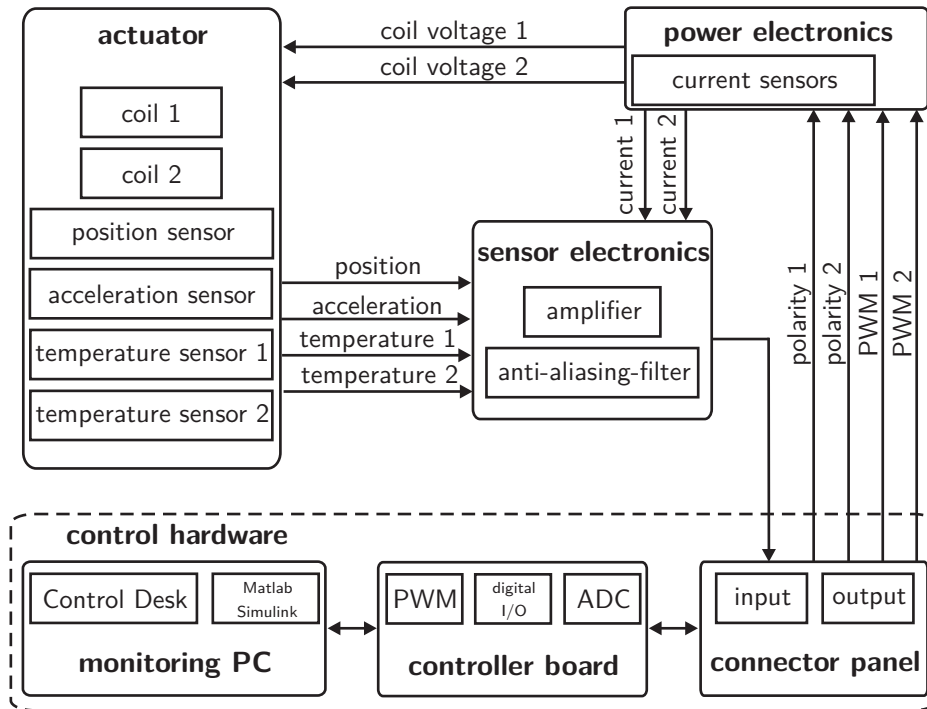
Figure 6.7.: Overview of the information processing system.

interfering with the maximum actuation frequency range of 100 Hz. Figure 6.7 shows the incorporation of the sensor system into the overall information processing concept.

6.3.2. Control Unit

The control unit allows for the operation of the actuator and the monitoring of experiments. A DS1104 R&D system by DSPACE [20] is chosen. The control unit consists of three major components: a monitoring PC, the real-time controller board and a connector panel. Figure 6.7 illustrates the integration of the control hardware into the information processing concept. The standardized hardware allows for convenient programming and debugging and therefore increases the flexibility in a laboratory environment. For industrial applications though, the control unit can be replaced by digital signal processor (DSP) modules. In that case a system integration of control electronics and power electronics is feasible, which leads to a one component operation module and enables the realization of a stand-alone solution for single actuator component test rigs as well as a modular design of car test rigs with several actuators.

Control algorithms and programs are designed on the monitoring computer. It serves as human interface for user inputs and the visualization of operating data. Furthermore, it allows for the evaluation and storage of measurement data.

The data acquisition, control algorithms and signal processing run on the DS1104 controller board in real time with a sampling rate of 10 kHz. Six ADC channels allow for the digitization of analog measuring signals, see Section 6.3.1. An onboard slave DSP subsystem provides four programmable one-phase PWM outputs, which are used

Table 6.3.: Key features of the dSpace DS1104 control unit hardware [20].

processor	MPC8240 processor with PPC603e core
	64-bit floating point processor
	250 MHz CPU
memory	global memory 32 MB SDRAM
	flash memory 8 MB
slave DSP subsystem	Texas Instruments TMS320F240 DSP
	16-bit fixed-point processor
	20 MHz
	4 × 1-phase PWM output
ADC	4 muxed channels equipped with one 16-bit sample & hold ADC
	4 channels each equipped with one 12-bit sample & hold ADC
	±10 V input voltage range each
digital I/0	20-bit parallel I/O
	single bit selectable for input or output

for the generation of the required PWM signals. The power electronic boards, which supply the voltage for each coil, are directly driven by two pulse-width modulation (PWM) signals. The voltage polarity is transmitted to the power electronics by means of the 20-bit digital I/O port. Here, two bits are selected as output and encode the voltage sign. Table 6.3 holds the relevant hardware aspects of the controller board.

A connector panel (CLP1104 from DSPACE) serves as interface between the controller board and the power electronics and sensors. The connector panel obtains access to the I/O signals of the controller board via a 100-pin KEL connector. The physical interface for driving the power electronics is the digital I/0 and the PWM port. Here two D-sub connectors are provided. The amplifier electronics of the sensors are connected via standard BNC connectors. All signal processing is executed on the controller board whereas the connector board serves as pure interface.

6.3.3. Software

The monitoring PC runs the operating system WINDOWS XP by MICROSOFT. For the operation of the actuator and the test rigs the software package CONTROLDESK from DSPACE[9] is used that allows for a fast and simple creation of user interfaces. Furthermore, the combination with MATLAB/SIMULINK from MATHWORKS[10] enables the fast generation of operating and control structures in block-diagram form. These are compiled with the REAL-TIME WORKSHOP from MATHWORKS and downloaded to the real-time hardware DS1104, where the execution at runtime occurs. Therefore, the user is freed from the burden of low-level programming. In the following, the relevant tools of both software packages are briefly described.

The REAL-TIME INTERFACE (RTI) from DSPACE provides graphical blocks that implement the physical I/O capabilities of the DS1104 system in the SIMULINK model [21].

---

9   http://www.dspace.com/
10 http://www.mathworks.com/

Furthermore, it extends the REAL-TIME WORKSHOP and enables the automated code generation. The automated conversion of MATLAB/SIMULINK models to compiled programs running on DSPACE real-time hardware shortens the development and coding time considerably. Model changes can be carried out efficiently and without major implementation effort.

For the fundamental code generation, the REAL-TIME WORKSHOP is employed. It allows the generation of C-code which is used for the rapid prototyping of control algorithms.

The graphical user interfaces, the visualization of measurement data and the control of experiments are implemented using CONTROLDESK. The program enables a straightforward creation of layouts and instruments by graphical programming. Furthermore, the project and experiment management are tightly integrated allowing for an efficient administration of all experiment files. The standard user interface includes control items for the start and termination of experiments as well as for the selection of different control modes. Both voltages and acceleration profiles can be selected as commands. A function generator is used for the generation of input voltage profiles. Different acceleration profiles (drive files) can be loaded via a selection dialog. The activation of a feedback control system allows for the tracking of these commands. Plotters or digital displays visualize the measured data, which typically includes the armature position, the armature acceleration, the coil currents and the coil temperatures.

The underlying control and operating algorithms are implemented as block diagrams in SIMULINK. For an increased flexibility these are fully parameterized and initialized by MATLAB M-files. The necessary software-hardware interface is realized using the I/O blocks from the RTI library.

The MLIB/MTRACE library of DSPACE facilitates the automation of the measuring process. It allows for the control of data capturing and the specification of trace variables under the control of M-files. Further important features for the automation of experiments include online parameter tuning and the transmission of test profiles to the real-time application at runtime. The results can be directly monitored on the user interface, while the measurement data is sent to the MATLAB workspace for further processing and storage [21].

6.4. Chapter Summary

This chapter has presented the implementation of the magnetic concept into the prototype reluctance shaker HPS3. Besides mechanical design aspects, the required sensor system and the control unit have been described.

The flux carrying parts of the HPS3 actuator are made of silicon iron with 0.35 mm thick laminations (electrical steel M250-35A). While this is beneficial for the reduction of eddy currents, the mechanical setup is more complex requiring an assessment of the loads during operation and a special support structure for the moving armature. In order to maximize the stiffness, robustness and precision of the laminated parts, the single sheets are laser cut and bonded to a stack with the bonding varnish technology. Due to the axial lamination and the high magnetic forces of maximum 20 kN, the

armature is reinforced by a support structure. Direct shear loads on the sheets are avoided by a steel bar bonded into each armature plate. The core has a double E-shape with a total of six teeth. It features surface mounted permanent magnets which are protected from armature impacts by steel limit stops and extended inner teeth. Furthermore, the axial lamination requires race-track shaped coils which are cast into the core.

The magnetic system is further extended by a membrane spring system which provides both the guiding for the armature and a restoring force which compensates the negative magnetic stiffness. This approach enables a stick-slip free motion at high frequencies and a stable actuator operation without feedback control. The springs are designed using a FE based calculation of the generated restoring forces. The setup employs a total of four 1.5 mm thick isotropic membranes divided into two spring packages.

Furthermore, designing the spring characteristic for a better compensation of the negative magnetic stiffness is investigated with a second prototype (reluctance shaker HPS2). For this purpose, an existing magnetic system from previous research is extended by a spring system with inserted holes. A semi-empirical approach enables the adjustment of the spring characteristic via the membrane thickness and the number, area and position of the holes.

Finally, an overview of the information processing system is given. It extends the actuator hardware to a mechatronic shaker system and enables the control of the excited vibration.

7. Experimental Results

The previous chapters presented the systematic development of magnetic reluctance shakers based on the demands of the respective testing situation. In the following, selected results from the experimental investigation of both realized prototypes HPS2 and HPS3 are presented. The measurements serve as basis for the validation of the proposed design approach and the simulation models. Furthermore, the experiments in a laboratory environment are the preliminary stage for the actuator application in car test rigs. For the force measurement a test rig is established, which allows for the adjustment of coil currents and armature position. During the experiments, two different setups are used:

- *fixed armature*: stationary armature position ($\dot{x} = 0$), voltage or current command, stationary or time-varying input signals

- *moving armature*: varying armature position ($\dot{x} \neq 0$), voltage command, time-varying input signals.

This approach allows for the measurement of both the static and the dynamic actuator characteristics.

7.1. Static Performance

This section describes the experimental results with a fixed armature. Particularly the measuring of static force diagrams allows for a first characterization of the actuator properties and an evaluation of the design described in Chapter 4. The generated reluctance force depends on the coil currents and the armature position, which determines the airgap length, see (3.15). In order to obtain a full force characteristic, both the coil currents and the armature position have to be varied during the experiment.

7.1.1. Force Test Rig

The challenges with respect to the static force measurement are mainly due to the high magnetic forces and the need for a defined armature displacement. Instead of designing a special force measurement test rig, in the following a commercial materials testing machine is modified and adapted for the static experiments [35, 121].

Requirements

The test rig must allow for the measurement of the static actuator force in dependency of the armature position and the coil currents. The force sensor range must be at least $\pm\, 20\,\text{kN}$, which is the maximum static actuator force at the boundaries of the stroke

Table 7.1.: Requirements for the force test rig.

parameter	range	description
functional requirements		
force measurement	$> 20\,\text{kN}$	max. static actuator force
travel range	$> 7\,\text{mm}$	max. actuator stroke 7 mm
travel speed	$> 1\,\text{mm/min}$	covering stroke range in acceptable time
deformation in force direction	$< 0.05\,\text{mm}$	preferably constant armature position
available test space		
height	$> 400\,\text{mm}$	overall actuator height
overall width	$> 350\,\text{mm}$	actuator width
other requirements		
flexibility		experiments with different actuators
measurement automation		minimize required time for experiments
interfaces		digital processing of all measuring signals

range. The actuators are already equipped with sensors for the armature position and the coil currents, therefore no additional sensors are required. However, the setup must enable defined stationary currents. The minimum travel range of the test rig results from the specified actuator stroke range of 7 mm. The armature position must be accurately positioned and held in this range. For this purpose the test rig deformation in force direction should be small. A minimum travel velocity of the fixed armature is required in order to cover the stroke range in a feasible time. Furthermore, the integration of the actuator into the test rig sets space requirements which are determined by the overall actuator dimensions.

Additional demands result from the necessary flexibility during experiments. Measurements with different actuators should be realizable. Therefore, the mechanical setup should be easily reconfigurable. An important feature is the automation of experiments, which allows for the capturing of a high amount of measurement points in acceptable time. Finally, the experiments should be monitored using the existing information processing system of the actuator, cf. Section 6.3. All signals are transmitted to the monitoring computer and processed. Table 7.1 holds an overview of the properties of the test rig.

Test Rig Concept

The exact force measurement poses high demands on the design of the test rig particularly with respect to stiffness and positioning accuracy. However, static materials testing machines are designed for a similar purpose and thus fulfill all requirements on the actuator force measurement.

Figure 7.1 shows the experimental setup with the materials testing machine[1] INSTRON 4482 of INSTRON DEUTSCHLAND GMBH[2]. The machine is designed for static force measurements up to 100 kN. The force sensor is located on a movable crosshead,

---

1 The test rig was made available by the INSTITUTE OF LIGHTWEIGHT STRUCTURES, TUM.
2 http://www.instron.de/
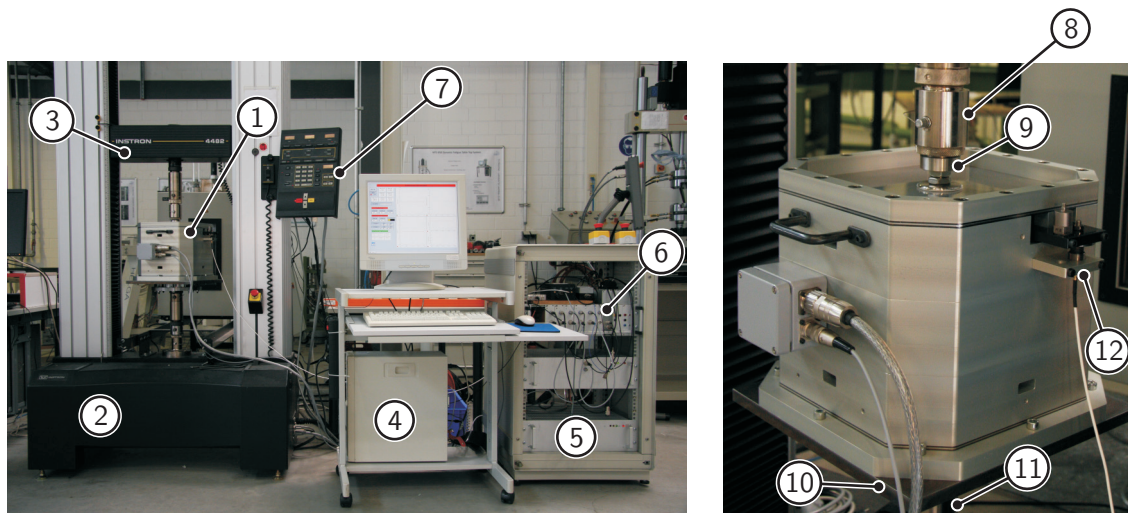
1	HPS3 actuator	5	power electronics	9	top flange
2	force test rig	6	sensor electronics	10	bottom flange
3	crosshead	7	operating panel test rig	11	holding fixture
4	monitoring PC	8	adaptor	12	position sensor

Figure 7.1.: Static force measurement test rig with the HPS3 actuator.

which is actuated by ball screws. The two columns are connected via a top plate and base beam. They provide the guiding for the crosshead. The overall assembly sits on a solid base structure.

A custom-made adapter connects the actuator shaft with the crosshead. In order to achieve a zero-backlash setup, the connection is secured with lock nuts. The actuator itself is screwed to a custom-made bottom flange, which sits on the base adaptor of the testing machine. All adaptors are made of steel due to the high loading during the experiments.

The machine is equipped with an incremental range sensor, which is used for the positioning of the traverse. Both the force and the position signal of the machine are captured in addition to the standard actuator signals. The measurement procedures are automatized using the full information processing capability of the dSpace system. This allows for a fast and efficient execution of the experiments.

7.1.2. Measurements

The static measurements aim at the determination of the actuator parameters as a function $f(x, i_1, i_2)$ of the armature position x and the coil currents i_1, i_2. In the following the measurement procedure is described, which is implemented in the control software.

The procedure starts with the initialization of the software and the test rig. The actuator is calibrated, i.e. the armature is moved to the physical center between both limits. Afterwards all working airgaps are of equal length. The control algorithm consists of three nested loops which adjust the armature position and both coil currents. The actual measurement process starts with the positioning of the armature by traversing
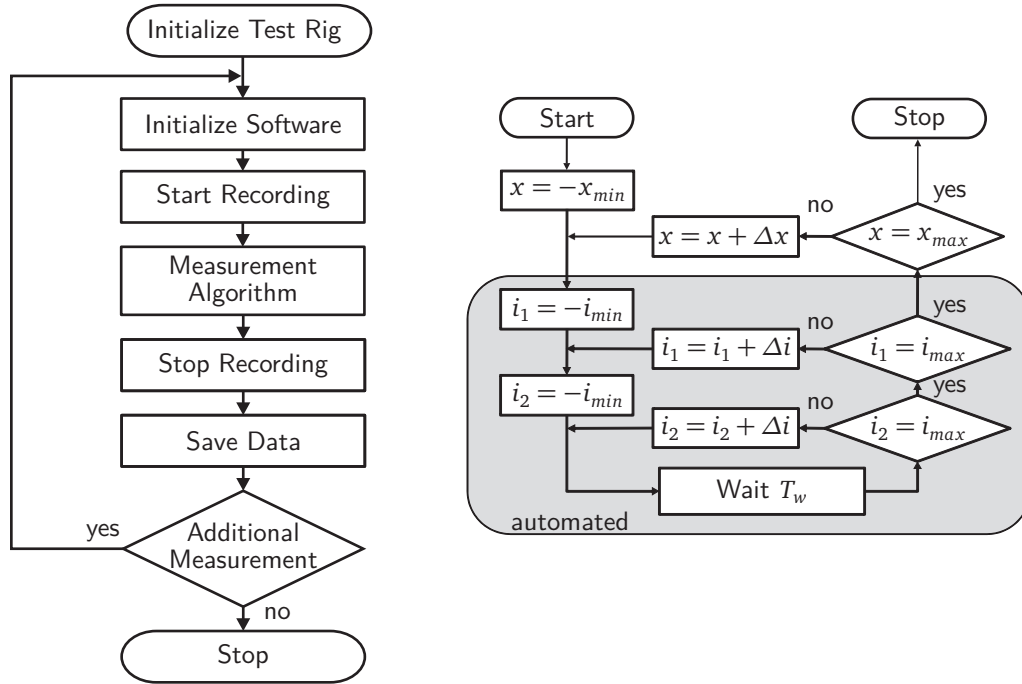
Figure 7.2.: Measurement procedure (left) and algorithm (right).

the crosshead of the testing machine. The measuring algorithm cycles through the current loops before moving the armature again as illustrated in Figure 7.2. The currents are adjusted using a simple PI controller. A voltage command alone would not be sufficient due to the temperature rise in the coils during the experiment. A short holding time is integrated, which ensures the settlement of the current to its final value. The time lag is chosen to be $T_w = 5\tau$, which corresponds to 99.3 % of the final current value.

In Figure 7.3 the measured force of the HPS2 actuator is compared to the simulation results of the co-energy based model for the case of equal coil currents $i_1 = i_2$. The actuator force $F(x, i_1, i_2)$ shows the typical nonlinear characteristic due to saturation and the influence of the armature position. The absolute peak force varies between 6 kN in central armature position and 12 kN at the boundary of the stroke range. The simulation with the co-energy based model yields a good agreement with the measurement in the entire operating range and maps the nonlinearity very well. This confirms the advantage compared to the linear MEC model, where a good fit is restricted to the center of the operating range while the simulation error is larger at the boundaries [118].

Figure 7.4 shows the measured force-current characteristics of the HPS3 actuator. The generated maximum force value in central armature position $x = 0$ mm is 5 kN with a coil current of $i_1 = i_2 = 5$ A which results in a static force-current factor $k_{Fi} = 1$ kN/A. Due to the different coil design, this force output is achieved with a lower magnetomotive force ($\Theta_{HPS3} = 4125$ A vs. $\Theta_{HPS2} = 5800$ A). As discussed in Chapter 2, the obtained force values are sufficient for a realistic road simulation in vibration test rigs. At the time of writing the maximum output currents of the power electronics are restricted to 5 A. However, a redesign for the rated coil current of 8 A would increase
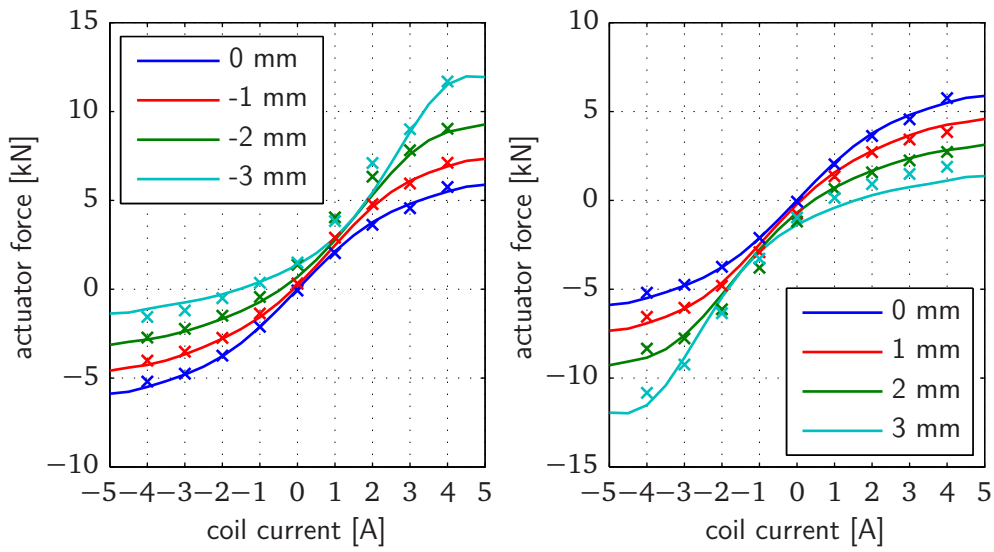
Figure 7.3.: Reluctance actuator HPS2: Comparison of measurement [×] and co-energy based model [—]. Equal currents in both coils.
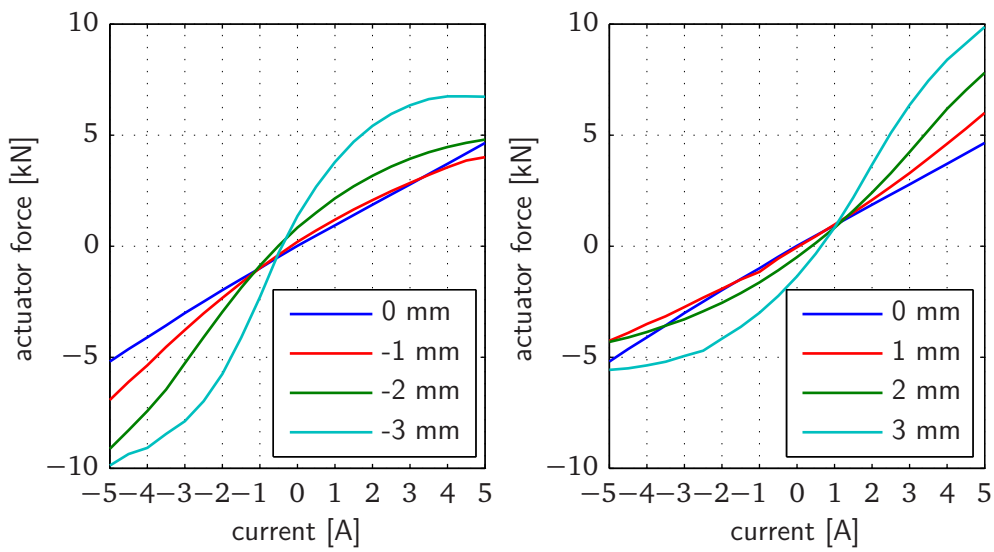

Figure 7.4.: Measured force-current characteristics of the HPS3 actuator. Equal currents in both coils.
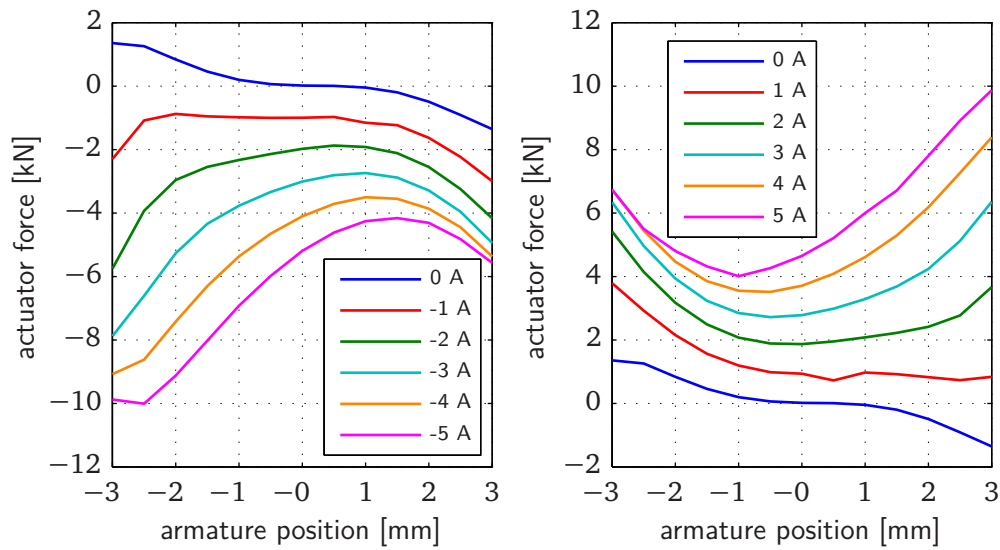
Figure 7.5.: Measured force-position characteristics of the HPS3 actuator. Equal currents in both coils.

the obtainable force considerably, so that the predicted peak force of $8\,\text{kN}$ for zero armature displacement can be achieved (see Figure 4.16).

The force-current characteristic in the central armature position $x = 0\,\text{mm}$ is linear, since the magnetic circuit is not saturated for this armature position. However, for large armature displacements the force generation is nonlinear due to the influence of saturation and the partial overcompensation of the permanent magnet flux. The lower force increase caused by saturation is visible in Figure 7.4 for the operating points $(x = -3\,\text{mm}, i = -5\,\text{A})$ and $(x = 3\,\text{mm}, i = 5\,\text{A})$. In contrast, for the operating points $(x = -3\,\text{mm}, i = 5\,\text{A})$ and $(x = 3\,\text{mm}, i = -5\,\text{A})$ the permanent magnet flux is overcompensated and the flux minimum in the smaller of both working airgaps is exceeded. As a consequence, the respective airgap is subject to more flux and contributes a higher magnetic force than desired. Therefore the total magnetic force $F_m = F_{m2} - F_{m1}$, which results from both airgaps, cannot be further increased at those points.

The force-position characteristics are illustrated in Figure 7.5. The typical nonlinear force generation of reluctance actuators is clearly observable. Since the force depends on the inverse square of the airgap length, a displacement of the armature leads to a considerable force variation even if the coil currents are kept constant. The superposition of spring stiffness and negative magnetic stiffness of the permanent magnets is observable for the case of current-less coils $i_1 = i_2 = 0\,\text{A}$. The stabilization produces a positive force for negative displacements and vice versa which moves the armature back to its central position $x = 0\,\text{mm}$.

7.2. Dynamic Performance

For the determination of the static performance the armature is fixed during the measurements and the armature position kept constant. This facilitates the force

measurement at different operating points. However, in the normal operating mode for vibration excitation the armature is oscillating. In that case a voltage command is applied to the coils, which is converted by the actuator into a motion.

The experiments in this section aim at the determination of the operating characteristics and the evaluation of the dynamic simulation model developed in Chapter 5. The measurements are carried out with the HPS2 and HPS3 actuator without attached loads. Since the actuators are stable, no additional feedback control for trajectory tracking is applied. For all experiments a sinusoidal input voltage is chosen. The measured armature position shows a small constant position deviation due to the gravitational influence on its own mass.

Figure 7.6 shows the position trajectory and the coil currents of the HPS2 actuator for different frequencies. In order to evaluate the influence of the eddy-current filters derived in Section 5.5.3, simulation results of the nonlinear model are compared to measurements with the prototype device. For the lower frequency 3 Hz (left side) the peak armature position is at 2 mm. Similar to the static case, there is a good match between simulation and experiment even for large armature displacements. For the higher frequency 10 Hz on the right side, the positive influence of the eddy current modeling is observable. Without eddy current modeling both the amplitude and phase of the simulated current trajectories show deviations from the measured values, while the incorporation of the eddy current filter yields an overall good match for all trajectories.

The influence of eddy currents in the solid magnetic core of the HPS2 actuator becomes more obvious for higher frequencies as illustrated in Figure 7.7. Without eddy current modeling the simulated coil currents are considerably lower than the measured values. An explanation for the differences can be found in the inductivity decrease due to eddy current influence. The lower inductivity causes a faster current rise to higher values. If the eddy current filter is used in the simulation, the deviations are small so that a satisfying result is obtained. The small phase delay is mainly due to the simplified first-order model for the filter which causes a phase delay of -90° for higher frequencies whereas the real phase shift is only -45° as discussed in [25, 124].

Figure 7.8 illustrates the validation of the simulation model of the HPS3 actuator for a 1 Hz and 10 Hz oscillation. In both cases the shape of the simulated and measured trajectories are similar. For the higher frequency 10 Hz a deviation particularly in the simulated current values is observed. This is due to the model parameters of the mechanical system. Particularly the membrane springs have a great influence on the overall actuator performance so that the simulation results are very sensitive to changes in the stiffness and damping of the spring system. Furthermore, both the measured and simulated coil current values are lower compared to the 1 Hz oscillation. At 10 Hz the system operates closer to the resonance frequency of the mechanical spring system. Here, a small excitation by the electromagnetic subsystem is sufficient for achieving large armature position amplitudes.

An oscillation at 40 Hz is shown in Figure 7.9. Simulation and experiment match particularly well for the armature trajectory. The comparison to the results for the HPS2 actuator demonstrates the efficient eddy current reduction of the fully laminated magnetic core, so that no phase delays are measured. First experiments at higher frequencies indicate a likewise satisfying prediction of the position and current
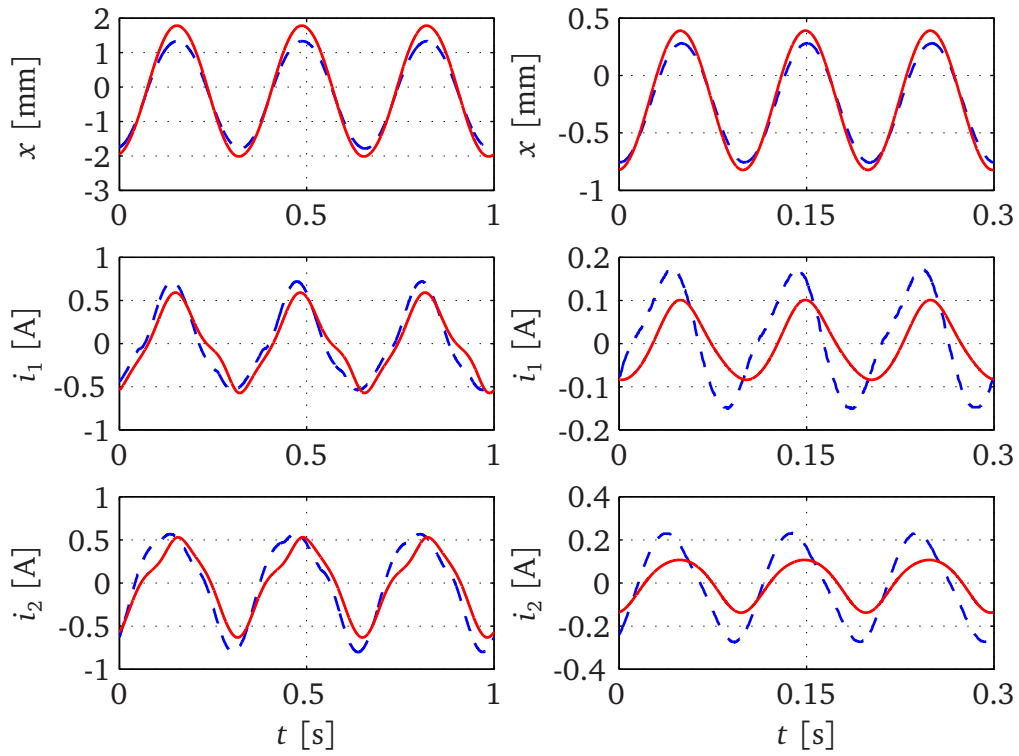
(a) Simulation without eddy current model.
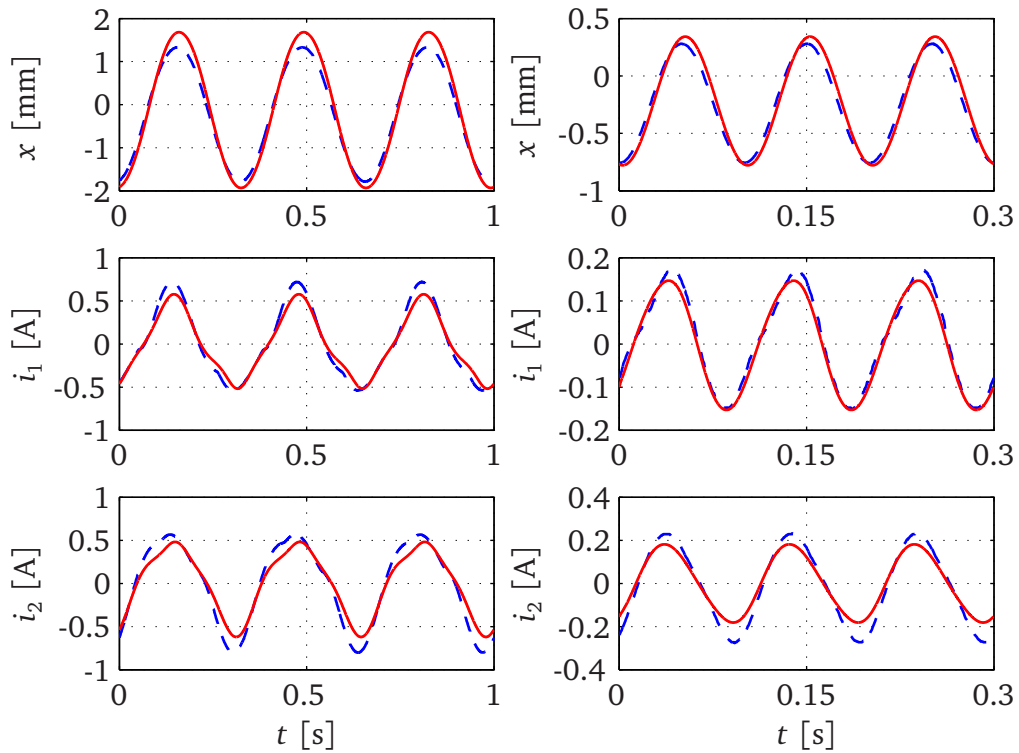
(b) Simulation with eddy current model.

Figure 7.6.: Reluctance actuator HPS2: Position and current trajectories for a 3 Hz (left) and 10 Hz (right) oscillation. Comparison of simulation [—] and experiment [– –].
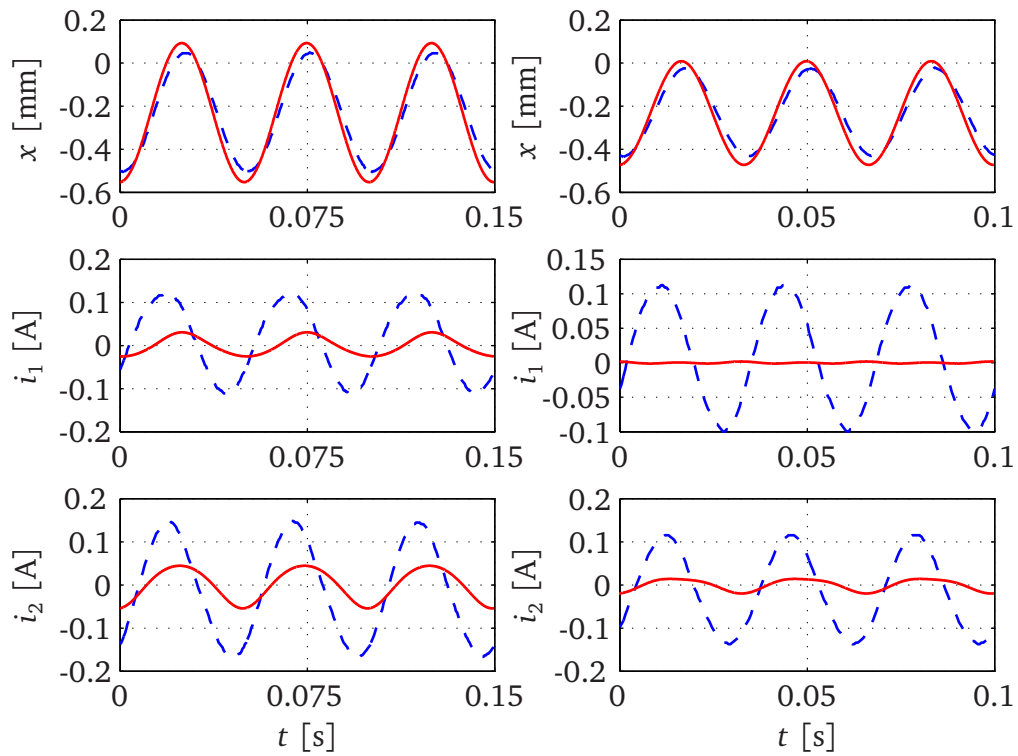
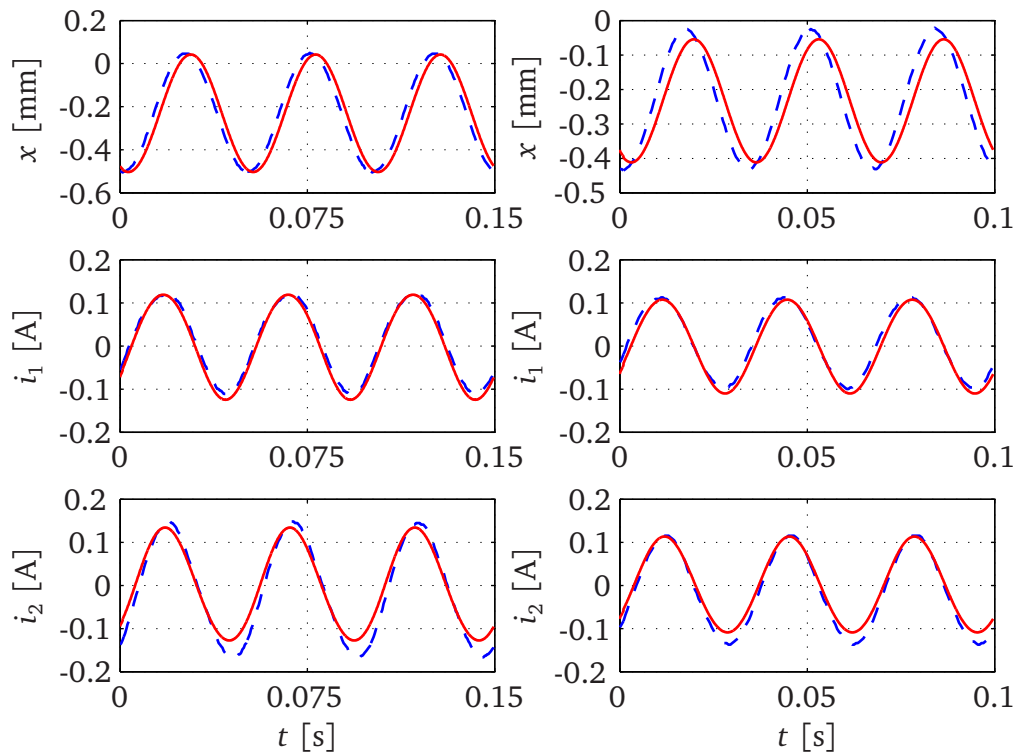(a) Simulation without eddy current model.

(b) Simulation with eddy current model.

Figure 7.7.: Reluctance actuator HPS2: Position and current trajectories for a 20 Hz (left) and 30 Hz (right) oscillation. Comparison of simulation [—] and experiment [– –].
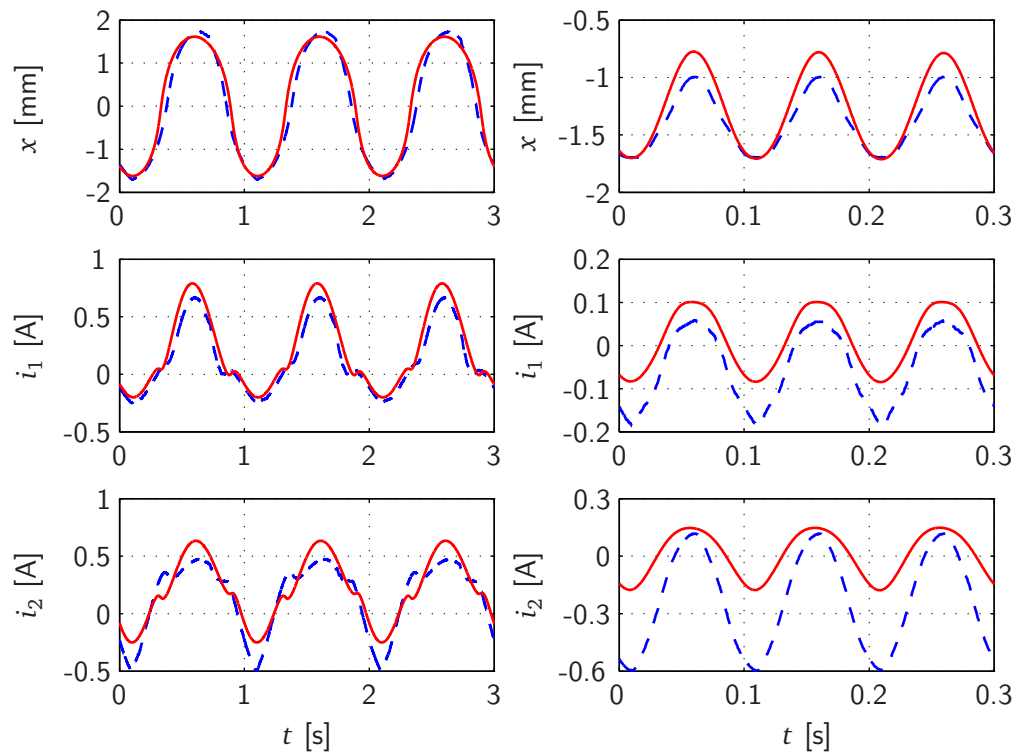
Figure 7.8.: Reluctance actuator HPS3: Position and current trajectories for a 1 Hz (left) and 10 Hz (right) oscillation. Comparison of simulation [—] and experiment [– –].
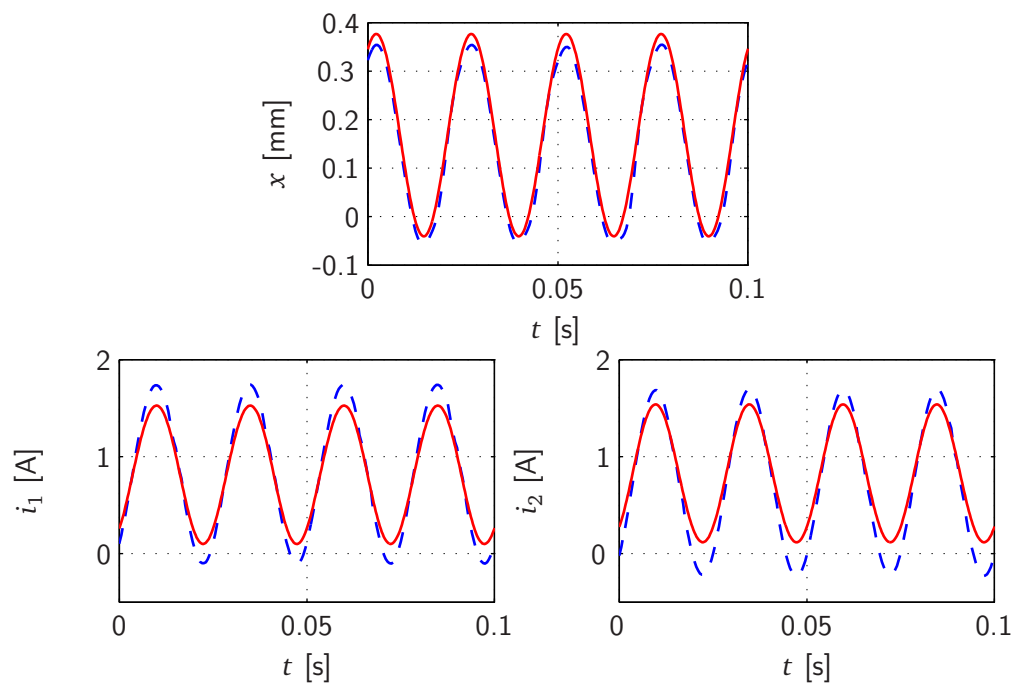

Figure 7.9.: Reluctance actuator HPS3: Position and current trajectories for a 40 Hz oscillation. Comparison of simulation [—] and experiment [– –].
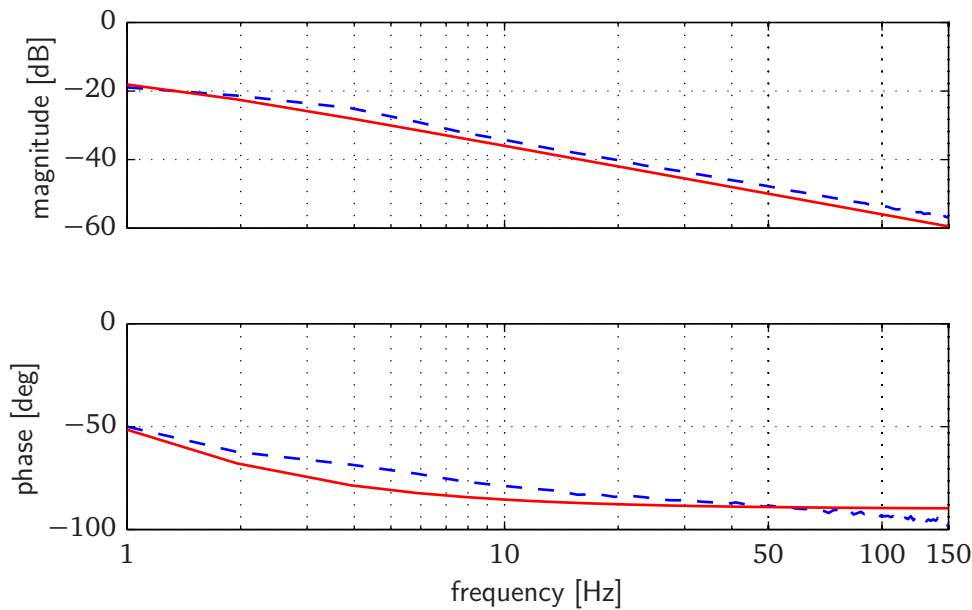
Figure 7.10.: Reluctance actuator HPS3: Simulated [—] and measured [– –] frequency response of the electric subsystem.

trajectories though the validation error increases with the frequency.

Overall, the co-energy based simulation predicts the dynamics of both actuators very well. Due to its solid core the HPS2 actuator is significantly influenced by eddy currents which can be modeled by a low pass filter. The remaining differences in the simulation of the HPS3 actuator can be further diminished by improving the model of the mechanical system since the membrane springs influence the overall actuator performance considerably.

For a further evaluation of the dynamic properties of the HPS3 actuator, the frequency response of the electric and magnetic subsystem is determined. For this purpose, both coils are simultaneously loaded with an equal sine sweep. No feedback control is used and the armature is not fixed during the experiment so that a free oscillation occurs due to the magnetic force generation. Figure 7.10 illustrates the transfer function of one coil in the electric subsystem which is calculated from the voltage command and the measured current. For the second coil a similar response is determined. The measured amplitude and phase characteristics exhibit a first order characteristic with a cutoff frequency of $0.8\,\mathrm{Hz}$. The validation of the experimental results with the theoretical values of the first-order coil model in (3.21) using the inductivity $L = 1\,\mathrm{H}$ and coil resistance $R = 5\,\Omega$ yields a good agreement.

In contrast, the transfer function from the coil current to the magnetic force is determined indirectly from the position and acceleration signal assuming a rigid body armature. The known armature mass and spring constants enable the calculation of the generated magnetic force. Figure 7.11 shows the measured frequency response. Both the amplitude and phase characteristics show no significant decrease in the investigated frequency range. The approximately constant responses indicate an efficient eddy current reduction by the laminated magnetic circuit. The measured magnitude $63\,\mathrm{dB}$ for low frequencies is close to the static force-current $k_{Fi} = 1\,\mathrm{kN/A}$
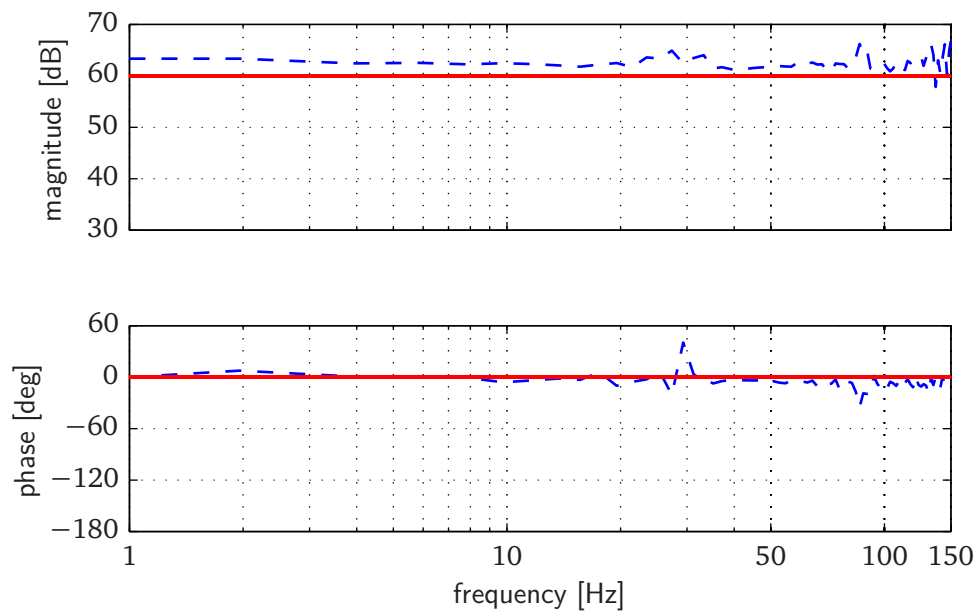
Figure 7.11.: Reluctance actuator HPS3: Simulated [——] and measured [– –] frequency response of the magnetic subsystem.

determined in Section 7.1.2. The remaining deviations are mainly due to the armature movement which causes airgap variations. These in turn influence the inductance and force generation.

The performance enhancement through the lamination of the flux-guiding core and armature parts becomes more obvious in comparison to the solid magnetic system of the HPS2 actuator whose cutoff frequency is 45 Hz [33]. Furthermore, by using the standard electrical steel M250-35A significant cost benefits in a potential industrial production can be realized.

However, the overall performance of reluctance actuators is determined by the dynamics of the electric subsystem. The large inductance allows for a high force-current factor, but limits the achievable bandwidth compared to electrodynamic shakers. In conclusion, magnetic reluctance shakers are suitable for applications requiring high forces at low frequencies.

8. Conclusions

Magnetic reluctance actuators have a great application potential in vibration testing. This thesis has presented a framework for the design and simulation of permanent magnet reluctance shakers. The realized actuators are intended for the disturbing noise analysis of vehicles and components in automotive NVH testing. A brief summary of the key findings is given in the following and complemented by suggestions for future research.

8.1. Summary

The point of origin for this thesis is set in Chapter 2 which gives an overview of vibration testing and the analysis of products for disturbing noise. A comparison of hydraulic, electrodynamic and reluctance drive concepts illustrates the application potential of magnetic reluctance actuators for NVH testing. The main advantages are a high force density, robustness, low power consumption and energy supply with electric current. An introduction to test rigs for the simulation of road drives in a laboratory environment shows the requirements on translatory reluctance drives for the controlled excitation of vibration. The direct body excitation (DBE) of vehicles via the frame instead of the wheels and suspension enables a sufficient excitation with the small achievable strokes of reluctance actuators.

Chapter 3 treats relevant key aspects of high performance actuators. Besides the generation of reluctance forces, the main loss mechanisms in the core and windings are discussed. For the development of high dynamic actuators particularly the reduction of eddy current influence in the magnetic system is essential. Moreover, different modeling approaches for the design and simulation are evaluated. For calculation of the main actuator parameters during the first design phase linear reluctance circuits are used due to their low computational cost. Finite element models allow for a detailed analysis of the magnetic circuit. For dynamic simulation, a reduced order approach based on numerical co-energy calculations is used. It enables an accurate prediction of the nonlinear actuator characteristic and a fast system simulation.

The magnetic design of the reluctance shaker HPS3 is presented in Chapter 4. First of all the design objectives are determined, based on given road profiles. The maximum magnetic force is 8 kN with a peak stroke of $\pm$ 3.5 mm, which allows for the excitation of heavy test objects with frequencies up to 100 Hz. With respect to the intended application, different topologies and selection criteria of magnetic materials are discussed. A fully laminated, polarized topology is proposed featuring two coils, two separate armature plates and surface mounted magnets. Mechanical springs fully compensate the negative magnetic stiffness and enable a stable operation. As material for the flux-guiding parts the standard electrical steel M250-35A is chosen. NdFeB permanent magnets with very high energy density provide the magnetic bias. The

development is based on a magnetic equivalent circuit model for the dimensioning and numerical field calculations for the detailed design analysis.

Chapter 5 describes the development of an energy-based simulation model for magnetic reluctance actuators. For this purpose an analytical approximation of discrete co-energy values, which are calculated during static FE simulations, is carried out. The resulting simulation model features low numerical cost and captures the nonlinear characteristics of reluctance actuators very well. Moreover, the model preserves all major advantages of the FE analysis such as the incorporation of saturation by using the nonlinear B-H curve and the detailed mapping of complex geometries and flux leakage. The method couples a system simulation with the numerical field calculation thereby simultaneously reducing the model order. Due to its block oriented hierarchical structure, the mechatronic modeling approach is suitable for direct software implementation.

The mechatronic development is complemented by the mechanical design and the information processing which are the subject of Chapter 6. The mechanical design considerations aim at the strength assessment of the laminations and the membrane springs by adopting numerical analyses. Special attention is paid to the laminated armature, where a supporting structure minimizes the mechanical load on the armature stack. While the permanent magnet bias is beneficial from a magnetic perspective, the resulting instability deteriorates the operating behavior of the actuator. Hence the compensation of the destabilizing magnetic force by the restoring force of membrane springs is a key feature of the proposed actuator concept. This approach enables a stick-slip free motion at high frequencies and a stable actuator operation without feedback control. In addition, the controlled tracking of reference profiles requires an intelligent actuator system. For this purpose, the developed shakers are extended to a vibration excitation system consisting of power electronics, real time hardware, sensor system and monitoring PC.

Chapter 7 presents selected results from simulations and experiments. For the accurate measurement of high magnetic forces a materials testing machine is adapted which allows for the precise positioning of the armature. Experiments with a fixed armature enable the measurement of the static actuator characteristics. The comparison to the design objectives defined in Chapter 4 shows, that the generated forces are sufficient for a realistic excitation of heavy passenger cars. Moreover, experiments with a moving armature serve for the validation of the dynamic simulation models and illustrate the frequency characteristics of the developed actuators. Both the transfer functions of the electric and magnetic subsystem are measured. The laminated magnetic system of the HPS3 actuator effectively reduces eddy currents and facilitates a sufficient excitation at higher frequencies up to 150 Hz. Furthermore, the use of standard electrical steel enables significant cost benefits in a potential industrial production.

8.2. Recommendations for Future Research

Several suggestions for future research can be made from the experiences gained during the work on this thesis. In the following, selected problems relating to the design, simulation and control of reluctance shakers as well as promising applications are discussed.

Actuators

For surface-mounted magnets as in the chosen topology, the required reluctance surface determines the length and width of the permanent magnets. A separation of the iron pole surface and magnet area could be achieved by using pole pieces. Moreover, the investigation of parallel polarized topologies is promising. In contrast to serial polarized magnetic systems, higher specific forces can be obtained since the reluctance due to the magnet in the coil flux path can be avoided.

The thermal load in the coil system is a key factor for a further reduction of the actuator size and weight. A detailed thermal design can lead to a significant reduction of the coil size. For the HPS3 actuator passive cooling has been chosen. However, for applications in which the noise of cooling fans is not relevant, an active cooling system could be considered which would enable the design of very compact reluctance shakers.

The mechanical design can be improved by the development of membrane springs with laser cut pockets. While isotropic springs are sufficient for a robust and stable actuator operation, a detailed adjustment of the spring characteristics allows for a further enhancement of the performance. Here the observation of the fatigue limit and the avoidance of acoustic emissions are important. Preliminary experimental results suggest that inserting fewer but larger pockets is beneficial. Additionally, the restoring force could be chosen such that the armature is positioned exactly in its central position.

Simulation and Control

Improved simulation results can be obtained for the HPS3 actuator by a better parameterization of the model for the mechanical subsystem. For this purpose, the characteristics of the spring system must be determined separately from those of the magnetic system. Experiments with the HPS2 actuator show that this can be achieved by measuring the force characteristics of a dummy actuator without magnetic core.

Although the force generation of reluctance actuators is nonlinear, the experimental determination of linear transfer functions in the frequency domain is beneficial for a performance assessment. For this purpose, the presented force test rig can be further used. Yet, a force sensor and sensor electronics suitable for high dynamic measurements must be chosen. For further experiments with a moving armature, a dynamometer could be set up. Currently, the generated coil currents during idling or actuation of comparatively small masses are too low for a validation of the entire performance spectrum. The developed component test rigs shown in Figure 2.5 can serve as a prototype, thereby supporting the static weight of an actuated large mass by air bellows.

For the trajectory tracking control of the reluctance shakers, approaches based on system identification and basic lumped parameter models have been used by HERRMANN and KOCH [33, 53]. A promising concept is the use of the presented co-energy based model for control design. For a first investigation, linear state space and nonlinear flatness-based feedback control designs are suggested. Using lookup tables instead of evaluating the analytical functions for the co-energy and its derivatives in each time step can reduce the computational effort considerably.

Applications

The functionality of the developed HPS3 actuator has been demonstrated in laboratory experiments. Consequently, tests in a road simulator with four actuators should be carried out. For this purpose the control concept developed in [53] can be used. However, the control structure can be considerably simplified because of the inherent stability of the actuators.

Currently, the maximum coil current is limited to 5 A by the power electronics. The achievable force can be further increased by designing enhanced power electronics which are capable of providing the rated coil current of 8 A. This would allow for the excitation of heavier vehicles.

Industrial vibration testing is mainly carried out in one dimension only or in three dimensions with a sequential excitation. A simultaneous excitation of all three dimensions reduces the analysis time and enhances the degree of reality. Since such a test rig must be driven by at least three actuators, the small size and low power consumption of magnetic reluctance actuators is beneficial.

A. Permanent Magnet Assembly Device

During the assembly of the prototype actuator the magnets are mounted in an already magnetized state. Thus magnetic forces between the core and permanent magnets as well as among the magnets themselves occur. In order to ensure the required precision and an efficient assembly, the jig shown in Figure A.1 has been developed for the magnet mounting on the core [11].

1	rear stop
2	base plate
3	lateral stop
4	limit stop
5	magnet
6	core
7	linear guiding
8	magnet holder
9	carriage
10	holder guiding
11	clamp
12	support rail
13	locking pin
14	hand gear
15	positioning rail
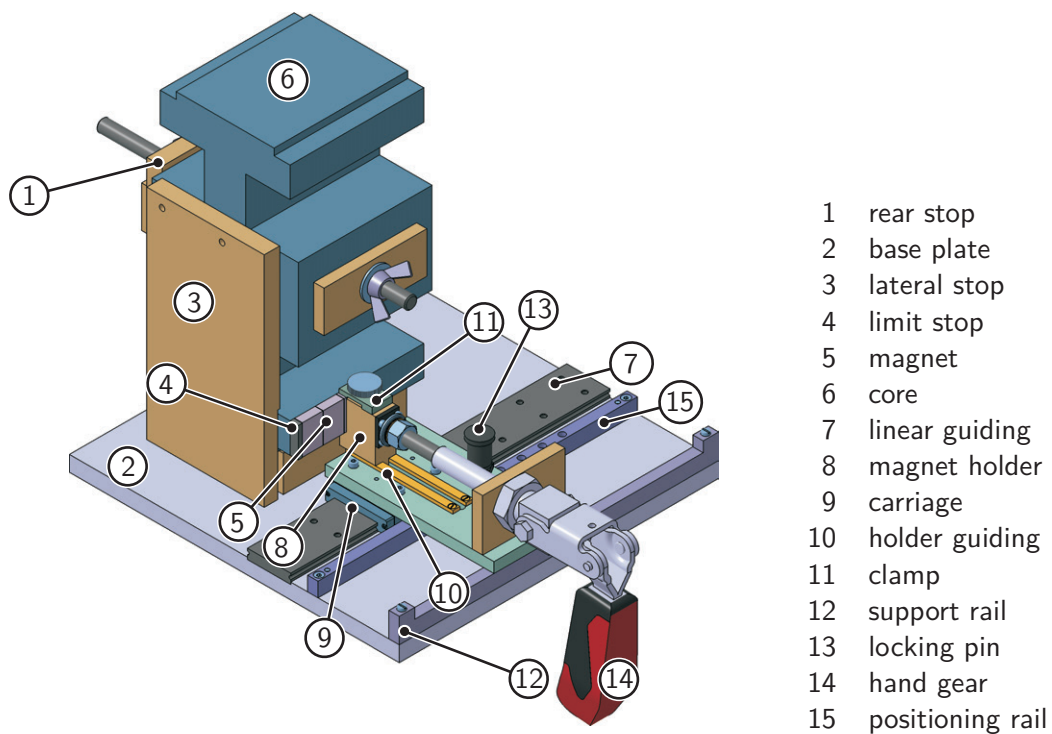
Figure A.1.: Permanent magnet mounting jig.

B. Technical Data

Table B.1.: Reluctance actuator HPS3: main parameters.

	symbol	unit	value
actuator			
stroke (pk-to-pk)	$\hat{x}$	mm	7
static force	$F_{s,max}$	N	8000
static force-current factor	k_{Fi}	N/A	1000
frequency range	f	Hz	0 … 100
rated current	I_r	A	8
mean coil resistance	R_c	Ω	2 × 5
mean coil inductance	L	H	2 × 1
no. of membrane springs	n_s		4
length		mm	292
width		mm	292
height		mm	295
weight		kg	65
laminations			
material			M250-35A
thickness	t	mm	0.35

Table B.2.: Reluctance actuator HPS3: coil parameters.

	symbol	unit	value
inner length		mm	134
inner width		mm	92
outer length		mm	238
outer width		mm	182
height		mm	47
winding area	A_w	mm^2	1886
rated current density	J_r	A/mm^2	5
temperature class	T_r	°C	180
copper diameter	d_{co}	mm	1.6
winding number	w		825
magnetomotive force	$\Theta_{c,max}$	A	6600

Table B.3.: Reluctance actuator HPS3: permanent magnet parameters.

	symbol	unit	value
material			Vacodym 655 HR
remanence	B_r	T	1.28
coercivity	H_{cB}	kA/m	990
energy density	BH_{max}	kJ/m^3	315
max. temperature		°C	150
number of cuboids			24
length		mm	20
width		mm	29
height	h_{PM}	mm	7.7
magnetomotive force	Θ_{PM}	A	7623

Table B.4.: Magnetic circuit design parameters.

	symbol	unit	value
maximum static force	$F_{s,max}$	kN	8
length inner airgaps	x_{ji}	mm	3.5
length outer airgaps	x_{jo}	mm	3.6
maximum flux density	B_{max}	T	1.4
leakage factor	σ		0.15
stacking factor	k_{st}		0.95
copper filling factor	k_{co}		0.7

Bibliography

[1] ANSYS INC.: *Low-Frequency Electromagnetic Analysis Guide*. Release 12.0, Apr. 2009

[2] ANTHONIS, J. ; VAES, D. ; ENGELEN, K. ; RAMON, H. ; SWEVERS, J.: Feedback Approach for Reproduction of Field Measurements on a Hydraulic Four Poster. In: *Biosystems Engineering* 96 (2007), no. 4, pp. 435–445

[3] BECKLEY, P.: *Electrical Steels for Rotating Machines*. The Institution of Engineering and Technology, 2002 (IEE Power and Energy Series 37). – ISBN 9780852969809

[4] BERRUT, J.-P. ; TREFETHEN, L.: Barycentric Lagrange Interpolation. In: *SIAM Rev* 46 (2004), pp. 501–517

[5] BÖDRICH, Th.: Electrodynamic and Electromagnetic Direct Drives for Reciprocating Compressors. In: *Proc. of the 11th Int. Conference on New Actuators (ACTUATOR)*. Bremen, Germany, June 2008, pp. 449–452

[6] BOLDEA, I. ; NASAR, S.: Linear electric actuators and generators. In: *IEEE Transactions on Energy Conversion* 14 (1999), no. 3, pp. 712–717

[7] BOLL, R.: *Weichmagnetische Werkstoffe: Einführung in den Magnetismus. VAC-Werkstoffe und ihre Anwendung*. Publicis Corporate Publishing, 1990. – ISBN 9783800915460

[8] BOLTE, E.: *Elektrische Maschinen: Grundlagen, Magnetfelder, Wicklungen, Asynchronmaschinen, Synchronmaschinen, Elektronisch kommutierte Gleichstrommaschinen*. Springer, 2012. – ISBN 9783642054846

[9] BRAUER, J.: *Magnetic Actuators and Sensors*. Wiley-IEEE Press, 2006. – ISBN 9780471731696

[10] BRINES, R. ; WEISS, L. ; PETERSON, E.: The Application of Direct Body Excitation Toward Developing a Full-Vehicle Objective Squeak and Rattle Metric. In: *Proc. of the SAE 2001 Noise & Vibration Conference & Exposition*, 2001

[11] BURGER, J.: *Entwurf und Realisierung einer Fertigungsvorrichtung für permanentmagnetisch erregte Reluktanzaktoren*, Technische Universität München, Semesterarbeit, 2011

[12] CANTIENI, R.: Experimental Methods used in System Identification of Civil Engineering Structures. In: *Proc. of the 1st Int. Operational Modal Analysis Conference (IOMAC)*. Copenhagen, Denmark, 2005, pp. 249–60

[13]   CASSING, W ; STANEK, W. ; ERD, L. ; HÜBNER, K.-D. ; KOCH, J. ; DUKART, A.: *Elektromagnetische Wandler und Sensoren: Grundlagen, feldnumerische Berechnung elektromagnetischer Felder und Anwendungen in der Mechatronik*. Expert Verlag, 2002. – ISBN 3816918786

[14]   CHEN, X. ; ZHU, Z. ; HOWE, D. ; DAI, J.: Comparative Study of Alternative Permanent Magnet Linear Oscillating Actuators. In: *Proc. of the International Conference on Electrical Machines and Systems, ICEMS 2008*. IEEE, 2008, pp. 2826–2831

[15]   CHILLET, Ch. ; VOYANT, J.-Y.: Design-Oriented Analytical Study of a Linear Electromagnetic Actuator by Means of a Reluctance Network. In: *IEEE Transactions on Magnetics* 37 (2001), July, no. 4, pp. 3004–3011. – DOI 10.1109/20.947053. – ISSN 0018–9464

[16]   CLAEYSSEN, F. ; MAGNAC, G. ; MARION, F. ; BARILLOT, F. ; MENEROUD, P. ; PATIENT, G.: Moving Coil or Moving Iron Controllable Actuators: How to make the good choice. In: *Proc. of the 6th Int. Symposium on Linear Drives for Industrial Applications (LDIA)*, 2007

[17]   CLARK, R. ; JEWELL, G. ; FORREST, S. ; RENS, J. ; MAERKY, C.: Design Features for Enhancing the Performance of Electromagnetic Valve Actuation Systems. In: *IEEE Transactions on Magnetics* 41 (2005), no. 3, pp. 1163–1168

[18]   DIETRICH, A.: *FEM-basierte Makromodellierung eines elektromagnetischen Aktors*, Technische Universität München, diploma thesis, 2008

[19]   DIN EN 60317: *Technische Lieferbedingungen an bestimmte Typen von Wickeldrähten - Teil 0-1: Allgemeine Anforderungen*. Feb. 2009

[20]   DSPACE GMBH: *DS1104 R&D Controller Board. Hardware Installation and Configuration*, 2006

[21]   DSPACE GMBH: *Embedded Success - Catalog 2012*. 2012

[22]   DUPONT: *VOLTATEX E1175 W*. Wilmington, USA, 2006

[23]   DYER, S. ; HE, X.: Least-Squares Fitting of Data by Polynomials. In: *IEEE Instrumentation & Measurement Magazine* 4 (2001), Dec., no. 4, pp. 46 –51. – DOI 10.1109/5289.975465. – ISSN 1094–6969

[24]   FAVOT, V. ; WIEDEMANN, D. ; HERRMANN, M. ; ULBRICH, H.: Nonlinear Modelling and Flatness-Based Control for an Electromagnetic Reluctance Force Actuator. In: *Proc. of the 3rd IEEE Conference on Industrial Electronics and Applications (ICIEA)*, 2008, pp. 114–119

[25]   FEELEY, J.: A Simple Dynamic Model for Eddy Currents in a Magnetic Actuator. In: *IEEE Transactions on Magnetics* 32 (1996), Mar., no. 2, pp. 453 –458. – DOI 10.1109/20.486532. – ISSN 0018–9464

[26] FITZGERALD, A. ; KINGSLEY, Ch. ; UMANS, S.: *Electric Machinery*. 6. McGraw-Hill, 2002. – ISBN 9780073660097

[27] GENUIT, K.: Vehicle Interior Noise - Combination of Sound, Vibration and Interactivity. In: *Sound and Vibration* 43 (2009), no. 12, pp. 8

[28] GENUIT, K. (ed.): *Sound-Engineering im Automobilbereich: Methoden zur Messung und Auswertung von Geräuschen und Schwingungen*. 1. Auflage. Springer, 2010. – ISBN 9783642014147

[29] GINZINGER, L.: *Control of a Rubbing Rotor using an Active Auxiliary Bearing*, Technische Universität München, dissertation, 2009

[30] GOLLEE, R.: *Modellierung und Simulation elektromagnetischer Aktoren*, Technische Universität Dresden, dissertation, 2004

[31] GRASSER, A.: *Modellbildung und lineare Trajektorienfolgeregelung für Reluktanzaktoren*, Technische Universität München, diploma thesis, 2011

[32] HARTWIG, Ch.: *Magnetdynamischer Linear-Aktor*, Universität Hannover, dissertation, 2003

[33] HERRMANN, M.: *Entwurf, Berechnung und Regelung magnetischer Reluktanzaktoren*. München, Technische Universität München, dissertation, 2008

[34] HERRMANN, M. ; ULBRICH, H.: State Controlled Electromagnetic Shaker for Trajectory Tracking. In: *Proc. of the 6th Int. Symposium on Linear Drives for Industrial Applications (LDIA)*. Lille, France, Sept. 2007

[35] HOFMANN, O.: *Kennfeldvermessung für elektromagnetische Aktoren*, Technische Universität München, bachelor thesis, 2011

[36] HOWE, D.: Electromagnetic Actuation Systems - Design and Applications. In: *Proc. of the IEE Colloquium on Limited Motion Electrical Actuation Systems*. London, Oct. 1998

[37] HOWE, D.: Magnetic Actuators. In: *Sensors and Actuators* 81 (2000), Apr., pp. 268–274

[38] ISERMANN, R.: *Mechatronic Systems: Fundamentals*. Springer, 2005. – ISBN 9781852339302

[39] JACKSON, J.: *Classical Electrodynamics*. Wiley, 1998. – ISBN 9780471309321

[40] JANOCHA, H. (ed.): *Actuators: Basics and Applications*. Springer, 2010. – ISBN 9783642082665

[41] JELTSEMA, D. ; SCHERPEN, J.: Multidomain Modeling of Nonlinear Networks and Systems. In: *IEEE Control Systems Magazine* 29 (2009), no. 4, pp. 28–59

[42] JENDRITZA, D.: *Technischer Einsatz neuer Aktoren*. Expert-Verlag GmbH, 2005. – ISBN 9783816920670

[43] JONEIT, D.: *Modellierung und Simulation elektromagnetischer Antriebe in der Feinwerktechnik*. Wissenschaftliche Schriftenreihe Elektrotechnik. Berlin : Köster, 2000 (Bd. 34). – ISBN 3895743712

[44] JÖST, R.: Additional Experimental Analysis Possibilities for Car Body Structures by using High Power Electrodynamic Shakers. In: *Proc. of the LMS Conference Europe*, 2006

[45] KALLENBACH, E. ; KUBE, H. ; ZÖPPIG, V. ; FEINDT, K. ; HERMANN, R. ; BEYER, F.: New Polarized Electromagnetic Actuators as Integrated Mechatronic Components – Design and Application. In: *Mechatronics* 9 (1999), no. 7, pp. 769–784

[46] KALLENBACH, M.: *Entwurf von magnetischen Mini- und Mikroaktoren mit stark nichtlinearem Magnetkreis*, Technische Universität Ilmenau, dissertation, 2005

[47] KALLENBACH, E. ET AL.: *Elektromagnete: Grundlagen, Berechnung, Entwurf und Anwendung*. Vieweg+Teubner Verlag, 2012. – ISBN 9783834809681

[48] KAVARANA, F. ; REDIERS, B.: Squeak and Rattle - State of the Art and Beyond. In: *Sound and Vibration* (2001). – Issue Apr.

[49] KHATEEB, N. ; GERLING, D.: Computer Aided Macromodeling for Control of Electromechanical Systems. In: *Proc. of the Conference of Electric and Electronical Engineering (EEC)*. Aleppo, Syria, 2007

[50] KHATEEB, N. ; GERLING, D.: The Off-line Co-Simulation of the Switched Reluctance Motor using the Macromodel Approach. In: *Proc. of the ANSYS Conference & 25th CADFEM Users' Meeting*, 2007

[51] KHATEEB, N. ; GERLING, D.: SVD-based Macromodeling of a PM Motor using the Energy Function Method. In: *Proc. of the 13th European Conference on Power Electronics and Applications (EPE)*, 2009

[52] KIM, J. ; CHANG, J.: A New Electromagnetic Linear Actuator for Quick Latching. In: *IEEE Transactions on Magnetics* 43 (2007), no. 4, pp. 1849–1852

[53] KOCH, U.: *Modellbasierte Regelung elektromagnetischer Aktoren für Störgeräuschprüfstände*, Technische Universität München, dissertation, 2011

[54] KOCH, U. ; ULBRICH, H.: Adaptive Forward Compensation Control using Prefilters with Phase Equalization for a Reluctance Force Actuator. In: *Proc. of the 9th Int. Conference on Motion and Vibration Control (MOVIC)*. Munich, Sept. 2008

[55] KOCH, U. ; WIEDEMANN, D. ; SUNDQVIST, N. ; ULBRICH, H.: State-Space Modelling and Decoupling Control of Electromagnetic Actuators for Car Vibration Excitation. In: *Proc. of the IEEE Int. Conference on Mechatronics (ICM)*. Malaga, Spain, Apr. 2009

[56] KOCH, U. ; WIEDEMANN, D. ; ULBRICH, H.: Decoupled Decentral Control of Electromagnetic Actuators for Car Vibration Excitation. In: *Proc. of the IEEE Int. Conference on Mechatronics (ICM)*. Malaga, Spain, Apr. 2009

[57] Koch, U. ; Wiedemann, D. ; Ulbrich, H.: Development, Optimization and Evaluation of a Road Simulator with Four Reluctance Force Actuators. In: *Proc. of the 10th Int. Conference and Exhibition on Actuators and New Drive Systems (ACTUATOR)*. Bremen, Germany, June 2010. – ISSN 9783933339126

[58] Koch, U. ; Wiedemann, D. ; Ulbrich, H.: Model-Based MIMO State-Space Control of a Car Vibration Test Rig With Four Electromagnetic Actuators for the Tracking of Road Measurements. In: *IEEE Transactions on Industrial Electronics* 58 (2011), Dec., no. 12, pp. 5319 –5323. – DOI 10.1109/TIE.2010.2044740. – ISSN 0278–0046

[59] Kollmann, F. ; Schösser, Th. ; Angert, R.: *Praktische Maschinenakustik*. Springer, 2005. – ISBN 9783540200949

[60] Kost, A.: *Numerische Methoden in der Berechnung elektromagnetischer Felder*. Springer, 1996. – ISBN 9783540550051

[61] Küpfmüller, K. ; Kohn, G.: *Theoretische Elektrotechnik und Elektronik*. Springer, 1995. – ISBN 9783540565000

[62] Lang, G.: Electrodynamic shaker fundamentals. In: *Sound and Vibration* 31 (1997), no. 4, pp. 14–23

[63] Lang, G.: An Introduction to Shaker Thermodynamics. In: *Sound and Vibration* 38 (2004), pp. 14–19

[64] Lang, G. ; Snyder, D.: Understanding the Physics of Electrodynamic Shaker Performance. In: *Sound and Vibration* 35 (2001), October, no. 10, pp. 24–33

[65] Langley, F. ; Mellor, P.: A Short-Stroke Permanent Magnet Aerospace Actuator with High Force-to-Mass Ratio. In: *Proc. of the 32nd IEEE Annual Conference on Industrial Electronics (IECON)*, 2006, pp. 3199–3204

[66] LCD LaserCut AG: *Innovation als Antrieb.* `www.lcd-lasercut.ch`. Version: Dec. 2012

[67] Lequesne, B.: Fast-Acting, Long-Stroke Solenoids with Two Springs. In: *IEEE Transactions on Industry Applications* 26 (1990), Sept.–Oct., no. 5, pp. 848–856. – DOI 10.1109/28.60050

[68] Lequesne, B.: Permanent Magnet Linear Motors for Short Strokes. In: *IEEE Transactions on Industry Applications* 32 (1996), Jan.–Feb., no. 1, pp. 161–168. – DOI 10.1109/28.485828

[69] Maierthaler, M.: *Auslegung und Konstruktion einer Federführung*, Technische Universität München, student thesis, 2008

[70] Melcher, J.: *Continuum Electromechanics*. The MIT Press, 1981. – ISBN 9780262131650. – Also available online from MIT OpenCourseWare at `http://ocw.mit.edu/`, accessed Mar. 2012

[71] MENQ, F.-Y. ; STOKOE, K. ; PARK, K. ; ROSENBLAD, B. ; COX, B.: Performance of Mobile Hydraulic Shakers at nees@UTexas for Earthquake Studies / Department of Civil, Architectural and Environmental Engineering, University of Texas at Austin. 2009. – Technical report

[72] MICHALOWSKI, L. ; SCHNEIDER, J. ; SIEBERT, S.: *Magnettechnik: Grundlagen, Werkstoffe, Anwendungen*. Vulkan-Verlag, 2006. – ISBN 9783802721397

[73] MÜLLER, G. ; GROTH, C.: *FEM für Praktiker – Band 1: Grundlagen*. Expert-Verlag, 2002. – ISBN 9783816918578

[74] MOOSMAYR, T.: *Objektivierung von transienten Störgeräuschen im Fahrzeuginnenraum*, Technische Universität München, dissertation, 2009

[75] MOOSMAYR, T. ; EICHENSEER, F.: Komfortables Fahren - Prävention von Störgeräuschen. In: *ATZextra - Der neue BMW 7er* 8 (2008), pp. 88–90

[76] MTS SYSTEMS CORPORATION: *Model 320 Tire-Coupled Road Simulators*. Online. http://www.mts.com/. Version: 2011. – Application Note

[77] NELSON, C.: *Vibration Test Evolution: Single-Axis, Single-Shaker to 6DoF*. Online. http://www.teamcorporation.com/. Version: 2002. – Application Note

[78] OBERBECK, C.: *Entwicklung und mechatronische Optimierung eines elektromagnetischen Aktors*, Technische Universität München, dissertation, 2002

[79] ORTEGA, R. ; PEREZ, J. ; NICKLASSON, P. ; SIRA-RAMIREZ, H.: *Passivity-based Control of Euler-Lagrange Systems: Mechanical, Electrical and Electromechanical Applications*. Springer, 2010. – ISBN 9781849968522

[80] OTTO, J. ; KILLAT, U. ; VAN DUIJSEN, P.: Energy Based Model Synthesis for Electrical Actuators and Sensors. In: *Proceedings of PCIM 2002*. Nuremberg, Germany, May 2002

[81] PARK, K. ; BAE, M. ; YOO, D. ; SHANKAR, S.: A Study on Buzz, Squeak and Rattle in a Cockpit Assembly. In: *Proc. of the SAE 2005 Noise and Vibration Conference and Exhibition*, 2005

[82] PEETERS, B. ; VAN DER LINDEN, P. ; DE VEUSTER, C.: Performance of Miniature Shakers for Vehicle Component Testing. In: *Proc. of the 22nd IMAC Conference and Exposition: A Conference and Exposition on Structural Dynamics*, 2004

[83] PENNANDER, L.-O. ; NORD, G. ; MAEZAWA, K. ; SAITO, M. ; BERCHOWITZ, D.: Design of Soft Magnetic Composite Components for Tubular Linear Motors. In: *Proc. of the Motor and Drive Systems Conference*. Miami, USA, 2006

[84] PHILIPPOW, E. ; STEINMANN, W. ; WIELAND, F. ; BONFIG, K. ; BECKER, W.-J.: *Grundlagen der Elektrotechnik*. Verlag Technik, 2000. – ISBN 9783341012413

[85] PIERSOL, A. ; PAEZ, Th.: *Harris' Shock and Vibration Handbook (McGraw-Hill Handbooks)*. McGraw-Hill Professional, 2009. – ISBN 9780071508193

[86] Pyrhonen, J. ; Jokinen, T. ; Hrabovcova, V.: *Design of Rotating Electrical Machines*. Wiley, 2009. – ISBN 9780470695166

[87] Radler, O.: *Ein Beitrag zur Messung statischer und dynamischer Eigenschaften von elektro-magneto-mechanischen Energiewandlern und deren Komponenten*, Technische Universität Ilmenau, dissertation, 2011

[88] Rens, J. ; Clark, R. ; Jewell, G.: Static Performance of a Polarized Permanent-Magnet Reluctance Actuator for Internal Combustion Engine Valve Actuation. In: *IEEE Transactions on Magnetics* 42 (2006), Aug., no. 8, pp. 2063 – 2070. – DOI 10.1109/TMAG.2006.877269. – ISSN 0018–9464

[89] Riethmüller, J.: *Eigenschaften polarisierter Elektromagnete und deren Dimensionierung anhand eines Entwurfsalgorithmus mit einem Optimierungsverfahren*. ISLE, 2004. – ISBN 393263389X

[90] Robert Bosch GmbH: *Electromagnet*. 1991. – Patent: WO 91/06109

[91] Rodriguez, M. ; Sanz, C.: Simple Frequency Domain Model for Hysteresis and Eddy Currents in Cylindrical and Parallelepipedal Cores. In: *IEEE Transactions on Magnetics* 43 (2007), May, no. 5, pp. 1912–1919. – DOI 10.1109/TMAG.2007.892657. – ISSN 0018–9464

[92] Roschke, Th.: *Entwurf geregelter elektromagnetischer Antriebe für Luftschütze*, Technische Universität Dresden, dissertation, 2000

[93] Rosenbaum, S.: *Entwurf elektromagnetischer Aktoren unter Berücksichtigung von Hysterese*, Technische Universität Ilmenau, dissertation, 2011

[94] Rosenbaum, S. ; Baumbach, J. ; Belyaev, N. ; Beyer, F. ; Otto, R. ; Kallenbach, E. ; Kallenbach, M. ; Elsasser, A. ; Dingelstadt, R.: Verbesserung der dynamischen Parameter von Magnetventilen durch Optimierung des Energiemanagements des heterogenen Gesamtsystems. In: *VDI Berichte* 1971 (2007), pp. 85

[95] Sarasa, M. ; Gerling, D. ; Kastinger, G. ; Schuhmacher, A.: Soft Magnetic Materials for Electrical Machines. In: *Proc. of the Low Voltage Electrical Machines Conference (LVEM)*. Brünn, Czech Republic, Nov. 2003, pp. 91–98

[96] Schlamp, V.: *Vergleich und Bewertung von Antriebskonzepten zur Schwingungsanregung*, Technische Universität München, student thesis, 2012

[97] Schmülling, B. ; Lessmann, M. ; van der Giet, M. ; Hameyer, K.: Proposals for the Use of Magnetic Guideways for Vertical Transportation Systems. In: *International Journal of Electrical Engineering in Transportation (IJEET)* 4 (2008), no. 1, pp. 9–13

[98] Schätzing, W. ; Müller, G.: *FEM für Praktiker – Band 4: Elektrotechnik*. Expert-Verlag, 2003. – ISBN 9783816921578

[99] SCHULTZ, A.: *Simulationsgestützter Entwurf elektromagnetischer Linearaktoren für fluidtechnische Ventile*, RWTH Aachen, dissertation, 2006

[100] SIMONYI, K ; THEIL, H.: *Theoretische Elektrotechnik*. Wiley-VCH, 1993. – ISBN 9783527402663

[101] SMALLWOOD, D. ; HUNTER, N.: Transportable 56-kN, 200-mm Displacement Hydraulic Shaker for Seismic Simulation. In: *Proc. of the 21st Annual Meeting of the Institute of Environmental Sciences*. Anaheim, USA, 1975

[102] SMITH, S.: Lebesgue Constants in Polynomial Interpolation. In: *Annales Mathematicae et Informaticae* 33 (2006), pp. 109–123

[103] STÖHR, G.: *Untersuchungen zum Aufbau einer hocheffizienten Kühlung einer elektrischen Maschine mit großer Leistungsdichte*, Technische Universität Berlin, dissertation, 2007

[104] STÖLTING, H.-D. ; KALLENBACH, E. ; AMRHEIN, W. (EDS.): *Handbuch Elektrische Kleinantriebe*. Hanser Fachbuchverlag, 2011. – ISBN 9783446423923

[105] STRAHAN, R.: Energy Conversion by Nonlinear Permanent Magnet Machines. In: *Electric Power Applications (IEE)* 145 (1998), May, no. 3, pp. 193 –198. – DOI 10.1049/ip–epa:19981863. – ISSN 1350–2352

[106] STRÖHLA, T.: *Ein Beitrag zur Simulation und zum Entwurf von elektromagnetischen Systemen mit Hilfe der Netzwerkmethode*, Technische Universität Ilmenau, dissertation, 2002

[107] STROMMER, S.: *Nichtlineare Regelung eines elektromagnetischen Aktors*, Technische Universität München, diploma thesis, 2012

[108] THYSSENKRUPP STEEL AG: *Power Core - M250-35A Elektroband NO/NGO electrical Steel*. Duisburg, 2009

[109] TÄNZER, W.: *Membranfedern als Bauelemente für Federführungen*, Technische Hochschule Ilmenau, dissertation, 1983

[110] ULBRICH, H.: Comparison of Different Actuator Concepts for Applications in Rotating Machinery. In: *International Journal of Rotating Machinery* 1 (1994), pp. 61–71

[111] VACCUMSCHMELZE GMBH & CO. KG: *Elektromagnetisches Einspritzventil und Verfahren zu seiner Herstellung sowie Verwendung eines Magnetkerns für ein elektromagnetisches Einspritzventil*. 2008. – Patent: DE 10 2006 055 088 B4

[112] VACUUMSCHMELZE GMBH & CO. KG: *Soft Magnetic Materials and Semi-finished Products*. Hanau, 2002

[113] VACUUMSCHMELZE GMBH & CO. KG: *Rare-Earth Permanent Magnets VACODYM, VACOMAX*. Hanau, 2007

[114] Vidyasankar, S.: *What is NVH?* Online. `http://www.frost.com/`. Version: Apr. 2005

[115] Wang, J. ; Howe, D. ; Lin, Z.: Comparative Studies on Linear Motor Topologies for Reciprocating Vapor Compressors. In: *Proc. of the IEEE Electric Machines and Drives Conference (IEMDC)* vol. 1, 2007, pp. 364–369

[116] Wang, Y.: *Berechnung und Auslegung von Magnetstellgliedern mit Strom-Vormagnetisierung und mit Permanentmagnet-Vormagnetisierung*. Aachen : Shaker Verlag, 1996 (Berichte aus dem Maschinenbau). – ISBN 382651629X

[117] Wiedemann, D. ; Koch, U. ; Ulbrich, H.: A Co-Energy based Macromodel for an Electromagnetic Actuator. In: *Proc. of the IEEE Electric Machines and Drives Conference (IEMDC)*. Miami, USA, May 2009, pp. 1770–1775

[118] Wiedemann, D. ; Koch, U. ; Ulbrich, H.: Development of Magnetic Reluctance Actuators for Vibration Excitation. In: *Proc. of the 12th International Symposium on Magnetic Bearings (ISMB)*. Wuhan, China, Aug. 2010

[119] Wiedemann, D. ; Koch, U. ; Ulbrich, H.: Linear Reluctance Actuator for Controlled Vibration Excitation. In: *Proc. of the 10th International Conference and Exhibition on Actuators and New Drive Systems (ACTUATOR)*. Bremen, Germany, June 2010. – ISBN 9783933339126

[120] Wiedemann, D. ; Koch, U. ; Ulbrich, H.: Schwingungsanregung mit elektromagnetischen Anregungssystemen. In: *Antriebssysteme 2011 – Elektrik, Mechanik, Hydraulik in der Anwendung* vol. 2138. Düsseldorf, Germany : VDI-Verlag, Sept. 2011. – ISBN 9783180921389, pp. 315–324

[121] Wiedemann, D. ; Ulbrich, H.: Design Aspects and Static Performance of Permanent-Magnet Reluctance Actuators for Shaker Applications. In: *Proc. of the ASME Dynamic Systems and Control Conference/11th Motion & Vibration Conference (MOVIC)*. Fort Lauderdale, USA, Oct. 2012

[122] Will, D. ; Gebhardt, N. ; Herschel, D. ; Nollau, R. (eds.): *Hydraulik: Grundlagen, Komponenten, Schaltungen*. Springer, 2006. – ISBN 9783540343226

[123] Zeller, P.: *Handbuch Fahrzeugakustik: Grundlagen, Auslegung, Berechnung, Versuch*. Vieweg + Teubner, 2009. – ISBN 9783834806512

[124] Zhu, L. ; Knospe, C. ; Maslen, E.: Analytic Model for a Nonlaminated Cylindrical Magnetic Actuator including Eddy Currents. In: *IEEE Transactions on Magnetics* 41 (2005), Apr., no. 4, pp. 1248 – 1258. – DOI 10.1109/TMAG.2005.844847. – ISSN 0018–9464

[125] Zhu, Z. ; Jewell, G. ; Howe, D.: Design Considerations for Permanent Magnet Polarised Electromagnetically Actuated Brakes. In: *IEEE Transactions on Magnetics* 31 (1995), Nov., no. 6, pp. 3743 –3745. – DOI 10.1109/20.489757. – ISSN 0018–9464

[126] Zmood, R. ; Anand, D. ; Kirk, J.: The Influence of Eddy Currents on Magnetic Actuator Performance. In: *Proceedings of the IEEE* 75 (1987), Feb., no. 2, pp. 259 – 260. – DOI 10.1109/PROC.1987.13726. – ISSN 0018–9219